2010

A study of synchronization of nonlinear oscillators: Application to epileptic seizures

Daisuke Takeshita

Department: Physics

A STUDY OF SYNCHRONIZATION OF NONLINEAR OSCILLATORS: APPLICATION TO EPILEPTIC SEIZURES

by

DAISUKE TAKESHITA

A DISSERTATION

Presented to the Faculty of the Graduate School of the

MISSOURI UNIVERSITY OF SCIENCE & TECHNOLOGY

and

UNIVERSITY OF MISSOURI–ST. LOUIS

In Partial Fulfillment of the Requirements for the Degree

DOCTOR OF PHILOSOPHY

in

PHYSICS

2010

Approved by

Sonya Bahar, Advisor
Philip Fraundorf
Paul Parris
Thomas Vojta
Renato Feres

ABSTRACT

This dissertation focuses on several problems in neuroscience from the perspective of nonlinear dynamics and stochastic processes.

The first part concerns a method to visualize the idea of the power spectrum of spike trains, which has an educational value to introductory students in biophysics.

The next part consists of experimental and computational work on drug-induced epileptic seizures in the rat neocortex. In the experimental part, spatiotemporal patterns of electrical activities in the rat neocortex are measured using voltage-sensitive dye imaging. Epileptic regions show well-synchronized, in-phase activity during epileptic seizures. In the computational part, a network of a Hodgkin-Huxley type neocortical neural model is constructed. Phase reduction, which is a dimension reduction technique for a stable limit cycle, is applied to the system. The results propose a possible mechanism for the initiation of the drug-induced seizure as a result of a bifurcation.

In the last part, a theoretical framework is developed to obtain the statistics for the period of oscillations of a stable limit cycle under stochastic perturbation. A stochastic version of phase reduction and first passage time analysis are utilized for this purpose. The method presented here shows a good agreement with numerical results for the weak noise regime.

ACKNOWLEDGMENTS

I would like to thank Dr. Sonya Bahar for all her support and encouragement toward the completion of the degree. Having such a *wonderful* person as an advisor makes my hard life easier. I would like to thank Dr. Renato Feres from whom I have learned a lot of interesting mathematics. The work of Section 5 has been done in collaboration with him. I would like to acknowledge other committee members, Dr. Paul Parris, Dr. Thomas Vojta, and Dr. Philip Fraundorf for their services and comments.

I would like to thank Dr. Vassiliy Tsytsarev from who I have leaned how to do experiments on in vivo rat neocortex. Special thanks go to Dr. Yasuomi Sato who has helped me with phase reduction. I would like to thank Dr. Frank Moss, who was my advisor for the first three years in the graduate program, for accepting me as a graduate student, his generosity, and being *the* attractor of our research group. I am glad that I savor his unique imagination in research. I would like to thank Dr. Alexander Neiman, who I respect as master of nonlinear dynamics and stochastic processes, for educating me and motivating me to learn more on the subjects. My maturity in physics and English communication skills have improved a lot through the interaction with Dr. Jorge Brea, with whom I spent several years in the same lab as graduate students. I would like to thank Dr. Lon Wilkens and Dr. Michael Hofmann for educating me on neuroscience. I would like to thank Mrs. Elaine Moss for her care and encouragement by her artwork. I appreciate Dr. Ta-Pei Cheng for his help throughout the graduate program. It was a great experience that I was able to contribute, even with a small amount, to his book on relativity and cosmology.

I would like to acknowledge the following funding sources: Epilepsy Foundation Predoctoral Fellowship, Dissertation Fellowship from UM-St. Louis, and Dr. Bahar's NSF Career Grant No.PHY-0547647 and her Startup Funds.

Finally, I would like thank my wife, Kazumi, for her dedication, support, and patience. Without her support, the quantity and quality of this dissertation would have been much less than what they are.

TABLE OF CONTENTS

Page

ABSTRACT iii

ACKNOWLEDGMENTS iv

LIST OF ILLUSTRATIONS x

LIST OF TABLES xii

SECTION

1. INTRODUCTION 1

1.1. OUTLINE 1

1.2. THE NERVOUS SYSTEM -- OVERVIEW 2

1.2.1. Brief Anatomy of a Neuron 3

1.2.2. Cell Membrane 3

1.2.3. Ion Channels 3

1.2.4. Resting Potential 4

1.2.5. Action Potential 5

1.2.6. Ion Pumps 7

1.2.7. Neural Communication -- Synapse 8

1.2.8. Electrical Flows in a Neuron 10

1.2.9. Neocortex 11

1.2.9.1 Laminar structure of neocortex 11

1.2.9.2 Morphological classification of neocortical neurons 11

1.2.9.3 Electrophysiological classification of neocortical neurons 13

1.2.9.4 Some statistics of neocortical neurons 13

1.2.10. Synchronization in the Brain 14

1.2.11. Epileptic Seizures 14

1.2.11.1 Definition of epilepsy 14

1.2.11.2 Clinical aspects of epileptic seizures 15

1.2.11.3 Experimental animal models of epileptic seizures 15

1.2.11.4 4-aminopyridine epileptic seizures 16

1.3. MEASUREMENT OF NEURAL SIGNAL 16

1.3.1. Local Field Potential 16
1.3.2. Voltage-Sensitive Dye Imaging 20
1.4. BIOPHYSICS OF SINGLE NEURON DYNAMICS 20
1.4.1. Nernst Potential 21
1.4.2. Dynamics of Voltage-Dependent Ion Channel 23
1.4.3. Ionic Current 26
1.4.4. The Membrane Model 27
1.4.5. "Canonical" Form of Conductance-Based Model 28
1.4.6. Example: Morris-Lecar Equations 28
1.5. NONLINEAR DYNAMICS 33
1.5.1. Linear Stability Analysis 33
1.5.1.1 One-dimension case 33
1.5.1.2 Two-dimensional case 34
1.5.2. Stable Limit Cycle 36
1.5.3. Bifurcation 36
1.5.3.1 Saddle-node bifurcation 36
1.5.3.2 Hopf bifurcation 37
1.5.3.3 Bifurcations in neural dynamics 39
1.5.4. Phase Reduction 40
1.5.4.1 Phase function and isochrons 40
1.5.4.2 First order phase reduction 42
1.5.4.3 Two oscillator problem 43
1.5.5. Phase Synchronization Analysis 44
1.5.6. Singular Perturbation 45
1.6. SOME CONCEPTS FROM PROBABILITY THEORY AND STOCHASTIC PROCESSES 48
1.6.1. Probability 48
1.6.2. Conditional Probability 48
1.6.3. Independence 49
1.6.4. Random Variables, Distribution, and Density 49
1.6.5. Expected Value, Variance, Moments 50
1.6.6. Mean Square Limit 51

1.6.7. Moment Generating Function 51
1.6.8. Stochastic Processes 51
1.6.9. Markov Process 52
1.7. STOCHASTIC DIFFERENTIAL EQUATIONS 52
1.7.1. Wiener Process 53
1.7.2. White Noise 53
1.7.3. Stochastic Integrals: Ito and Stratonovich 54
1.7.4. Change of Variables: Ito Formula 58
1.7.5. Ito or Stratonovich 59
1.7.6. Forward and Backward Fokker-Planck Equations 59
1.7.7. First Passage Time Problem 62
2. ANALYZING SPIKE TRAINS WITH CIRCULAR STATISTICS 65
2.1. OBJECTIVES 65
2.2. FORMULATION 66
2.2.1. Power Spectrum of a Sequence of Spikes 67
2.2.2. Circular Statistics 69
2.3. APPLICATIONS 71
2.3.1. Discrete Fourier Transform (DFT) 71
2.3.2. Circular Statistics (CS) 71
2.4. RESULTS 72
2.5. DISCUSSION 74
2.6. CONCLUSION 77
2.7. SUGGESTED PROBLEM: POISSON SPIKE TRAINS 77
3. SYNCHRONIZATION ANALYSIS OF VOLTAGE-SENSITIVE DYE IMAGING DURING DRUG-INDUCED SEIZUERES IN THE RAT NEOCORTEX 79
3.1. OBJECTIVES 79
3.2. EXPERIMENTAL METHODS 79
3.2.1. Surgery and Staining 80
3.2.2. Electrophysiology 80
3.2.3. Drug Administration 80
3.2.4. Recording 81

3.3. DATA ANALYSIS 82
3.3.1. Noise/Artifact Reduction 83
3.3.1.1 Baseline drift 83
3.3.1.2 Random noise 84
3.3.1.3 Heartbeat artifact 84
3.3.1.4 Respiration artifact 84
3.3.2. Determination of Seizure Area 85
3.3.3. Synchronization Analysis 85
3.4. RESULTS 85
3.4.1. Description of Seizure Events 86
3.4.2. Patterns of Local Field Potential during Seizure Events 86
3.4.3. Change of Seizure Area over Time 86
3.4.4. Phase Synchronization 88
3.4.5. Phase Maps 92
3.5. DISCUSSION 94
3.5.1. Comparison with Previous Studies 94
3.5.2. Future Work 95
3.5.3. Limitation of the Present Study 95
3.6. CONCLUSION 96
4. MODELING SEIZURE DYNAMICS 97
4.1. OBJECTIVES 97
4.2. NEOCORTICAL NEURAL MODEL 97
4.3. RESULTS 99
4.3.1. Phase Reduction 99
4.3.2. Effect of Noise -- Two Neuron Case 101
4.3.3. Network without Noise 101
4.3.4. Network with Noise 102
4.4. DISCUSSION 105
4.4.1. Comparison with Previous Studies 105
4.4.2. Limitations and Shortcomings of the Present Model 105
4.5. CONCLUSION 107

5. STOCHASTIC ANALYSIS OF LIMIT CYCLE OSCILLATOR 108
5.1. OBJECTIVES 108
5.2. MOTIVATION: STOCHASTIC NEURAL MODEL 109
5.3. STOCHASTIC PHASE REDUCTION 110
5.4. HIGER ORDER APPROXIMATION OF ISOCHRONS 112
5.4.1. Some Definitions and Notations 112
5.4.2. The Main Results 114
5.4.3. The Stuart-Landau Oscillator: an Illustration 115
5.5. DETERMINATION OF MOMENTS OF PERIOD 119
5.5.1. First Passage Time Analysis 119
5.5.2. Numerical Results 123
5.5.3. Application to a Limit Cycle Oscillator 125
5.6. CONCLUSION 127
BIBLIOGRAPHY 129
VITA 140

LIST OF ILLUSTRATIONS

Figure Page

1.1. Neurons of different kinds 4

1.2. An action potential 6

1.3. Schematic diagram of a chemical synapse 9

1.4. An example of the excitatory synaptic potential 10

1.5. The laminar structure and locations of pyramidal neurons in the neocortex 12

1.6. Membrane current caused by excitatory synaptic current 18

1.7. Different geometries of neurons and their corresponding electrostatic models 19

1.8. A container with a permeable membrane only to K^+ 22

1.9. An equivalent electrical circuit to the membrane model 27

1.10. Response to a brief current injection in the ML model 30

1.11. Variables of ML model in the phase plane 31

1.12. The time course of membrane potential responding to constant current with different values 32

1.13. The time course of ionic currents 32

1.14. The time derivative of x as a function of x for the system in Eq. 25 35

1.15. An example of a stable limit cycle 37

1.16. An example of saddle-node bifurcation 38

1.17. Isochrons for the Stuart-Landau oscillator for different parameter sets 41

1.18. A comparison between the analytical and outer approximate solution for Eq. 49 47

1.19. A realization of simulated Wiener process 54

1.20. The analytical (solid line) and approximate (dashed line) solution for the mean first passage time 64

2.1. Circular statistics for detecting preferred direction. 67

2.2. Schema of circular statistics 70

2.3. Comparison between CS and PS 73

2.4. Diagrams of circular statistics 75

2.5. Circular statistics applied to spike trains with noise in the frequency 76

3.1. Cranial window on the skull of the rat 81

3.2. A schema of the recording setup 82

3.3. Comparison among the raw and processed voltage-sensitive dye signals, and local field potential during a seizure event 83
3.4. Example local field potential patterns during a seizure event 87
3.5. Time course of seizure area 88
3.6. LFP and γ (synchronization index) before and during seizure event 89
3.7. Changes in overall synchronization index and spatial map of synchrony 90
3.8. The same plot as Figure 3.7, but showing a seizure event in another rat 91
3.9. Maximum averaged synchronization indices before and during seizure events 92
3.10. Phase map of voltage-sensitive dye imaging during a seizure 93
4.1. Results of phase reduction applied to the neocortical model 100
4.2. Bifurcation diagram 100
4.3. Mean field for a pair of coupled neurons 102
4.4. Mean field and raster plot of netwwork without noise 102
4.5. Mean field, clustering index, and raster plot of network with noise 104
4.6. Comparison between simulation and experiment 106
5.1. Diagram of the approach taken 108
5.2: Determination of $Q_t^{(2)}$ for the Stuart-Landau oscillator 120
5.3. $<T_{fp}>$ is plotted as a function of starting point (x_0) 124
5.4. VAR(T_{fp}) is plotted as a function of starting point (x_0) 125
5.5. A comparison between the numerical and analytical results of the mean (left) and variance (right) of the period of the Stuart-Landau oscillator 127

LIST OF TABLES

Table Page

1.1. Ion concentrations at resting state.....5

1. INTRODUCTION

"Science is built up of facts, as a house is with stones. But a collection of facts is no more a science than a heap of stones is a house."-Henri Poincaré

"If we knew what it was we were doing, it would not be called research, would it?"
-Albert Einstein

1.1. OUTLINE

Quantitative approaches in neuroscience have recently been attracting great attention. This dissertation focuses on several different problems in neuroscience using approaches from nonlinear dynamics and stochastic processes.

This Section summarizes the background for the rest of the dissertation. In 1.2, a quick overview of the nervous system is given. Section 1.3 describes methods used in Section 3 and 4 to measure electrical activity in the neural system. Section 1.4 explains how spiking activity of a single neuron occurs in a quantitative language. In 1.5, basic facts from nonlinear dynamics are summarized. Some basic definitions from probability theory and stochastic processes are summarized in Section 1.6. Section 1.7 provides a quick overview of stochastic differential equations. A significant amount of effort was made to make this dissertation as self-contained as possible, due to the fact that the field of this dissertation does not belong to traditional physics and is highly interdisciplinary. Cross-references are made throughout the dissertation. Hopefully, the reader can start reading from anywhere in Sections 2-5 and refer to topics in this Section when necessary.

Section 2 presents a method, circular statistics, to analyze a certain class of neural signals (spike trains). Although it is shown that the method is equivalent to the power spectrum, the method can be utilized to introduce the notion of the power spectrum at an introductory level. The results presented here have been published [1].

Section 3 focuses on the synchronization analysis of voltage-sensitive dye imaging during drug-induced seizures in the rat neocortex. Phase synchronization analysis is applied to the signals from the voltage-sensitive dye imaging to characterize

spatiotemporal patterns of synchronization during seizure events. Some preliminary results from this Section have been presented in a conference with a published abstract [2].

Section 4 concerns the modeling of epileptic dynamics in the drug-induced seizures studied in the previous section. The dynamics of a neocortical neuron is modeled by a conductance-based model (Hodgkin-Huxley type model). A dimension reduction technique, phase reduction, is applied to a pair of neurons to obtain stable and unstable phase differences between the two neurons as a function of a control parameter which mimics the effect of a seizure-inducing drug. The results presented here have been published [3].

Section 5 focuses on the development of a theoretical framework for stochastic perturbation of limit cycles. A theoretical framework for obtaining the statistics of the period of a limit cycle oscillator is developed using a stochastic version of phase reduction. A part of the results presented here has been submitted [4].

1.2. THE NERVOUS SYSTEM -- OVERVIEW

In this section, some basic facts about the nervous system are provided. To make this subsection simple and readable, the description is sometimes idealized at the expense of precision. For more precise and exhaustive knowledge, the reader is referred to [5-7].

The nervous system of animals is classified into two groups[1]: the peripheral and central nervous systems. The central nervous system consists of systems such as the brain and spinal cord, while the nerves connecting to the central nervous system belong to the peripheral nervous system. The review below is restricted to molecular, single-cell, and network levels in the brain, especially the neocortex, since those are most relevant to the dissertation.

The brain mainly consists of two types of cells: neurons and glial cells. Although it had been thought that only neurons are critical elements for electrical communication in the brain, recent evidence suggests that glial cells may be as important as neurons. However, the role of glia is beyond the scope of this dissertation.

---

[1] A group is an algebraic structure that consists of a set with a binary operation that has a unit and inverse elements. That is not the group mentioned here, of course ☺

It is estimated that there are 10^{10}-10^{12} neurons in the brain. It is commonly believed that electrical signals are used in all brain function. Electrical activity is caused by the flow of ions through proteins embedded in the cell membrane such as ion channels (see 1.2.3 and 1.4.2) with a mechanism similar to that of an ionic battery (see 1.2.4 and 1.4.1). When the increase in voltage of a neuron is above some threshold, a voltage change occurs in a spike-like signal. This is called the *action potential*, and the signal propagates to other regions of the neuron (see 1.2.5). When an action potential propagates to a terminal of a neuron which is responsible for transmission of signals to another neuron, the change in voltage occurs in the other neuron through a structure called the synapse (see 1.2.7).

1.2.1. Brief Anatomy of a Neuron. A neuron usually consists of a cell body, and processes called dendrites and axons, which are branches growing from the cell body [5]. Pictures of several different kinds of neurons are shown in Figure 1.1. The cell body contains the cell nucleus, in which the genetic material (DNA) of the cell is located. A dendrite carries information to the cell body, while an axon carries information away from the cell body.

1.2.2. Cell Membrane. A neuron is enclosed by a double layer (bilayer) of lipid molecules called the cell membrane. In the cell membrane, lipid molecules are aligned with hydrophilic heads outside and hydrophobic tails inside. The cell membrane prevents substances insoluble in lipid from moving through the membrane and can be viewed as a capacitor. Therefore, the movement of ions such as Na^+, K^+, Ca^{2+}, and Cl^- through the cell membrane, which is important for neural function as discussed in the subsequent subsections, must occur through proteins embedded in the cell membrane called ion channels (see 1.2.3) or ion pumps (see 1.2.6).

1.2.3. Ion Channels. Many types of proteins are embedded in the cell membrane. Among them, one type of protein that is relevant to the dissertation is the *ion channel*. Ion channels are proteins with a pore that allow ions to move into and out of a neuron [5]. The flux of ions through the cell membrane causes a difference in electrical potential between the outside and inside of the cell (following the convention, the electrical potential inside a cell with respect to the outside is called the *membrane potential* and denoted by V in this dissertation). Most of the ion channels are selective for particular kind of ion such as Na^+,

K^+, Ca^{2+}, or Cl^-. The permeability of some ion channels is gated by deformation of the channel protein due to changes in the environment such as membrane potential or changes in concentration of some chemicals (e.g. neurotransmitter; see 1.2.7). Depending on selectivity and gating mechanisms, ion channels can be classified, and many kinds of ion channels have been identified. There are many ion channels of the same kind distributed over the membrane. For example, the estimated density of Na channels in the axon in several kinds of animals ranges from 100 to 3,000 channels/μm^2 [8].

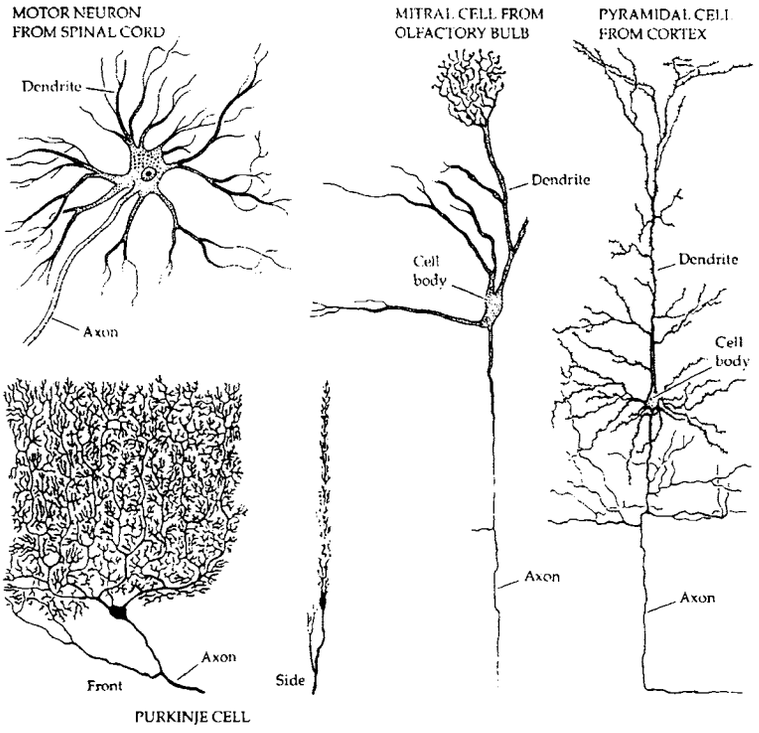

Figure 1.1. Neurons of different kinds. Adapted from Figure 6 in Chapter 1 in [5] with kind permission from Sinauer Associates, ©1992 Sinauer Associates, Inc.

1.2.4. Resting Potential. The membrane potential, when there is no net flow of ions (i.e., current) across the membrane, is called the *resting potential* of a neuron. It is known that the resting potential of a neuron is about -70 mV in physiologically normal conditions. There are two components of this phenomenon. First, there is a concentration difference of ions of a given kind between outside and inside. Types of ions critical for

neurons are Na^+, K^+, and Cl^-, and they have definite patterns for the ratio of concentration outside and inside, although the specific ratio depends on the kind of neuron. For example, Na^+ is more concentrated on the outside of neurons than inside, while the opposite is true for K^+ (see Table 1.1). The other component is that ion channels have selectivity as discussed in 1.2.3. Due to these components, the resting potential is about -70mV, which would cause the flow of ions due to the electrical gradient. However, the net current across the membrane is zero because this ion flow counterbalances the flow due to the concentration gradients. This is explained in more quantitative way in 1.4.1. It is known that the concentration ratio of K^+ is the major determining factor for the value of the resting potential [8].

Table 1.1. Ion concentrations at resting state. Reproduced from Table 6.1 (p.133) in [9] with kind permission from Elsevier, ©1999 Academic Press.

Squid giant axon

	Ion concentration inside the cell (mM)	*Ion concentration outside the cell (mM)*
K^+	400	20
Na^+	50	40
Cl^-	40	560

Mammalian neuron

K^+	135	3
Na^+	18	145
Cl^-	7	120

1.2.5. Action Potential. When the membrane potential of a neuron is raised above some threshold due to either inputs from other neurons or experimentally delivered stimuli, there will be a sudden increase in the membrane potential which lasts on the order of milliseconds, which looks like a spike (Figure 1.2) This is called the action potential

(or informally often called spiking or firing). The generation of the action potential is often described as excitability from the perspective of nonlinear dynamics in the following sense: a perturbation to the membrane potential above the threshold leads to a large transient deviation from the resting potential (see 1.2.4), while a perturbation even slightly smaller than the threshold will not result in a large deviation. The comparison of the two curves in Figure 1.2 shows a clear difference.

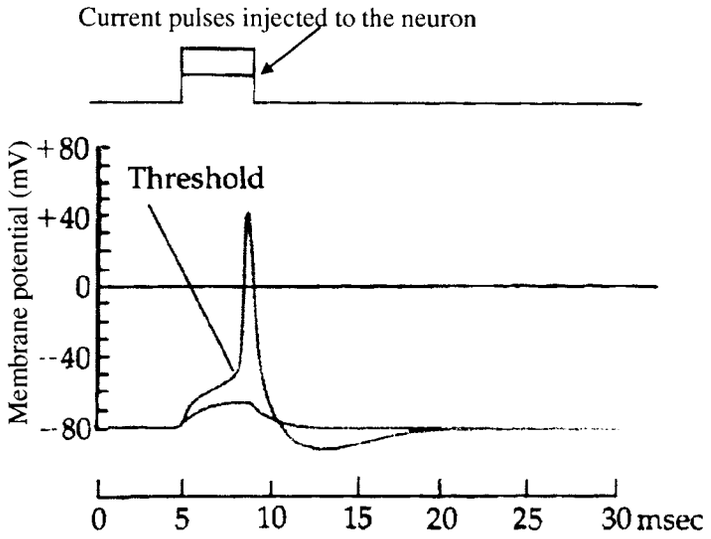

Figure 1.2. An action potential. The membrane potential of a neuron, stimulated with a current pulse, is plotted as a function of time. The top panel shows the current pulses injected to the neuron. Note that the bigger current pulse led to a spike called the action potential while the smaller one did not. The figure is adapted and modified from Figure 4 in Chapter 1 in [5] with kind permission from Sinauer Associates, ©1992 Sinauer Associates, Inc.

Hodgkin and Huxley did a series of experiments and came to the conclusion that the voltage-dependent changes in permeability of Na^+ and K^+ are critical for the generation of the action potential [8]. The mechanism of the action potential can approximately be summarized as follows. When the membrane potential of a neuron is increased above threshold, the permeability of the voltage-dependent Na^+ channel

increases rapidly. This causes the flow of Na^+ into the neuron, due to both the higher concentration of Na^+ outside and negative membrane potential, which is responsible for the upstroke of action potential. This is followed by the increase in the permeability of the voltage-dependent K^+ channel, which causes outward current since K^+ is more concentrated inside, which outweighs the effect of the electrical gradient that would make K^+ ions tend to flow into the cell. A more quantitative explanation of the mechanism of action potential generation is given in 1.4.

1.2.6. Ion Pumps. Ion pumps are membrane proteins that maintain the concentration gradient of a neuron. Although no consideration is given to ion pumps in this dissertation, their role is briefly summarized below because of their functional significance.

When an action potential occurs, Na^+ ions move to the inside and K^+ ions move to the outside of a neuron. Although the movement of the ions due to a small number of spikes may not affect the concentration gradient, without any restoration mechanism, the concentration gradient would eventually change, making the neuron unable to function properly. To maintain the normal (unbalanced) concentration gradient such as shown in Table 1.1, there is a mechanism for pumping ions against their electrochemical gradient. Ion pumps are membrane proteins like ion channels. A major difference between ion pumps and channels is that ion pumps use the energy of ATP (adenosine 5'-triphosphate, which is the source of metabolic energy for all living cells) for transportation of ions, while transportation of ions through ion channels does not require the energy from ATP. The Na^+-K^+ pump transports Na^+ ions out of the cell in exchange for pumping K^+ into the cell in order to maintain a high Na^+ concentration outside and a high K^+ concentration inside. The significance of the Na^+-K^+ pump is shown by the fact that the Na^+-K^+ pump has been estimated to use nearly 25 % of the ATP used in many animals [10].

In this dissertation, it is assumed that the amount of ion flow due to electrical activity of the neurons is so small that concentration of ions does not change. However, accumulation of K^+ outside has been observed during epileptic seizures [11], possibly because the outflow of K^+ due to intensive action potential firing exceeds the inflow of K^+ due to the Na^+-K^++ pump. The reader is referred to, for example, [10,12] for further discussion of the mechanisms of ion pumps.

1.2.7. Neural Communication -- Synapse. Communication between neurons typically occurs through synapses, which can roughly be defined as a link between one neuron and another. There are two types of synapses: chemical and electrical. In electrical synapses, the transmission of a signal occurs through direct flow of current between two neurons while, in chemical synapses, transmission is mediated by a chemical molecule called a neurotransmitter. Major functional differences between electrical and chemical synapses include: 1) there is almost no delay in electrical synapses, while there is delay in chemical ones and 2) the flow of information is bidirectional in electrical synapses while it is unidirectional in chemical ones, as discussed below. The dissertation only considers chemical synapses, since chemical ones are more common than electrical ones in the nervous system, although electrical synapses have also been shown to be important in both brain function and pathology including epileptic seizures.

At electrical synapses, two neurons are physically linked by one type of ion channel, which allows flow of ions from one to the other due to the difference in voltage between them. This is like connecting two neurons with a conducting wire.

At chemical synapses, there is a space between two neurons called a synaptic cleft (see Figure 1.3). The direction of flow of a signal is unidirectional at chemical synapses. The neuron that sends a signal to the other is called a *presynaptic* neuron while the neuron that receives the signal is called a *postsynaptic* neuron. When an action potential (see 1.2.5) in a presynaptic neuron reaches to its synaptic terminal (see 1.2.8 for description of propagation of the action potential along the axon), a chemical called a neurotransmitter is released into the synaptic cleft. The released neurotransmitter reaches the surface of the postsynaptic cell by diffusion. When the neurotransmitter molecules bind to a receptor, which is another type of ion channel, on the postsynaptic neuron, the receptor channel opens. The opening of the channel causes current through it and causes a change in membrane potential. The direction of changes in the membrane potential can be either positive or negative, depending on what kind of neurotransmitter a presynaptic neuron releases. This positive and negative change occurs by the activation of channels permeable to cations (e.g. Na^+) and anions (e.g. Cl^-), respectively. A neuron that releases

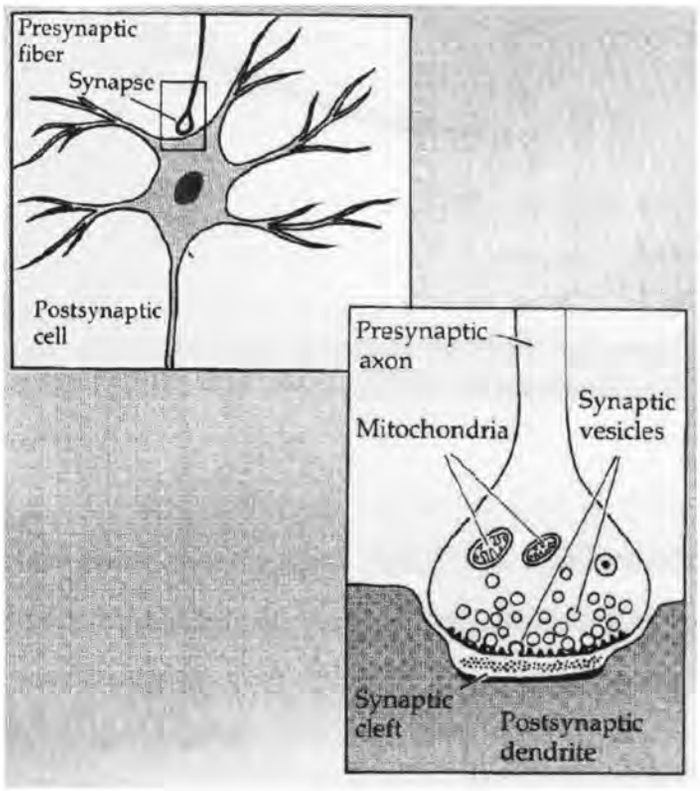

Figure 1.3. Schematic diagram of a chemical synapse. Adapted from Box 2 in Chapter 1 in [5] with kind permission from Sinauer Associates, ©1992 Sinauer Associates, Inc.

neurotransmitter causing a positive voltage change in postsynaptic neuron is called an *excitatory* neuron since it tends to facilitate action potentials in the postsynaptic neuron. The positive change in the membrane potential in the postsynaptic neuron due to this synaptic activity is called the *excitatory postsynaptic potential* (EPSP). On the other hand, a neuron causing a negative change is called an *inhibitory* neuron since it tends to suppress action potentials in the postsynaptic cell, and the negative change in the membrane potential in the postsynaptic neuron is called the *inhibitory postsynaptic potential* (IPSP). EPSPs and IPSPs last for about a few tens to hundreds milliseconds, depending on the type of the receptor on the postsynaptic neuron, which is much longer (though far smaller in amplitude) than the duration of the action potential. An example of EPSP is shown in Figure 1.4. Examples of neurotransmitters for excitatory and inhibitory neurons are glutamate and GABA (γ-aminobutyric acid), respectively.

Figure 1.4. An example of the excitatory synaptic potential. Adapted from Figure 1 in [13] with kind permission from Wiley-Blackwell, ©1956 Wiley-Blackwell.

1.2.8. Electrical Flows in a Neuron. Although a neuron model considered in this dissertation is assumed to be a point without physical size (so-called a single compartment model, see 1.4) for simplicity, this is not the case in a real neuron. Therefore, there is electrical flow within a single neuron.

A simplified picture is as follows. Dendrites (see 1.2.1) which receive inputs from as many as 10,000 other neurons through chemical synapses (see 1.2.7) act as integrators of the inputs. The local membrane potential changes where there is current due to synaptic activities. This non-uniformity of the membrane potential causes diffusion of ions in the network of dendrites as well as diffusion between the inside and outside of the neuron through open ion channels. It is known that the likelihood of an action potential in the dendrite and cell body is small compared to that in the axon due to a different composition of kinds of ion channels from that in the axon. Therefore, while the propagation of an action potential along the axon is a nonlinear process as discussed below, the diffusion process in the dendrites can be modeled by the linear cable equation, which describes a diffusion process in a leaky cable [12].

When sufficiently large excitatory inputs (i.e., inputs that cause an increase in the membrane potential) are received over the dendrites to increase the membrane potential above the threshold, an action potential (see 1.2.5) initiates, typically at the initial segment of the axon from the cell body [14]. An action potential in one place causes an increase in the membrane potential in neighboring places in the axon through diffusion. This causes an increase in the permeability of voltage-dependent Na^+ channels and, thus, triggers an action potential in the neighboring places. This process is a nonlinear process and can be

modeled as a nonlinear cable equation, which can produce traveling waves of electrical excitation [12].

When an action potential propagates to the end of the axon, neurotransmitters are released into the synaptic cleft of the synapse at the axon terminal. This causes membrane potential changes in the dendrites onto which the axon makes its synaptic connections.

1.2.9. Neocortex. Since Sections 3 and 4 focus on neocortical seizures, some facts about neocortical networks are provided in this section. The neocortex is the outer region of the mammalian brain and is responsible for higher functions such as sensory perception (i.e., interpretation of a sensory stimulus such as light and sound) and motor control (i.e., moving limbs and eyes). The name, neocortex, comes from the fact that it is part of the cerebral cortex which was most recently acquired in evolution.

1.2.9.1 Laminar structure of neocortex. The neocortex consists of six layers, each of which spans in parallel to the brain surface and is numbered sequentially from the most superficial layer. The classification of the layers is based on the types of neurons in each layer (see Figure 1.5) and each layer has a different role [6]. In layer 1 there are few cell bodies of neurons. Layers 2 and 3 have mostly pyramidal neurons (explained in the next subsection), and make output connections to other cortical regions. Many non-pyramidal neurons are located in layer 4 and receive input primarily from the thalamus, a deeper structure in the brain whose role includes relaying sensory and motor information to the neocortex. The largest pyramidal neurons exist in layer 5 and their long axons make output connections to regions such as the basal ganglia and spinal cord. Layer 6 contains neurons whose output goes to the thalamus.

1.2.9.2 Morphological classification of neocortical neurons. Neurons have been classified in terms of morphological and electrophysiological properties. From a morphological point of view, neocortical neurons can be classified into two categories: *pyramidal neurons* and *non-pyramidal neurons* [6]. Both types can be further classified into subcategories and the reader is referred to, for example, [15] for more detail.

Pyramidal neurons have a pyramid-shaped cell body, from which the name derives (see Figure 1.5). The apex of their cell body is oriented toward the surface of the brain. The axons of pyramidal neurons make both local and long-range connections. The main trunks of their axons connect to a distant region of the neocortex, or to other structures in

the nervous system, while there are several branches from the main trunk which end near the cell body. All the output from the neocortex is through pyramidal neurons [15].

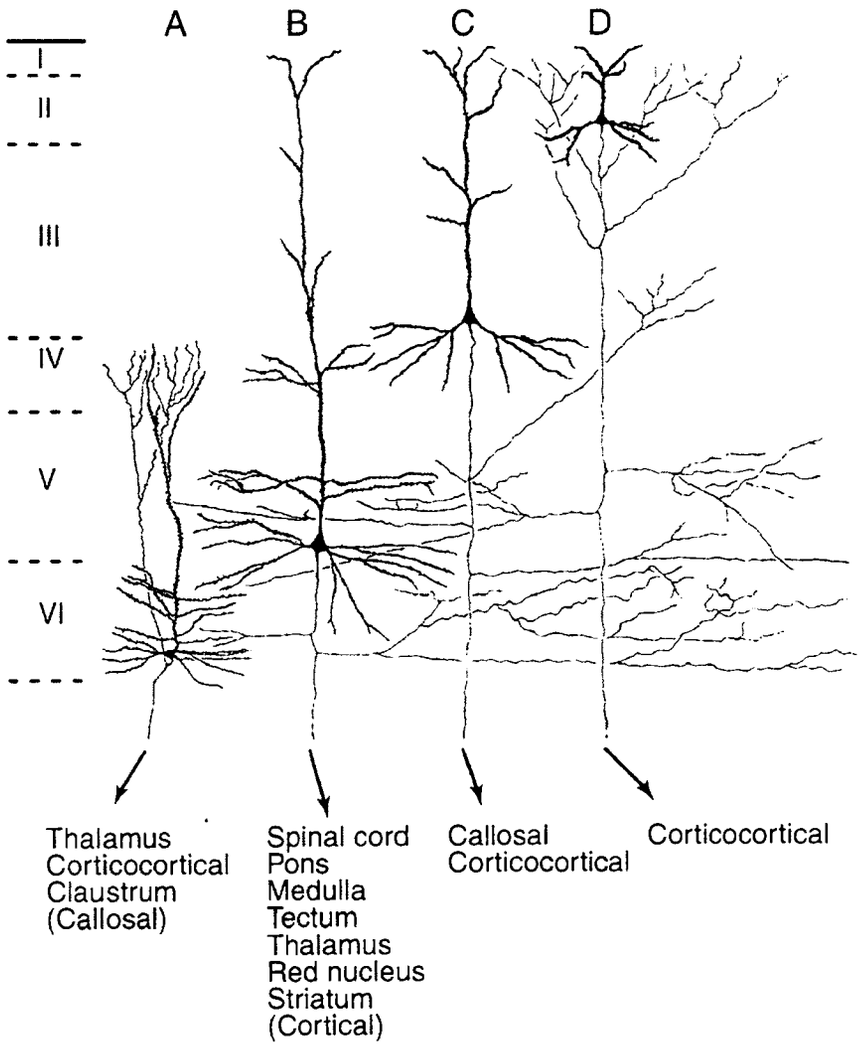

Figure 1.5. The laminar structure and locations of pyramidal neurons in the neocortex. Adapted from Figure 8 (p.535) in [16] with kind permission from Springer Science and Business Media, ©1984 Plenum Press.

Non-pyramidal neurons have round and smaller cell bodies. The axon of a non-pyramidal neuron makes local connections: it usually terminates near its cell body and rarely goes further. Input from other regions of the brain is received by non-pyramidal

neurons. Therefore, the main roles of non-pyramidal neurons are local information processing and receiving input from other regions in the brain.

1.2.9.3 Electrophysiological classification of neocortical neurons. It is a common experimental technique to apply a constant stimulus current to an isolated neuron. In such an experiment, without stimulus current, the neuron does not show an action potential and the membrane potential stays constant, called the resting potential (see 1.2.4). When the stimulus is kept above some threshold, the neuron shows periodic action potentials. Based on its spiking patterns, neurons are mainly classified into four classes [17, 18].

Regular-spiking neurons are characterized by a tonic spiking pattern with higher frequency of spikes at the beginning of a stimulus. They are mostly pyramidal neurons. The majority of neocortical neurons are regular-spiking neurons. *Intrinsically bursting* neurons, which are pyramidal neurons, show clustered patterns of action potentials, called *bursts*, followed by a pause and a tonic spiking pattern. *Fast-rhythmic-bursting* neurons produce a sequence of bursts at 30-40 Hz and they are either pyramidal or non-pyramidal cells. *Fast-spiking* neurons give rise to a tonic spiking with much faster rate than regular-spiking neurons and with a thin shape of action potentials. Among those four classes of neurons, only fast-spiking neurons are inhibitory neurons, while the rest are excitatory (see 1.2.7 for the definition of the excitatory and inhibitory neuron). Having said that neurons can be classified into the four classes, recent evidence has shown that firing patterns can be changed from one to another under some conditions [18].

1.2.9.4 Some statistics of neocortical neurons. Some statistics of neocortical neurons are briefly summarized. All the data here comes from [19], to which the reader is referred for more detail.

The density of neurons in the brain varies from animal to animal, and from place to place. In general, the number of neurons per unit volume is lower in larger brains. In the mouse neocortex, the density of neurons is estimated to be 10^4 to 10^5 neurons/mm^3. The average number of synapses per neuron in the mouse neocortex is estimated to be 2,300 to 8,000 while, in humans, it is estimated to range from 24,000 to 80,000.

There are data which suggest that the estimated length of axons of the pyramidal cell in the mouse cortex ranges from less than 1 mm to 17 mm and that the most frequent

length range is 1 to 2 mm. However, the authors also warn that the result may change dramatically from the actual distribution because of the fact that they have to estimate the length of axons based on a correction formula since the thickness of their section sample is often much smaller than the length of axons.

1.2.10. Synchronization in the Brain. Synchronization of electrical activity is ubiquitous in many aspects of brain function. Only a small fraction of synchronization phenomena are summarized below. For a more comprehensive review, the reader is referred to, for example, [20].

Many studies have suggested that synchronization of electrical activities are critical for normal brain function such as visual perception [21], associative learning [22] and memory consolidation [23], to name a few.

It has been shown that neural synchrony may be critical in the development of the brain. There is synchronized spontaneous neural activity in the neonatal neocortex [24], while desynchronized neural activity is observed in the mature neocortex [25].

Although neural synchrony is crucial to brain function, it can also cause pathologies in the brain. There have been lines of evidence that show abnormal neural synchronization is associated with some brain disorders such as autism, schizophrenia, Alzheimer's disease and Parkinson's disease [20].

Epilepsy [26] has traditionally been considered to result from excess and/or synchronized electrical activity in the brain, although several studies have recently suggested that this may not necessarily be the case (see 3.1 for more discussions).

1.2.11. Epileptic Seizures. Since Sections 3 and 4 concern one particular type of epilepsy which is artificially induced in the rat, some basic knowledge about epilepsy is provided in this subsection. The following subsection (1.2.11.1) explains a definition of epilepsy and epileptic seizures. Some facts and terminology are explained in 1.2.11.2. Animal models, which have been used to complement studies in human epileptic patients, are briefly summarized in 1.2.11.3. The primary focus of Sections 3 and 4 of this dissertation is a particular animal model in which a K^+ channel blocker is locally applied. This particular animal model is described in 1.2.11.4.

1.2.11.1 Definition of epilepsy. Epilepsy is not a specific type of disease, but a category of symptoms of disordered brain function [27]. According to the definition

proposed by the International League Against Epilepsy and the International Bureau for Epilepsy [28], an epileptic seizure is "a transient occurrence of signs and/or symptoms due to abnormal excessive or synchronous neuronal activity in the brain" and epilepsy is "a disorder of the brain characterized by an enduring predisposition to generate epileptic seizures and by the neurobiological, cognitive, psychological, and social consequences of this condition".

1.2.11.2 Clinical aspects of epileptic seizures. The estimated average annual incidence of epilepsy is 28.9 to 53.1 per 100,000 population [29]. There are many factors that can cause epilepsy: brain injury, developmental malformation, genetic factors, and so on [27].

Characterization of epileptic seizures has been performed based on electrical activity in the brains of epileptic patients recorded with the electroencephalogram (EEG) [27]. Seizures are generally classified into two categories: focal and generalized seizures. *Focal seizures* (also called partial or local seizures) are those where the changes in electrical activity at clinical onset are confined to a local region in one cerebral hemisphere. *Generalized seizures* are those where the changes in electrical activity at a clinical onset occur in both cerebral hemispheres. Those two types are further categorized into subtypes, which is beyond the scope of this dissertation. The reader is referred to [27] for more detailed classification of seizures.

1.2.11.3 Experimental animal models of epileptic seizures. To study the neurological mechanisms of epileptic seizures, research on human epilepsy would be an ideal approach and, in fact, extensive research has been done on human epileptic patients. However, the study of human epileptic patients has several drawbacks [30]. First, the application of invasive techniques in human patients is limited by ethical constraints. Second, it is difficult to have good controls of physiological variables. Finally, statistical analysis may require a larger number of patients than that in clinical studies. As alternative and complementary approaches, animal models of epileptic seizures, where epileptic seizures are artificially caused by a researcher, have been widely studied. Studies using animal models of epilepsy have also been used to investigate oscillatory neural mechanisms commonly seen in a normal brain [30].

Animal models can be divided into two classes: acute models and chronic models. In acute models, epileptic seizures are induced in otherwise normal animals. Methods for acute animal models include the application of electroshock, and the application of chemicals that increase excitability of neurons [30]. Acute models can provide hypotheses about neural mechanisms of seizure events at molecular, cellular, and network levels.

Chronic models are aimed to investigate long-term and progressive changes caused by chronic occurrence of epileptic seizures. Methods for chronic animal models include kindling (chronic application of electrical or chemical stimulations that causes progressive increase in the frequency and/or severity of seizures), application of metals such as alumina and cobalt acids, and other materials such as tetanus toxin. Genetic models have received increasing attention. Some genetic models are similar to human genetic epilepsies.

1.2.11.4 4-aminopyridine epileptic seizures. This subsection is devoted to one specific type of animal epilepsy model which is used in Section 3, and of which a computational model is constructed in Section 4. 4-aminopyridine (4AP) is a blocker of K^+ channels (see 1.2.3). At a single cell level, 4AP is known to increase the duration of the action potential (see 1.2.5) [31]. As a result of the prolonged duration of the action potential, there is an increase in the amount of neurotransmitter released at the synaptic terminals of both excitatory and inhibitory neurons, which leads to an increase in amplitude of both excitatory and inhibitory postsynaptic potentials (see 1.2.7) in postsynaptic neurons. At a network level, it is known to cause epileptic activity when applied to the brain in vivo or to brain slices [32].

1.3. MEASUREMENT OF NEURAL SIGNAL

In this subsection, techniques to measure electrical activity which are relevant to this dissertation are described.

1.3.1. Local Field Potential. The *local field potential* (LFP) recording is one type of measurement of electrical activity in the neural system, called the extracellular recording, and measures the electrical potential at one location in the brain with respect to a reference point. In extracellular recordings, the tip of an electrode in the brain is in the extracellular space, meaning that the tip is outside the neurons, while, in the intracellular

recording, the tip of the electrode is inside the neuron. In practice, in the case of a live animal as in Section 3, both measurements can be done by inserting an electrode in a place inside the brain while setting another electrode on somewhere in the animal's body as a reference.

The local field potential is the low frequency component (less than 300 Hz) of the extracellular recording. It is widely believed that the local field potential reflects mainly the electrical potential due to synaptic current (see 1.2.7) of a population of neurons, while the high frequency component (300-10,000 Hz) of the extracellular recording reflects the electrical potential due to action potentials (see 1.2.5). This is presumably due to the fact that the time scale of the synaptic potential (an order of 10-100 milliseconds) is much slower than that of the action potential (an order of millisecond).

Although the intracellular recording is experimentally more delicate than the extracellular recording, it is relatively simple to interpret signals from the intracellular recording. The intracellular recording essentially measures the membrane potential of a cell into which an electrode is inserted. When an action potential (see 1.2.5) occurs, the signal from the measurement looks like the membrane potential simulated by a Hodgkin-Huxley type model. While the extracellular recording is less delicate to perform, its interpretation is not straightforward, since it typically reflects the electrical activity from a population of neurons. Even when an extracellular recording is made from an isolated single neuron, its signal looks very different from that with an intracellular recording. For example, during an action potential in a neuron, the signals from the extracellular recording close to the neuron show a triphasic signal rather than a single spike-like signal.

Although the theoretical basis for extracellular recording in the brain is yet to be understood, an extensive amount of research in from both theoretical and experimental aspects has provided some knowledge about extracellular recording in the brain. A most simplified model of the extracellular recording is briefly discussed below [33]. The first principle for the extracellular recording is the Maxwell equations. Several approximations are made for the model discussed here. First, since the physiologically relevant frequency range of the signals are low (less than 10,000 Hz), the effect of magnetic induction is negligible. Therefore, the problem can be treated as one of electrostatics. Second, although the cell membrane acts as a capacitor (see 1.2.2) and the role of the capacitance is very

critical in the dynamics of a neuron (see 1.4.4), some experimental data support that, for local field potential measurement, capacitive effects of the brain tissue are negligible and, therefore, the brain can be viewed as purely resistive. Third, conductivity of the medium is assumed to be homogeneous and isotropic. Finally, Ohm's law holds (i.e., $\vec{J} = \sigma\vec{E}$ holds).

Consider a synapse where the excitatory synaptic activity occurs as shown in Figure 1.6 (see 1.2.7 for the explanation of the neuroscience terms). The excitatory

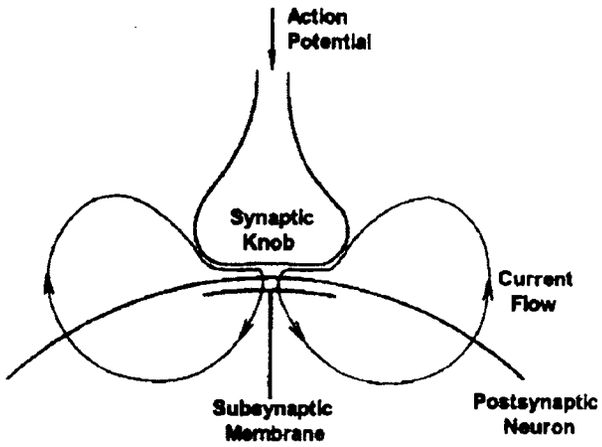

Figure 1.6. Membrane current caused by excitatory synaptic current. The inward current at the synapse causes outward current at distant places. Adapted from Figure 4-6 (p.164) in [24] with kind permission from Oxford University Press, ©2006 Oxford University Press, Inc.

synaptic current increases the membrane potential at the location where positive ions flow into the postsynaptic neuron. This creates the gradient in the membrane potential in the postsynaptic neuron. Positive ions diffuse to neighboring places and some of them leak out of the neuron (see 1.2.8) until the system comes back to the steady state (i.e., the membrane potential comes back to the resting potential, see 1.2.4). This process creates current sources and sinks distributed on the membrane of the postsynaptic neuron. Therefore, the electrical potential at a point in the extracellular space is determined by the summation of the potentials created by such current sources. Assuming that each current

source is spherically symmetric, the electrical potential at a given point in the brain can be expressed by the following equation

$$\Phi(\vec{r},t) = \frac{1}{4\pi\sigma}\sum_{n=1}^{N}\frac{I_n(t)}{R_n}, \tag{1}$$

where σ is the conductivity of the medium, $I_n(t)$ is the n^{th} current source, and R_n is the distance between the point where the measurement is made and the point of the source. Therefore, by knowing the distribution of the current sources, the electrical potential at a given point can be calculated. However, the electrical potential at a given point is highly affected by the geometry of neurons, as discussed later.

Consider the two different neural geometries shown in Figure 1.7. In Figure 1.7A, neurons are lined up parallel to each other. In this case, the synchronized synaptic current forms a dipole layer, which creates a large electric field. On the other hand, when neurons are located in a radially symmetric manner as in Figure 1.7B, the electric field outside the population of neurons tends to be small. In the case of the neocortex, pyramidal neurons are aligned perpendicular to the surface of the brain. Therefore, a configuration like Figure 1.7A might give a good approximation.

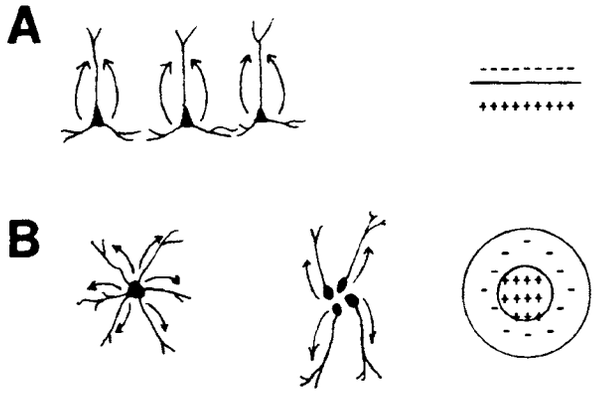

Figure 1.7. Different geometries of neurons and their corresponding electrostatic models. Adapted from Figure 3 (p.289) in [34] with kind permission from Springer Science and Business Media, ©1990 The Humana Press Inc.

Suppose that a microelectrode is placed above the layer of N neurons as in Figure 1.7A and that the dipole moment from each current source is changing periodically with the identical frequency. Consider two situations: all the dipole moments oscillate (1) in phase and (2) with random phases. Then, it is expected that the electrical potential in the case (1) is proportional to N, while the potential in the case (2) is proportional to $\sqrt{N}$ [35]. This indicates that the local field potential measurement may mostly reflect in-phase synchronous activity of neurons, if this activity is occurring.

1.3.2. Voltage-Sensitive Dye Imaging. Voltage-sensitive dyes are molecules which sit in the cell membrane and emit fluorescence in response to changes in the membrane potential.

Voltage-sensitive dyes have been widely used in the measurement of electrical activity in the neural system. At a single-cell level, it has been experimentally shown that the fluorescence correlates linearly with the membrane potential [28]. At a population level, several patterns, such as propagating waves, are observed [31].

The dye which is used in the experiment in Section 3 is called RH-1961. This dye, also called a blue dye, has been specifically developed for the measurement of electrical activity in in vivo brain imaging as an improvement from more traditional dyes such as RH-795. RH-1691 can be excited with a longer wavelength than the absorption wavelength of hemoglobin. Thus, using RH-1691 reduces the noise due to hemodynamics such as the changes in reflectance caused by local blood volume change more than older dyes [36, 37]. The use of such blue dyes is particularly important in seizure studies, where each seizure is a unique event, and thus imaging trials cannot be averaged in order to improve signal-to-noise ratio.

1.4. BIOPHYSICS OF SINGLE NEURON DYNAMICS

This subsection is devoted to explaining how a model for single neuron dynamics can be built. This formalism explained here was originally developed by Hodgkin and Huxley (known as the Hodgkin-Huxley equations) and called a conductance-based model, where the membrane potential dynamics is described by the change in current through ion channels (or changes in conductance of ion channels).

As mentioned before, in this dissertation, a single neuron is modeled as an object without size, in the sense that a single variable describes the membrane potential of an entire neuron, as opposed to an object where different places in a single neuron can have different voltages. This is called a single-compartment model. The focus of this subsection is restricted to a single-compartment, conductance-based model. There are other types of models such as multi-compartment, conductance-based models, where a single neuron is modeled with more than one segment [38], and population models, where the dynamics of activity of a local population of neurons is described as a function of time and space [39].

A single-compartment conductance-based model is equivalent to an electrical circuit with a capacitor and variable resistors. In the Hodgkin-Huxley model, voltage-dependent Na^+ and K^+ channels are essential for an action potential to occur. To understand how this circuit generates an action potential (see 1.2.5), several notions have to be explained.

1.4.1. Nernst Potential. The selectivity of ion channels mentioned in 1.2.3 is the basis of electrical phenomena in neurons. Consider a system where a container of solution is separated into two compartments by a membrane, as shown in Figure 1.8. The container is filled with liquid containing two ions, K^+ and A^- (A^- can be any monovalent anion). Each compartment has the same amount of K^+ and A^-, so that the total charge is zero in each container. However, the concentration of the salt is larger in one container (say, left) than the other (right). The membrane has pores that are permeable only to K^+. At the beginning of this process, the electrical potential difference between the two compartments is zero. However, it is expected that K^+ diffuses into the right side due to the concentration difference. Since A^- ions cannot move through the membrane, diffusing K^+ ions into the right side makes the electrical potential of the right side higher, which drives K^+ ions to move toward the left. So, there are two opposing driving forces for the transfer of K^+ ions, and the question of interest is what the equilibrium potential difference between the two compartments will be.

Applying the Boltzmann distribution or equating the Gibbs free energy to zero for the system, the equilibrium potential V_K is determined by the Nernst equation:

$$V_K = E_{Left} - E_{right} = \frac{RT}{zF} \ln \frac{[K_{right}]}{[K_{left}\}} \tag{2}$$

where R is Boltzmann's constant, T is temperature, z is valence, and F is the Faraday constant. This means that, when the measured potential is equal to the equilibrium potential, there is no net flow of K^+ ions between the two compartments. Based on the mammalian cell values in Table 1.1, the equilibrium potentials for K^+, Na^+, and Cl^- are -102, 55.7, and -75.9 mV, respectively.

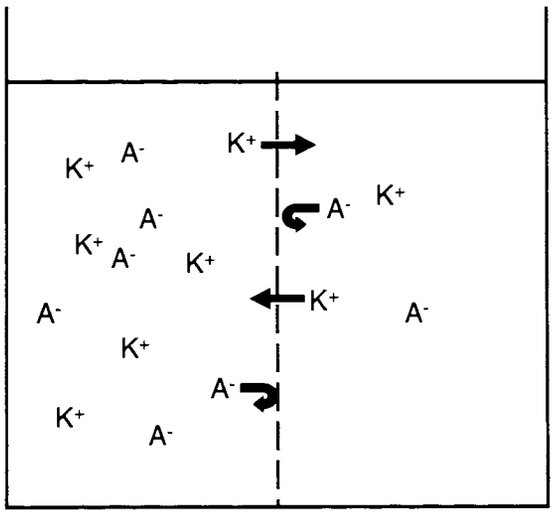

Figure 1.8. A container with a permeable membrane only to K^+.

Although perfect selectivity is assumed in the neural models used in this dissertation, it is worth discussing the case of imperfect selectivity from the physics point of view. In reality, an ion channel is not perfectly selective to one kind of ion. Assume a collection of ions rather than K^+ and A^- and imperfect selectivity of pores. In this case, the final membrane potential where the net current is zero (the resting potential) has to be modified. Using electro-diffusion theory with a few assumptions [8, 12] and assuming that

only K^+, Na^+, and Cl^-, which are physiologically relevant, are permeant to the membrane, the resting potential is give by the Goldman-Hodgkin-Katz (GHK) equation:

$$V_{GHK} = \frac{RT}{F} \ln \frac{P_K[K^+]_{out} + P_{Na}[Na^+]_{out} + P_{Cl}[Cl^-]_{in}}{P_K[K^+]_{in} + P_{Na}[Na^+]_{in} + P_{Cl}[Cl^-]_{out}} \tag{3}$$

where P_i is the relative permeability for ion i (this has to be measured experimentally). Although the GHK equation looks similar to the Nernst equation (Eq. 2), the two equations are derived based on totally different principles [8]. The Nernst equation derives the voltage at equilibrium, which can be derived from thermodynamics (Gibbs free energy) or the Boltzmann distribution. On the other hand, when more than one kind of ion can go through the pores at the resting potential (see 1.2.4), the net flow of each ion species is not necessarily zero, even though the net flow of all the ions is zero. Therefore, this is a non-equilibrium problem and the treatment for the derivation of the GHK equation is far more complicated than the Nernst equation. The GHK equation is derived as the steady state for the net current in the differential equations that describe the dynamics of the current through pores based on electro-diffusion theory. The Nernst potential can also be derived from GHK equation as the special case of the pores being perfectly selective to only one kind of ion [12].

1.4.2. Dynamics of Voltage-Dependent Ion Channel. To model the current through ion channels, the dynamics of an ion channel must be considered. The ion channel of interest here is the voltage-dependent channel, whose dynamics of opening and closing depends on the membrane potential V. Consider a simple model which consists of two states of an ion channel, the open and closed state,

$$C \rightleftharpoons O, \tag{4}$$

where C and O refer to the closed state and open state, respectively. The transition between them corresponds to a conformational change in the channel protein. Assume that there are N channels of this kind on a neuron and define the number of open and closed

channels at time t as $N_O(t)$ and $N_C(t)$, respectively. Since the total number of channels should be preserved,

$$N_O(t) + N_C(t) = N . \tag{5}$$

Since the ion flow is the sum of the currents through each ion channel as stated in Eq. 14 below, an equation governing the time course of the fraction of open channels would determine the current through the channels at a given time.

To obtain an equation for the dynamics of the fraction of open channels, the law of mass action, which is an empirical law which states that the reaction rate in a single-step reaction is proportional to the concentration of the reactants [40], is employed. It is natural to refer to the fraction of open channels as "concentration", denoted as f ($=N_O/N$). Then, from Eq. 5, the fraction of closed channels is given by 1-f. By the law of mass action, the rate of transitions from the state C to O, denoted as j_+, can be written as

$$j_+ = k^+(1-f) \tag{6}$$

where k^+ is the proportionality constant for the transition rate. Similarly, the rate of transitions from the state O to C, denoted as j_-, can be written as

$$j_- = k^- f \tag{7}$$

where k^- is the proportionality constant for the transition rate. Then, the equation for the dynamics of the fraction of open channels becomes as follows:

$$\begin{aligned} \frac{df}{dt} &= j_+ - j_- \\ &= -k^- f + k^+(1-f) \\ &= -(k^- + k^+)\left(f - \frac{k^+}{(k^- + k^+)} \right). \end{aligned} \tag{8}$$

(Note that an implicit assumption made, in order to apply the law of mass action, is that the number of molecules involved is very large, which may not be necessarily the case for ion channels on a neuron. If the number of channels are not so large, some stochasticity is expected, rather than the deterministic dynamics described by Eq. 8. A stochastic version of the dynamics of this system is considered in Section 5.2 and it is shown that, in the limit of $N \to \infty$, the deterministic equation (Eq. 8) can be recovered.) Define $\tau = 1/(k^- + k^-)$ and $f^\infty = k^+/(k^- + k^-)$. For voltage-gated channels, k^+ and k^- are a function of V and, therefore, so are τ and f^∞. Then, Eq. 8 becomes

$$\frac{df}{dt} = \frac{-(f - f^\infty(V))}{\tau(V)}. \tag{9}$$

If V is kept constant, f reaches f^∞ with time constant τ, which is similar to the dynamics of charge stored in a capacitor in the RC circuit.

To see the explicit form of voltage dependence of τ and f^∞ in Eq. 9, the dependence of k^+ and k^- on V should be determined. Using the Arrhenius equation[2], which is an empirical law to describe the temperature dependence of the reaction rate constant [8], the rate constants k can be expressed as

$$k \propto \exp\left(\frac{-E_a}{RT}\right) \tag{10}$$

where E_a is the activation energy of the reaction. For a voltage-gated channel, the membrane potential V affects the rate constants for the transition between the open and closed states. Therefore, k^+ and k^- can be written as

$$k^+ = k_O^+ \exp(-\alpha V),\ k^- = k_O^- \exp(-\beta V) \tag{11}$$

---

[2] The rate constant can be obtained using a more theoretical approach, the transition state, which is beyond the scope of this dissertation

where $k_O^+, k_O^-, \alpha,$ and β are constants. Then, after some algebraic manipulation, τ and f^∞ can be written as [41].

$$f_\infty = 0.5(1 + \tanh(V - V_O)/2S_O)$$
$$\tau = \frac{\phi}{\cosh((V - V_O)/2S_O)} \tag{12}$$

where $S_O = 1/(\beta - \alpha)$ and $V_O = \ln(k_O^- / k_O^-)/(\beta - \alpha)$.

1.4.3. Ionic Current. Based on the discussion of the Nernst potential (1.4.1), the simplest approximation for the current through a single ion channel, if it is open, is represented by Ohm's law, taking the difference in voltage with respect to the Nernst potential:

$$i = g_n^{single}(V - V_n) \tag{13}$$

where n is the subscript for the n^{th} kind of ion channel, g^{single} is the conductance of the single ion channel and V_n is the equilibrium potential for the kind of ion permeant to the n^{th} kind of ion channel. Assume that there is a collection of channels of the same kind with the number N_n. Let f_n be the fraction of open channels (an implicit assumption here is that N_n is large enough to be able to treat the fraction as a continuous variable). The number of open channels is given by $N_n f_n$. Then, the total current through the n^{th} kind of channel is

$$I_n = N_n f_n g_n^{single}(V - V_n) \tag{14}$$

By defining the maximal conductance g_n as $g_n = N_n g_n^{single}$, Eq. 14 becomes

$$I_n = g_n f_n (V - V_n), \tag{15}$$

which will be used for the equivalent electrical circuit in the next subsection. It is known that there is a deviation from the linear relationship between the voltage and current

through ion channels (Eq. 15). The reader is referred to [8] for the discussion of nonlinearity in the current-voltage relationship.

1.4.4. The Membrane Model. It is widely accepted that the dynamics of the membrane potential can be reliably modeled by an equivalent electrical circuit (Figure 1.9). In this circuit, the lipid double-layer cell membrane is modeled as a capacitive element and is arranged with the ionic currents discussed in 1.4.3. By Kirchhoff's law, the equation for the dynamics of the membrane potential is

$$\begin{aligned} I_{app} &= \sum_{n=1}^{N} I_n + C\frac{dV}{dt} \\ &= \sum_{n=1}^{N} g_n f_n (V - V_n) + C\frac{dV}{dt} \end{aligned} \tag{16}$$

where I_{app} is an externally applied current, C is the capacitance of membrane, and, for the second equality, Eq. 15 is used. Rearranging the equation to a more standard form gives

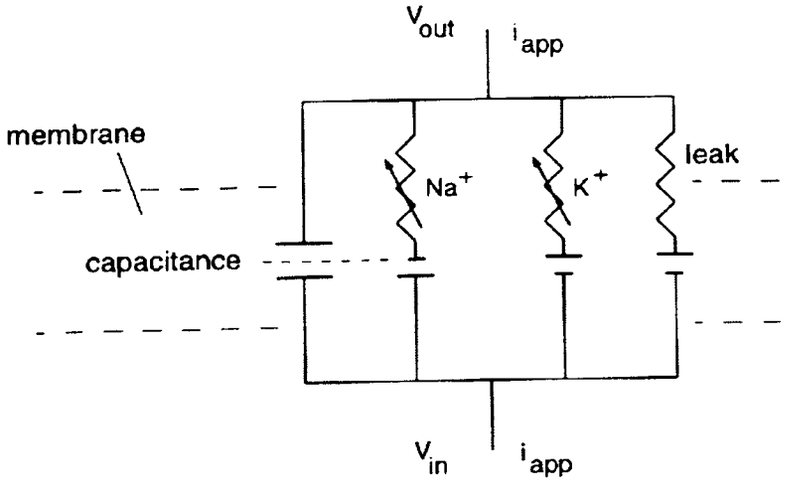

Figure 1.9. An equivalent electrical circuit to the membrane model. Adapted from Figure 2.4 (p.27) in [41] with kind permission from Springer Science and Business Media, ©2002 Springer-Verlag New York, Inc.

$$C\frac{dV}{dt} = -\sum_{n=1}^{N} g_n f_n (V - V_n) + I_{app}. \tag{17}$$

Eq. 17, with the differential equations for the fraction of open channels (Eq. 9), forms a model for the dynamics of a single neuron.

1.4.5. "Canonical" Form of Conductance-Based Model. Based on the discussion up to this subsection, a single-compartment, conductance-based model can be written in the following "canonical" form:

$$\begin{aligned} C\frac{dV}{dt} &= -\sum_{n=1}^{L} g_n f_n (V - V_n) + I_{app} \\ \frac{df_1}{dt} &= -\frac{(f_1 - f_1^{\infty}(V))}{\tau_1(V)} \\ &\vdots \\ \frac{df_L}{dt} &= -\frac{(f_L - f_L^{\infty}(V))}{\tau_L(V)} \end{aligned} \tag{18}$$

where L represents the number of kinds of ion channels (n=1, 2,..., L), V is the membrane potential, and g_n and f_n are the maximum conductance and the fraction of open channels for the n^{th} kind of ion channel, respectively. The differential equation for V is derived from Kirchhoff's law (Eq. 17) and the other equations are derived from the dynamics of ion channels (Eq. 9). One of the simplest conductance-based models is provided in the next subsection as an example.

1.4.6. Example: Morris-Lecar Equations. The first and most famous conductance-based model is the Hodgkin-Huxley equations. In this subsection, however, a simpler model, the Morris-Lecar (ML) equations [42], is presented for illustration. The model is proposed for the electrical activity of the barnacle muscle fiber. Thus, it is not technically a neural model. However, the equation works in a very similar way to a neural model.

The model consists of two kinds of ion channels, Ca^{2+} and K^+. In the case of neural models with a minimal setting, Na^+ and K^+ are usually considered. Ca^{2+} in this model qualitatively behaves in the same way as the Na^+ current in neural models. The model has

three kinds of ion channels: Ca^{2+}, K^+, and leakage channels. The equations have the following form:

$$\begin{aligned} C\frac{dV}{dt} &= -g_{Ca}m(V-V_{Ca}) - g_K w(V-V_K) - g_L(V-V_L) + I_{app} \\ \frac{dm}{dt} &= -\frac{(m-m_\infty(V))}{\tau_m(V)} \\ \frac{dw}{dt} &= -\frac{(w-w_\infty(V))}{\tau_w(V)}, \end{aligned} \tag{19}$$

where g_i represents the maximal conductance for each kind of channel, as in Eq. 15, m and w are the fraction of open channels for the Ca^{2+} and K^+ channels, respectively, and $m^\infty(V)$ and $w^\infty(V)$ are the steady-state fraction of the Ca^{2+} and K^+ channels, as explained in Eq. 9, respectively. A crucial approximation will be made to obtain a reduced set of the equations, which makes the analysis of this model more tractable. Based on the fact that the characteristic time scale for the dynamics of the Ca^{2+} channel ($=\tau_m(V)$) is much shorter than that for the K^+ channel ($=\tau_w(V)$), i.e., m changes much faster than w, the assumption is made that the fraction of open Ca^{2+} channels ($=m$) reaches its steady-state value ($=m^\infty(V)$) without a time lag. This can be done by replacing m in the first equation in Eq. 19 by $m^\infty(V)$. In words, the fraction of open Ca^{2+} channels is no longer a function of time, but a function of the membrane potential. The reduced set of equations can be written as:

$$\begin{aligned} C\frac{dV}{dt} &= -g_{Ca}m_\infty(V)(V-V_{Ca}) - g_K w(V-V_K) - g_L(V-V_L) + I_{app} \\ \frac{dw}{dt} &= -\frac{\phi(w-w_\infty(V))}{\tau(V)}, \end{aligned} \tag{20}$$

where m_∞ and w_∞ are defined as follows:

$$
\begin{aligned}
m_\infty &= 0.5(1+\tanh((V-v_1)/v_2)) \\
w_\infty &= 0.5(1+\tanh((V-v_3)/v_4)) \\
\tau &= 1/\cosh((V-v_3)/(2v_4))
\end{aligned}
\tag{21}
$$

and the values of the parameters used here are taken from [41]. By the reduction of the dimension of the system from 3 to 2, the variables that describe the system can be plotted in a plane, which is called the phase plane, rather than a 3-dimensional space.

One important feature of neural dynamics, excitability (see 1.2.5), can be observed in this model. Figure 1.10 shows the time course of the response of the membrane potential V to an injection of a brief current pulse for 10 msec with two different amplitudes 100 and 150 pA, i.e., set I_{app}=100 or 150 at t=300 to 310 and I_{app} =0, otherwise. The current injection can be assumed to be artificially given by an experimenter. The injection of a larger current pulse (150 pA, see Figure 1.10 *right*) leads to a large transient change in the membrane potential (action potential). Note that the transient change of the membrane potential lasts even after the injection of the current pulse. On the other hand, with an injection of a smaller current pulse for the same duration (100 pA, see Figure 1.10 *left*), the membrane potential returns to the resting potential without a large deviation. The difference between the two conditions is prominent when the time course of the two variables (V, w) is plotted in the phase plane (Figure 1.11).

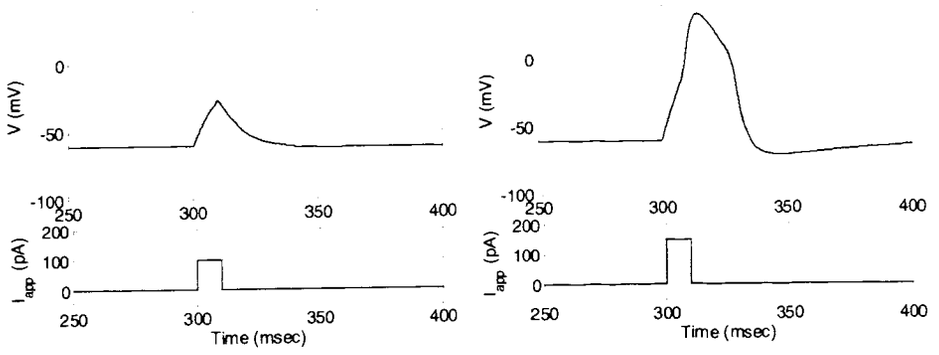

Figure 1.10. Response to a brief current injection in the ML model. *Left*: the top graph shows the time course of the membrane potential responding to a brief current pulse at 100 pA while the bottom graph shows the timing of the current pulse. *Right*: the same graphs as the left are shown, except that the current pulse has an amplitude of 150 pA.

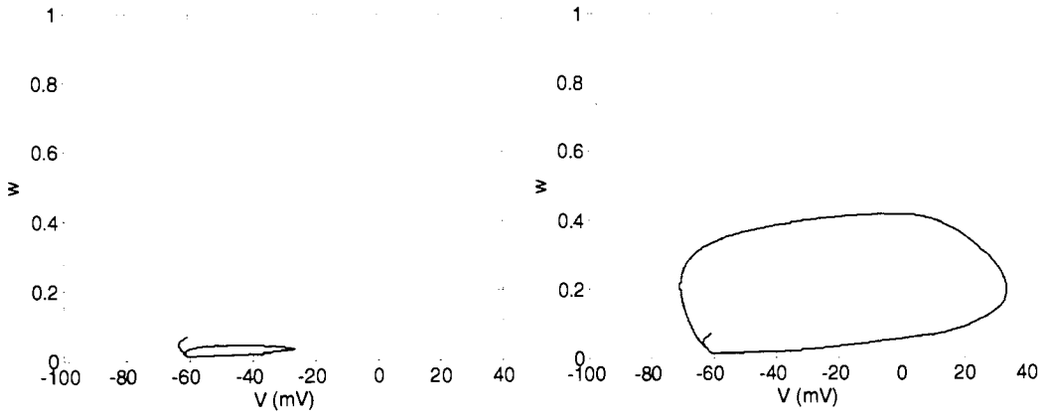

Figure 1.11. Variables of ML model in the phase plane. In the left and right graph, the variables (V, w) are plotted for the left and right graphs in Figure 1.10, respectively.

Consider another situation where a constant current is injected. The graphs of the numerical solutions for Eqs. 20 with different values of I_{app} are shown in Figure 1.12. As I_{app} increases above a certain value, V starts oscillating periodically. This is a bifurcation, where, due to the change in the value of I_{app}, the behavior of the solution of the differential equations qualitatively changes (see 1.5.3). When I_{app} is above the threshold, the solution of Eqs. 20 converges to a closed orbit in the phase plane. This is called a stable limit cycle (see 1.5.2). A detailed analysis shows that this bifurcation is a subcritical Hopf bifurcation (see 1.5.3.2). For more detailed analysis of this system, the reader is referred to [41, 43].

The changes in the ionic currents during the periodic spiking for $I_{app} = 150$ are shown in Figure 1.13. The total current through the membrane is plotted on the middle panel (positive current is defined as inward current). One can see that there is inward current at the upstroke of an action potential while there is outward current at the downstroke of an action potential. The Ca^{2+} current (solid line, positive is defined as

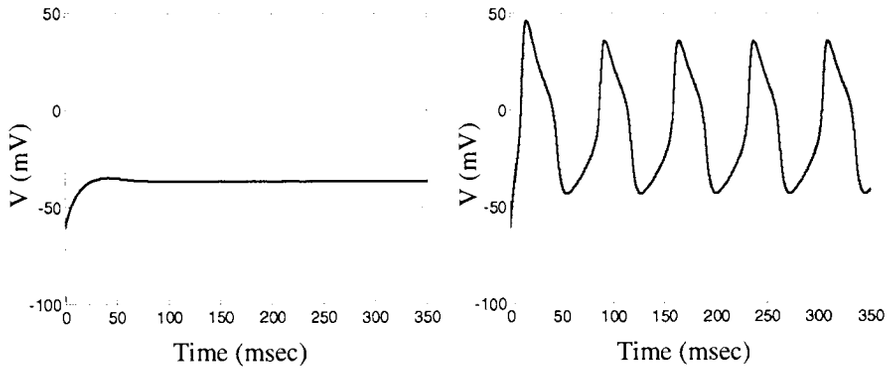

Figure 1.12. The time course of membrane potential responding to constant current with different values. *Left*: $I_{app} = 60$, *Right*: $I_{app} = 150$.

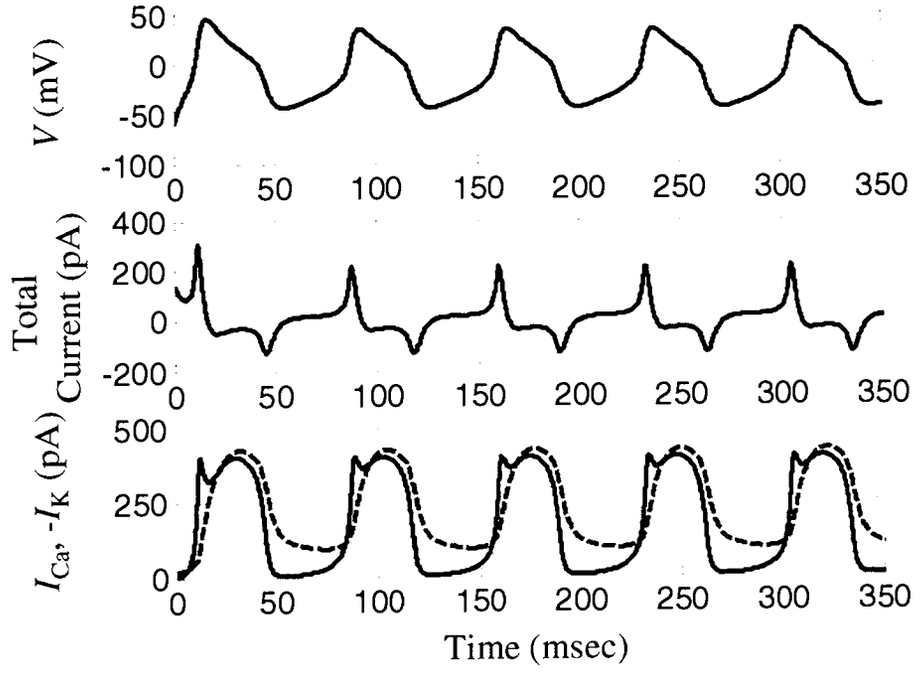

Figure 1.13. The time course of ionic currents. *Top*: membrane potential with $I_{app} = 150$ (identical to Figure 1.12 right). *Middle*: total ionic current through the membrane (positive is defined as inward current). *Bottom*: Ca^{2+} current (solid line) and K^+ current (dashed line) through the membrane.

inflow of Ca^{2+}) and K^+ current (dashed line, positive is defined as outflow of K^+ for presentation purposes) are plotted on the bottom panel. There is a slight time lag between inflow of Ca^{2+} and outflow of K^+, which is crucial to generation of an action potential. The upstroke of an action potential is mainly due to the flow of Ca^{2+} ions into the cell, while the decrease in the membrane potential at the last phase of an action potential is due to the flow of K^+ out of the cell.

In the case of the neural model, this description holds by replacing Ca^{2+} with Na^+: the upstroke of the action potential is due to the inflow of Na^+ ions, while the downstroke is caused by the outflow of K^+ ions.

1.5. NONLINEAR DYNAMICS

In this subsection, background is provided on the aspects of nonlinear dynamics relevant to the problems discussed in the dissertation. For more comprehensive treatment, the reader is referred to [44-46].

The focus of this subsection is a set of ordinary equations:

$$\begin{aligned} \dot{x}_1 &= f_1(x_1,\ldots,x_n) \\ &\vdots \\ \dot{x}_n &= f_n(x_1,\ldots,x_n) \end{aligned} \tag{22}$$

where $\dot{x}_i = dx_i / dt$. The space that consists of the n variables is called the *phase space* and n is called the dimension of the system. The solution of Eqs. 22 is a curve in the phase space for the system.

1.5.1. Linear Stability Analysis. In Eqs. 22, any $x^* = (x_1^*,\ldots,x_n^*)$ for which all the $\dot{x}_i$s are zero is called a fixed point. How the solution for Eqs. 22 behaves near fixed points can be studied by *linear stability analysis*.

1.5.1.1 One-dimension case. Assume that x^* is a fixed point for the equation $\dot{x} = f(x)$. Define $\eta(t) = x(t) - x^*$. Then

$$\begin{aligned}\dot{\eta} &= \dot{x} = f(x) = f(\eta + x^*) \\ &= f(x^*) + f'(x^*)\eta + O(\eta^2) \\ &= f'(x^*)\eta + O(\eta^2).\end{aligned} \tag{23}$$

For the last equality, $f(x^*) = 0$ is used. Ignoring the quadratic and higher order terms in η,

$$\dot{\eta} = f'(x^*)\eta \tag{24}$$

which is linear in η. Therefore, if $f'(x^*) > 0$, η grows exponentially, while, if $f'(x^*) < 0$, η decays exponentially to zero[3]. A fixed point of the former kind is called a stable fixed point while the latter is called an unstable fixed point. If $f'(x^*) = 0$, taking a higher order term in η will be necessary. It is also possible to determine the linear stability geometrically as illustrated in the example below.

Example. Consider

$$\dot{x} = x^2 + c, \quad c < 0. \tag{25}$$

There are two fixed points: $x^* = \pm\sqrt{-c}$. At $x^* = -\sqrt{-c}$, $f'(x^*) < 0$ and, therefore, the point is stable, while the other point is unstable. The graph of $f(x)$ gives an intuitive picture about the stability of the fixed points (Figure 1.14). The solution starting in the neighborhood of the left fixed point approaches the fixed point, while that of the right fixed point goes away from the fixed point.

1.5.1.2 Two-dimensional case. For *n*=2, the treatment is slightly more complicated than the one-dimensional case. Consider the set of equations

$$\begin{aligned}\dot{x}_1 &= f_1(x_1, x_2) \\ \dot{x}_2 &= f_2(x_1, x_2).\end{aligned} \tag{26}$$

---

[3] The solution of $dx/dt=cx$ is $x(t)=x(0)\exp(ct)$.

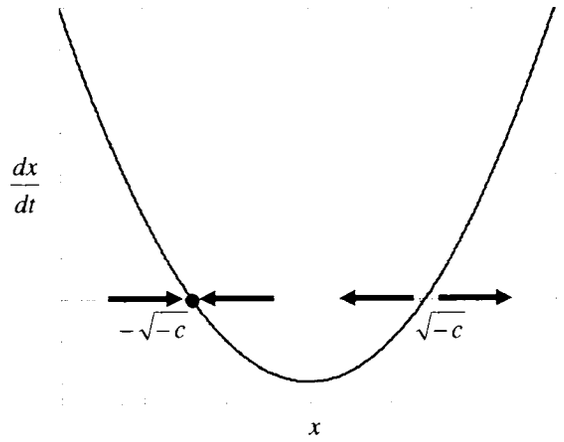

Figure 1.14. The time derivative of x as a function of x for the system in Eq. 25.

Let (x_1^*, x_2^*) be a fixed point and $u_1 = x_1 - x_1^*$ and $u_2 = x_2 - x_2^*$. Then the equation for u_1 is:

$$\begin{aligned} \dot{u}_1 &= \dot{x}_1 \\ &= f_1(x_1^* + u1, x_2^* + u_2) \\ &= f_1(x_1^*, x_2^*) + \frac{\partial f_1}{\partial x_1} u_1 + \frac{\partial f_1}{\partial x_2} u_2 + O(u_1, u_2, u_1 u_2) \\ &= \frac{\partial f_1}{\partial x_1} u_1 + \frac{\partial f_1}{\partial x_2} u_2 + O(u_1, u_2, u_1 u_2) \end{aligned} \tag{27}$$

For the third equality, the Taylor series expansion was used and, for the last equality, $f_1(x_1^*, x_2^*) = 0$ was used. The equation for u_2 can be obtained in a similar fashion and, by ignoring the quadratic or higher order terms in u_1 and u_2, the equations for u_1 and u_2 can be summarized in matrix form as follows:

$$\begin{pmatrix} \dot{u}_1 \\ \dot{u}_2 \end{pmatrix} = \begin{pmatrix} \partial f_1 / \partial x_1 & \partial f_1 / \partial x_2 \\ \partial f_2 / \partial x_1 & \partial f_2 / \partial x_2 \end{pmatrix} \begin{pmatrix} u_1 \\ u_2 \end{pmatrix}. \tag{28}$$

This is a two-dimensional linear equation. Note that the matrix in Eq. 28 is the Jacobian matrix of the vector-valued function $F(x_1, x_2) = (f_1(x_1, x_2), f_2(x_1, x_2))$ and the solution can be obtained by finding eigenvalues and eigenvectors of the Jacobian matrix. The stability of the fixed point can be classified based on the spectrum of eigenvalues of the Jacobian matrix, which is briefly summarized here. The real part of the eigenvalues determines stability. If the real part of both eigenvalues is negative (positive), the fixed point is stable (unstable). If the eigenvalues are complex numbers (purely imaginary), the fixed point is a spiral (center). See [44] for more detail.

1.5.2. Stable Limit Cycle. A limit cycle is a closed trajectory in the phase space. A limit cycle is called stable if all the trajectories in the neighborhood of the limit cycle approach the limit cycle as time goes to positive infinity. A stable limit cycle implies a sustained oscillation.

The set of equations below gives a simple example of a stable limit cycle [44].

$$\dot{r} = r(1 - r^2), \ \dot{\theta} = 1 \tag{29}$$

where $r \geq 0$. Since r and θ are not coupled, the dynamics of r and θ can be studied separately. The linear stability analysis for r shows that $r^* = 0$ is an unstable fixed point, while $r^* = 1$ is a stable fixed point. It is easy to see that θ increases linearly in time. Therefore, trajectories starting from all points except the origin approach the unit circle (Figure 1.15).

1.5.3. Bifurcation. A bifurcation can be said to be a qualitative change in the behavior of the solution of a system of differential equations due to changes of parameters in the system. This subsection discusses two types of bifurcation which are relevant to the subjects of this dissertation.

1.5.3.1 Saddle-node bifurcation. Consider the equation

$$\dot{x} = x^2 + c \tag{30}$$

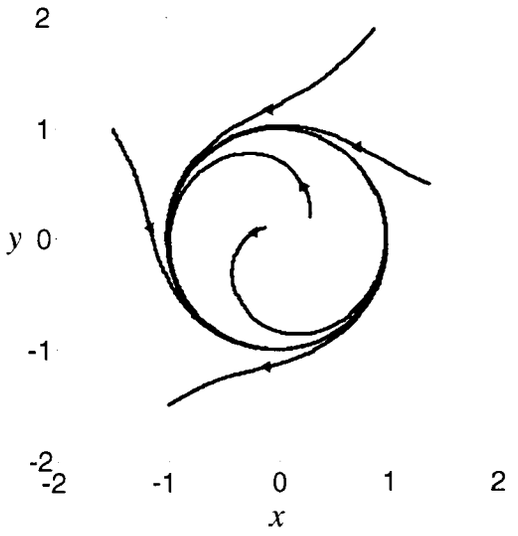

Figure 1.15. An example of a stable limit cycle.

where c is a parameter which can be any real number. When c is negative, as shown in the example in 1.5.1, there are two fixed points: one is stable and the other is unstable (Figure 1.14). As c is decreased down to zero, the two fixed points merge into one fixed point which is half-stable (Figure 1.16, left). When c is positive, there is no fixed point (Figure 1.16, right) and the solution with any initial value goes to positive infinity as time goes to positive infinity. The behavior of the solution for Eq. 30 is qualitatively different for $c>0$ and $c<0$. It is said that, in this example, a bifurcation occurred at $c=0$.

1.5.3.2 Hopf bifurcation. A Hopf bifurcation is characterized by the appearance of a limit cycle from a fixed point as a result of the change of a parameter in a system of differential equations. This bifurcation is mathematically described by the Hopf bifurcation theorem [45], which is not discussed here. Instead, two examples [44] of the Hopf bifurcation are discussed below. The first example is called a *supercritical Hopf bifurcation*. Consider the set of equations

$$\begin{aligned} \dot{r} &= \mu r - r^3 \\ \dot{\theta} &= \omega + br^2. \end{aligned} \tag{31}$$

For $\mu < 0$, the origin is the only fixed point, and is a stable spiral (see 1.5.1.2 for the classification of fixed points). On the other hand, for $\mu > 0$, the origin becomes an unstable spiral surrounded by a stable limit cycle with radius $\sqrt{\mu}$.

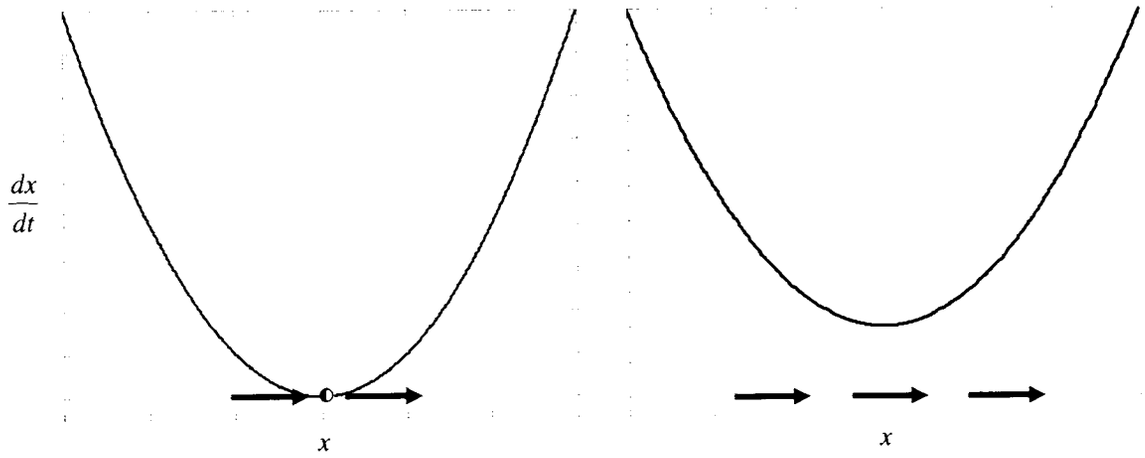

Figure 1.16. An example of saddle-node bifurcation. Left: $c = 0$. Right: $c > 0$.

The second example shows another type of Hopf bifurcation, a *subcritical Hopf bifurcation*. Consider the system

$$\begin{aligned} \dot{r} &= \mu r + r^3 - r^5 \\ \dot{\theta} &= \omega + br^2. \end{aligned} \tag{32}$$

After some algebra and linear stability analysis, one can find interesting changes in behavior of this system as μ varies. For $\mu < -1/4$, the origin is a stable spiral. There is no attractor (i.e., a set of points to which points in the neighborhood are attracted, such as a stable fixed point or stable limit cycle) in this phase space. For $-1/4 < \mu < 0$, the stable spiral at the origin is surrounded by an unstable limit cycle. This unstable limit cycle is further surrounded by a stable limit cycle. As μ increases toward 0, the unstable limit

cycle shrinks and merges into the stable fixed point at the origin at $\mu = 0$. For $\mu > 0$, the origin becomes an unstable spiral. This fixed point is surrounded by a stable limit cycle.

As discussed in the next subsection, the subcritical Hopf bifurcation is one of the most common ways in which the periodic occurrence of action potentials initiates from a constant membrane potential as a response to an increased stimulus current in a neural model.

1.5.3.3 Bifurcations in neural dynamics. As described before, it is common to study how a neuron responds to constant stimulus current in both experiments (see 1.2.9.3) and neural models (see 1.4.6). What commonly happens is that the membrane potential shows periodic oscillations (i.e., repetitive action potentials) when the stimulus current is above some threshold, while the membrane potential stays constant for stimulus current below the threshold. In a neural model, this is a bifurcation, where the constant membrane potential below the threshold corresponds to a stable fixed point, while periodic oscillations correspond to a stable limit cycle.

There are two common ways by which a stable limit cycle can emerge through bifurcation in a neural model: saddle-node bifurcation and Hopf bifurcation. Although the detail is not discussed here, one important implication for neuroscience of the differences between two bifurcations is discussed. For more detailed discussions, the reader is referred to [41, 43].

In the emergence of a limit cycle from a fixed point through the Hopf bifurcation, the Hopf bifurcation theorem says that the frequency of the limit cycle near a bifurcation point is the imaginary part of the eigenvalue of the Jacobian at the fixed point. This can be translated to a neural model in the following way: as the stimulus current is increased, the frequency of periodic oscillations at the point of transition from a constant membrane potential has nonzero minimum. On the other hand, in the case of the emergence of a limit cycle though the saddle-node bifurcation, the frequency of periodic oscillations near the bifurcation point can be arbitrarily small, which is often called the emergence of oscillations with zero frequency. See [41, 43] for such examples. In a real neuron, the emergence of periodic oscillations with both zero and non-zero frequency is observed, which presumably can be explained by the dynamical difference above.

1.5.4. Phase Reduction. This subsection is devoted to the description of a method for reducing the dimension of a system with a stable limit cycle to a one-dimensional variable, "phase". For a more complete discussion the reader is referred to [46, 47]. Throughout this subsection, the following n-dimensional differential equation

$$\dot{x} = F(x) \tag{33}$$

is considered and it is assumed that this differential equation has a stable limit cycle with period T as a solution.

1.5.4.1 Phase function and isochrons. Since a stable limit cycle is a closed periodic orbit in the phase space, it intuitively makes sense to define the phase of the oscillator. Let x_0 be a point on the limit cycle and define the phase function θ on the limit cycle such that $\theta(x_0(t)) = t \bmod T$. This is just a parameterization of the limit cycle with respect to its period.

It is possible to extend the phase function to some neighborhood of the limit cycle. Let y_0 be a point in the neighborhood of the limit cycle such that $y_0(t)$ goes to $x_0(t)$ as t goes to infinity. Then, the phase of y_0 can be defined as $\theta(y_0) = \theta(x_0)$. This extends the phase function to some neighborhood in the basin of attraction of the limit cycle.

The level sets of θ (i.e., sets consisting of points in some neighborhood of the limit cycle such that the phase of the points in each set is the same) are called *isochrons*. The existence of isochrons was proved in [48]. Since the component function of the gradient of the phase function ($=\partial\theta/\partial x_i$) gives the change in phase due to a small perturbation in the respective position coordinates, the graphs of those functions are often referred to as *phase response curves*, which play an important role for the study of weak perturbations to a limit cycle oscillator, as explained in the next subsection.

As an example, the Stuart-Landau oscillator is discussed. The set of equations for the oscillator is given by

$$\begin{aligned} \dot{x} &= x - c_0 y - (x^2 + y^2)(x - c_2 y), \\ \dot{y} &= c_0 x + y - (x^2 + y^2)(c_2 x + y). \end{aligned} \tag{34}$$

By defining the coordinate (r,θ) as [49]

$$\begin{aligned} x &= r\cos(\theta + c_2 \ln r) \\ y &= r\sin(\theta + c_2 \ln r), \end{aligned} \tag{35}$$

the solution with the initial point (r_0,θ_0) with $r_0 \neq 0$ is represented by

$$\begin{aligned} r(t) &= \left(1 + \frac{1-r_0^2}{r_0^2} e^{-2t}\right)^{-\frac{1}{2}} \\ \theta(t) &= \theta_0 + (c_0 - c_2)t. \end{aligned} \tag{36}$$

This shows that there is a stable limit (a circle with r=1) and that θ is the phase function since it increases linearly in time. For a given point (x,y), the phase of the point can be obtained by solving Eq. 35. Isochrons for the Stuart-Landau oscillator with different parameters are plotted in Figure 1.17.

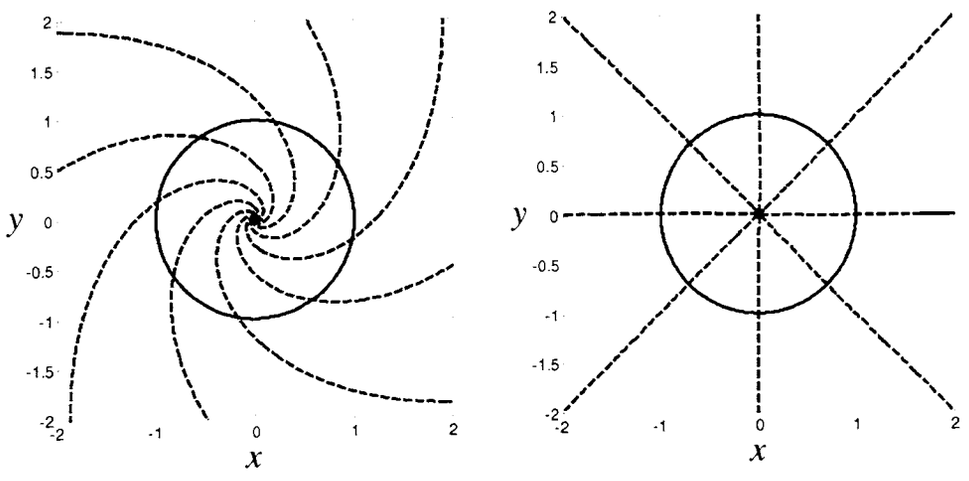

Figure 1.17. Isochrons for the Stuart-Landau oscillator for different parameter sets. The unit circles in both graphs represent the stable limit cycle solution for Eq. 34. Isochrons are plotted with dashed lines with time interval of $\pi/8$. *Left*: c_0=2, c_2=1 *Right*: c_0=1, c_2=0.

1.5.4.2 First order phase reduction. It is easy to see why the derivatives of θ are needed when studying weak perturbations of a stable oscillator described by $\dot{x} = F(x)$. Let such a perturbation be given by the new equation

$$\dot{x} = F(x) + \varepsilon G(x,t), \tag{37}$$

where ε is a small positive number. Then, using the chain rule,

$$\begin{aligned} \frac{d}{dt}\theta(x(t)) &= \nabla\theta(x(t)) \cdot \dot{x} \\ &= \nabla\theta(x(t)) \cdot F(x) + \nabla\theta(x(t)) \cdot \varepsilon G(x,t) \\ &= 1 + \nabla\theta(x(t)) \cdot \varepsilon G(x,t) \end{aligned} \tag{38}$$

where $\nabla\theta$ is the gradient of the phase function. Writing $Q_t^{(1)} = \nabla\theta(x_0(t))$, where $x_0(t)$ is the point on the limit cycle on the same isochron as $x(t)$, then

$$\frac{d\theta}{dt} = 1 + \varepsilon Q_t^{(1)} \cdot G(x,t) + \varepsilon O\left(\left|x(t) - x_0(t)\right|\right). \tag{39}$$

One then proceeds by discarding the term $\varepsilon O\left(\left|x(t) - x_0(t)\right|\right)$ and analyzing the resulting system. Thus, implementing the phase reduction method in order 1 in $|x(t)\text{-}x_0(t)|$ requires finding the gradient of the phase function along the limit cycle of the unperturbed oscillator, denoted by $Q_t^{(1)}$ in the last equation.

One practical method for obtaining the gradient of θ is by solving the equation:

$$\dot{Q}_t^{(1)} + DF^*(x_0(t))Q_t^{(1)} = 0 \tag{40}$$

where the dot indicates the time derivative and $DF^*(x_0(t))$ is the transpose of the Jacobian matrix of F evaluated along the limit cycle. This procedure was suggested by Malkin [50] and later by others independently [51, 52]. The reader is referred to [50],

Chapter 9, for more details of Malkin's theorem and [46], Chapter 10, for a historical note on phase reduction. One can find $Q_t^{(1)}$ by numerically integrating the equation backwards in time for any initial condition satisfying $Q_0^{(1)} \cdot F(x_0(0)) = 1$ (note that $d\theta/dt = 1$ by the definition of the phase function and that $d\theta/dt = Q_t^{(1)} \cdot F(x_0(t))$ by the chain rule) over an interval of time long enough to allow the solution to stabilize to a periodic orbit [53].

1.5.4.3 Two oscillator problem. Phase reduction has been applied to a synchronization problem of coupled oscillators. This method is used in Section 4. Consider a pair of weakly coupled identical oscillators indexed by *i* and *j*:

$$dX_i(t)/dt = F(X_i) + \varepsilon G(X_i, X_j) \tag{41}$$

where the coupling between the two oscillators is given by the function *G*. Each oscillator can be reduced to the following phase equation:

$$\dot{\theta}_i = 1 + Q_i^{(1)}(\theta_i) \cdot \varepsilon G(x_0(\theta_i), x_0(\theta_j)), \tag{42}$$

where $x_0(\theta)$ is a point on the limit cycle whose phase is θ. Then, using averaging [50], the equation can be written as

$$\frac{d\theta_i}{dt} = 1 + H(\theta_j - \theta_i), \tag{43}$$

where the function H is given by

$$H(\theta_j - \theta_i) = \frac{1}{T}\int_0^T Q^{(1)}(t)^* G(x_0(t), x_0(t + \theta_j - \theta_i))dt. \tag{44}$$

Let ϕ be the difference between the phases of the two oscillators ($\phi = \theta_j - \theta_i$). The dynamics of the phase difference between the two oscillators can be represented as

$$\frac{d\phi}{dt} = H(-\phi) - H(\phi). \tag{45}$$

Note that the dynamics of the phase difference between the two oscillators is described by a one-dimensional differential equation and that, therefore, linear stability analysis in one-dimension (1.5.1.1) can be applied. In short, a fixed phase difference is thus any value ϕ_0 for which $\frac{d\phi}{dt} = 0$. The slope of $\frac{d\phi}{dt} = 0$ at ϕ_0 gives the stability of the phase difference, with a negative slope corresponding to a stable, and a positive slope corresponding to an unstable, phase difference.

1.5.5. Phase Synchronization Analysis. This subsection is devoted to explaining the motivation for, and methodology of, a measure to characterize one type of synchronization, phase synchronization, which is used for the data analysis of the voltage-sensitive dye experiments discussed in Section 3. Synchronization is often evaluated with measures based on linear correlation such as cross correlation. However, the measure may not work for signals with certain properties. In the case where two signals are linearly correlated, linear correlation techniques such as cross correlation work perfectly. On the other hand, when the correlation of two signals is nonlinear, linear correlation techniques do not necessarily work even if the two signals are synchronized. Another situation where linear correlation techniques may not work is when the *amplitude* of signal is not correlated, while the *phases* of the signal are synchronized. Rosenblum et al. [54] have suggested an analysis technique, called phase synchronization analysis, to overcome such a difficulty.

In phase synchronization analysis, the phase of a signal is extracted. This can be done by the application of the Hilbert transform to the signal to obtain the instantaneous phase of the signal via the construction of analytic signal

$$\xi(t) = x(t) + ix_H(t) = A(t)e^{i\phi(t)} \tag{46}$$

where $x_H(t)$ is the Hilbert transform of the original signal $x(t)$:

$$x_H(t) = \frac{1}{\pi} P.V. \int_{-\infty}^{\infty} \frac{x(\tau)}{t-\tau} d\tau \tag{47}$$

where $P.V.$ means that the integral is considered as the Cauchy principal value. $\phi(t)$ is the instantaneous phase of $x(t)$ [55].

The phase difference between two signals is calculated as the difference between instantaneous phases from the two signals. To evaluate the degree of synchronization, a histogram for the phase difference is made within a time window. The synchronization index, which corresponds to the intensity of the first Fourier mode of the probability density of the phase difference, is calculated as

$$\gamma = \sqrt{\langle \cos \Delta\phi(t_i) \rangle^2 + \langle \sin \Delta\phi(t_i) \rangle^2} \tag{48}$$

where $\Delta\phi(t_i)$ is the phase difference at the i^{th} time point in a time window and $\langle\ \rangle$ represents the average over time points in the window [56]. Note that synchronization index ranges from 0 to 1 and that higher value indicates more synchrony. For example, $\gamma = 1$ if two signals are perfectly synchronized ($\Delta\phi$ is constant in time), while $\gamma = 0$ if two signals are not synchronized at all ($\Delta\phi$ is uniformly distributed).

1.5.6. Singular Perturbation. In this subsection, an approximation technique is explained for one class of the boundary value problem, which is relevant to Sections 1.7.7 and 5.5. To illustrate the idea, consider the following boundary value problem [57]:

$$\begin{aligned} &\varepsilon y'' + (1+\varepsilon) y' + y = 0, \ 0 < x < 1 \\ &y(0) = 0, \ y(1) = 1 \end{aligned} \tag{49}$$

where $0 < \varepsilon << 1$. Although the analytical solution can be obtained for this equation, consider obtaining an approximate solution. To do so, the first thing one could think of is a perturbation series. Assume that the solution has a perturbation series:

$$y(x) = y_0(x) + \varepsilon y_1(x) + \varepsilon^2 y_2(x) + \cdots . \tag{50}$$

By substituting Eq. 50 into Eq. 49 and equating to zero the coefficients of each power of ε, the zeroth-order term of ε satisfies the following boundary value problem:

$$\begin{aligned} &y_0' + y_0 = 0, \\ &y_0(0) = 0, \, y_0(1) = 1. \end{aligned} \tag{51}$$

This already causes a difficulty. The general solution of Eq. 51 is

$$y_o(x) = ce^{-x} . \tag{52}$$

To satisfy the boundary condition $y_0(0) = 0$, c has to be 0, which gives $y_0(x) = 0$. However, this solution does not satisfy the other boundary condition. On the other hand, applying $y_0(1) = 1$ to Eq. 52 gives $y_0(x) = e^{1-x}$, which does not satisfy the boundary condition at x=0. Therefore, the application of regular perturbation theory does not work for this problem. However, it can be still meaningful, as discussed below.

The cause of the problem is as follows. Eq. 51 can be obtained by dropping the terms multiplied by ε. By dropping the term $\varepsilon y''$, the problem becomes a first order problem rather than a second order one. This is only valid when y'' is sufficiently small. To understand the problem better, compare the analytical solution of Eq. 49 with the approximate solution of Eq. 52 which satisfies the boundary condition $y_0(1) = 1$ (i.e., $y_0(x) = e^{1-x}$). The analytical solution of Eq. 49 is

$$y(x) = \frac{1}{e^{-1} - e^{-1/\varepsilon}} (e^{-x} - e^{-x/\varepsilon}) . \tag{53}$$

The two functions are plotted in Figure 1.18. One can see that there are two regions: the one close to $x = 0$ where the analytical solution changes very rapidly and the other where the approximate solution matches well with the analytical solution. The former region is

called the *boundary layer* while the latter is called the *outer region.* By calculating the second derivative of $y(x)$ using Eq. 53, one can show that, in the boundary region, the second derivative has an order of ε^{-2} and, therefore, the term $\varepsilon y''$ cannot be neglected. On the other hand, in the outer region, the term $\varepsilon y''$ is small compared to the other terms and can be safely neglected. Therefore, the regular perturbation works in the outer region.

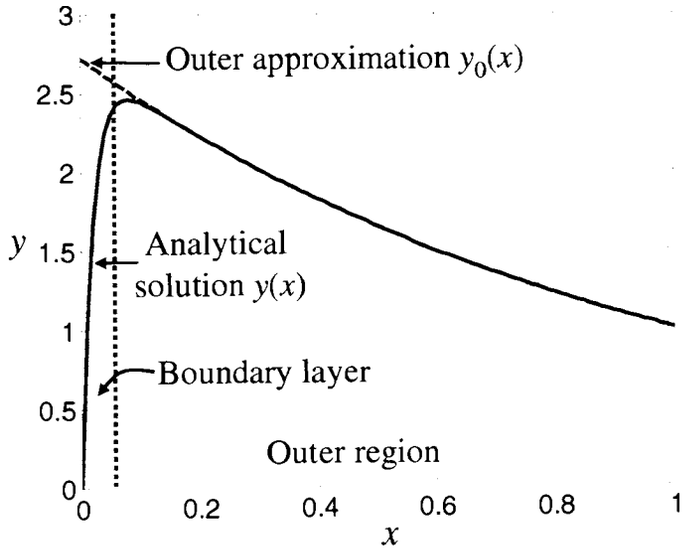

Figure 1.18. A comparison between the analytical and outer approximate solution for Eq. 49. The solid and dashed lines represent the analytical and outer approximate solution, respectively.

The discussion above indicates that an approximate solution of Eq. 49 has to be found separately in the boundary layer and outer region. To find an approximate solution in the boundary layer, so-called boundary layer analysis can be used. To concatenate continuously a boundary layer solution with an outer region solution, matching has to be done. However, in this dissertation, as only the determination of the outer region solution is required, those issues are not discussed. The interested reader should refer to [57].

1.6. SOME CONCEPTS FROM PROBABILITY THEORY AND STOCHASTIC PROCESSES

In this subsection, some notions from elementary probability (i.e., non-measure theoretic probability theory) relevant to this dissertation are provided in an informal setting. For more precise and comprehensive treatment, the reader is referred to [41].

1.6.1. Probability. Suppose that there is some experiment one would like to model. A sample space S is a set that consists of all the possible outcomes of the experiment. A point s in S corresponds to one possible outcome of the experiment. An event A is a subset of S, to which a probability is assigned. Events can be combined using the set operations. For example, $A \cup B$ is the event that occurs if and only if A occurs or B occurs (or both occur). $A \cap B$ is the event that occurs if and only if A occurs and B occurs, and so on.

Let C be a collection of all the subsets of S (i.e., a collection of all the possible events) and P be a real-valued function on C. Then P is called a *probability function* when the following axioms hold

1) $P(A) \geq 0$ for any event A

2) $P(S) = 1$

3) For any sequence of mutually disjoint events (i.e., $\{A_j\}_{j=1}^{\infty}$ such that

$A_i \cap A_j = \phi$ when $i \neq j$), $P(\bigcup_{i=1}^{\infty} A_i) = \sum_{i=1}^{\infty} P(A_i)$

Then, $P(A)$ is called the *probability* of the event A.

1.6.2. Conditional Probability. Let A and B be two events such that $P(A) > 0$. Then the conditional probability of B given A, denoted by $P(B \mid A)$, is defined as

$$P(B \mid A) = \frac{P(B \cap A)}{P(A)}. \tag{54}$$

To give a specific example, assume that there are two coins, each of which shows either a head or tail with equal probability (=1/2) and the outcome of one of the coins does not affect that of the other. Let A be the event where the first coin shows a head and B be the

event where the second coin shows a head. Then, the conditional probability that both coins show a head given that the first shows a head can be denoted as $P(A \cap B \mid A)$:

$$\begin{aligned} P(A \cap B \mid A) &= P((A \cap B) \cap A) / P(A) \\ &= P(A \cap B) / P(A) \\ &= (1/4)/(1/2) \\ &= 1/2. \end{aligned} \tag{55}$$

1.6.3. Independence. Let A and B be two events. Then the two events are *independent* if and only if

$$P(A \cap B) = P(A)P(B). \tag{56}$$

In the example of two coins above, the independence of the events A and B is implicitly assumed by the statement of "the outcome of one of the coins does not affect that of the other".

1.6.4. Random Variables, Distribution, and Density. A *random variable* X is a function from S into the set of real numbers such that, for $-\infty < x < \infty$, the set $\{s : X(s) \leq x\}$ is an event in S. The *distribution function* F of a random variable X is the function

$$F(x) = P(X \leq x), -\infty < x < \infty. \tag{57}$$

It is not hard to see that

$$\begin{aligned} &P(a < X \leq b) = F(b) - F(a), \ a \leq b \\ &F(-\infty) = 0, F(+\infty) = 1. \end{aligned} \tag{58}$$

Assuming $F(x)$ is differentiable, the *probability density function* $p(x)$ may be defined as

$$p(x) = \frac{dF(x)}{dx}. \tag{59}$$

It follows that

$$\begin{aligned} &\int_{-\infty}^{\infty} p(x)dx = 1 \\ &P(a < X \le b) = \int_{a}^{b} p(x)dx. \end{aligned} \tag{60}$$

Note that, for an infinitesimal number Δx, $p(x)\Delta x$ gives the probability that X is in the interval $(x, x+\Delta x]$, i.e.,

$$P(x < X \le x + \Delta x) = p(x)\Delta x. \tag{61}$$

1.6.5. Expected Value, Variance, Moments. The expected value of a random variable X, denoted by $E[X]$ or $\langle X \rangle$, is given by

$$E[X] = \int_{-\infty}^{\infty} xp(x)dx. \tag{62}$$

The variance of X, denoted by $Var(X)$, is defined as

$$\begin{aligned} Var(X) &= E\left[(X - E[X])^2\right] \\ &= E[X^2] - E[X]^2. \end{aligned} \tag{63}$$

The n^{th} order moment of X is defined as

$$E\left[X^n\right] = \int_{-\infty}^{\infty} x^n p(x)dx. \tag{64}$$

1.6.6. Mean Square Limit. Let $\{X_n\}$ be a sequence of random variables. X_n is said to converge to X in the mean square sense if

$$\lim_{n\to\infty} E[(X_n - X)^2] = 0. \tag{65}$$

1.6.7. Moment Generating Function. The moment generating function $u(s)$ of a random variable X is given by the Laplace transform of the probability density function:

$$u(s) = E[e^{-sX}] = \int_{-\infty}^{\infty} e^{-sx} p(x)dx \tag{66}$$

where $p(x)$ is the probability density for X. Then, the n^{th} moment of X (Eq. 64) can be calculated as

$$E[X^n] = (-1)^n \left.\frac{\partial^n u}{\partial s^n}\right|_{s=0}. \tag{67}$$

1.6.8. Stochastic Processes. For an element s in the sample space S, define a function $X(t,s)$ where $t \in T \subset \Re$. Then, the set

$$\{X(t,s), t \in T\} \tag{68}$$

is called a *stochastic process* [58]. Note that, for any particular value of t, the function $X(t,s)$ is a random variable. It is often unnecessary to write the argument s of the function $X(t,s)$. Then the stochastic process can be written by

$$\{X(t), t \in T\}. \tag{69}$$

or more simply, $X(t)$.

The joint probability density of the stochastic process $X(t)$ is defined as follows:

$$p(x_1,t_1;\ldots;x_k,t_k) = P(X(t_1) = x_1,\ldots,X(t_k) = x_k)\,. \tag{70}$$

Similarly, the conditional probability (see 1.6.2) of the stochastic process $X(t)$ can be defined as

$$\begin{aligned} &p(x_1,t_1;\ldots;x_k,t_k \mid x_{k+1},t_{k+1};\ldots;x_{k+N},t_{k+N}) \\ &\quad = p(x_1,t_1;\ldots;x_{k+N},t_{k+N}) / p(x_{k+1},t_{k+1};\ldots;x_{k+N},t_{k+N}). \end{aligned} \tag{71}$$

1.6.9. Markov Process. The Markov property is the property that, given the present state, the states in the past do not have any influence on the future. A Markov process is a stochastic process which satisfies the Markov property. Using the conditional probability of a stochastic process $X(t)$, the Markov property can be written as

$$p(x_1,t_1;\ldots;x_k,t_k \mid x_{k+1},t_{k+1};\ldots;x_{k+N},t_{k+N}) = p(x_1,t_1;\ldots;x_k,t_k \mid x_{k+1},t_{k+1}) \tag{72}$$

provided

$$t_1 \geq t_2 \geq \ldots \geq t_{k+N}\,. \tag{73}$$

1.7. STOCHASTIC DIFFERENTIAL EQUATIONS

In Sections 4 and 5, stochastic differential equations (SDE), which are also known as Langevin equations, are used. In particular, an understanding of stochastic differential equations is crucial for the material presented in Section 5 below. A stochastic differential equation has the form of

$$\frac{dx}{dt} = a(x) + b(x)\xi(t) \tag{74}$$

where $\xi(t)$ is a Gaussian white noise term with mean zero and covariance is given by

$$\langle \xi(t)\xi(t') \rangle = \delta(t-t') \tag{75}$$

which has the pathology of having infinite variance. It turns out that the white noise is, in some sense, the derivative of the Wiener process, which is a mathematical model of Brownian motion, although the Wiener process is nowhere differentiable. This subsection provides some background about how Eq. 74 should be interpreted. Two common interpretations are called Ito and Stratonovich integrals (see 1.7.3). The scope of the discussion here is limited to one-dimensional SDE. For more comprehensive treatment, the reader should refer to, for example, [59, 60].

1.7.1. Wiener Process. Brownian motion is the highly irregular motion of particles in a liquid due to bombardment by smaller molecules of the liquid. Let $W(t)$ be the location of a particle at time t. The Wiener process is a process $W(t)$ that satisfies the following properties [61]:

(1) $W(0) = 0$

(2) $W(t) - W(s)$ has a Gaussian distribution with mean 0 and variance $t - s$.

(3) $W(t_2) - W(t_1)$, $W(t_3) - W(t_2)$, ..., $W(t_n) - W(t_{n-1})$ are independent for

$t_1 \le t_2 \le \ldots \le t_{n-1} \le t_n$.

One realization of simulated Wiener process is shown in Figure 1.19. It can be shown that a Wiener process $W(t)$ is a continuous process but is nowhere differentiable.

1.7.2. White Noise. Although the Wiener process is nowhere differentiable, define the process $Y(t)$ [58]

$$Y(t) = \lim_{h \to 0} \frac{W(t+h) - W(t)}{h}. \tag{76}$$

Then, the mean and covariance of $Y(t)$ (interchanging the limit and the operation of taking expectation (see 1.6.5), which is integral, is assumed) are

$$\begin{aligned} E[Y(t)] &= \lim_{h \to 0} E\left[\frac{W(t+h) - W(t)}{h} \right] \\ &= \lim_{h \to 0} 0 = 0 \end{aligned} \tag{77}$$

and, by noting, when $t < s$, that $E[W(t)W(s)] = E[W(t)(W(s) - W(t)) + W^2(t)] = t$,

$$E[Y(t)Y(s)] = \lim_{h\to 0} E\left[\left(\frac{W(t+h)-W(t)}{h}\right)\left(\frac{W(s+h)-W(s)}{h}\right)\right] = \begin{cases} 0 & \text{if } t \neq s \\ \infty & \text{if } t = s \end{cases}, \tag{78}$$

which gives the required properties for Gaussian white noise. Therefore, although the Wiener process is nowhere differentiable, Gaussian white noise can be symbolically written as the time derivative of the Wiener process:

$$\xi(t) = dW(t)/dt. \tag{79}$$

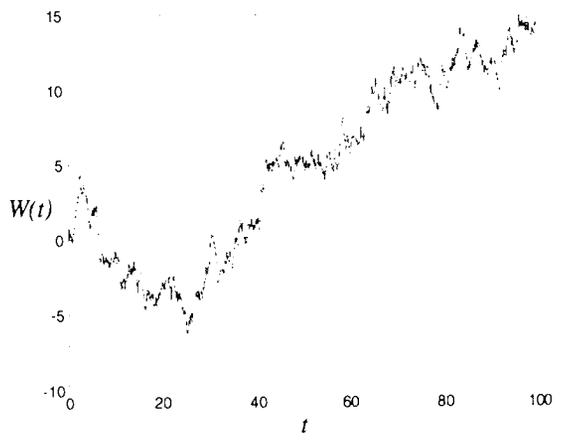

Figure 1.19. A realization of simulated Wiener process.

1.7.3. Stochastic Integrals: Ito and Stratonovich. Based on the discussion of white noise in the previous subsection, the integral of Eq. 74 can be symbolically written as follows:

$$\begin{aligned} x(t_1) - x(t_0) &= \int_{t_0}^{t_1} a(x(t))dt + \int_{t_0}^{t_1} b(x)\xi(t)dt \\ &= \int_{t_0}^{t_1} a(x(t))dt + \int_{t_0}^{t_1} b(x)dW(t), \end{aligned} \tag{80}$$

where Eq. 79 is used for the 2nd term in the 2nd line. Though written in integral form, one has to determine how the 2nd integral on the right hand side is to be interpreted.

First, consider the following form of the integral

$$\int_{t_0}^{t} G(t')dW(t') \tag{81}$$

where $G(t)$ is an arbitrary function of time and $W(t)$ is a Wiener process. Divide the interval $[t_0, t]$ into n subintervals with a partition of $[t_0, t]$ such that $t_0 \le t_1 \le \cdots \le t_{n-1} \le t$. Define intermediate points τ_i such that

$$t_{i-1} \le \tau_i \le t_i \tag{82}$$

The integral $\int_{t_0}^{t} G(t')dW(t')$ can be defined as the limit of

$$S_n = \sum_{i=1}^{n} G(\tau_i)\big(W(t_i) - W(t_{i-1})\big). \tag{83}$$

For an ordinary Rieman-Stieltjes integral, S_n converges to the same limit independent of choices of τ_i. However, for Eq. 83, due to the stochastic nature of the Wiener process, the limit of S_n depends on the choice of τ_i, which is fundamentally different from a deterministic integral. To see this, let

$$G(t) = W(t),\ \tau_i = \alpha t_i + (1-\alpha)t_{i-1}. \tag{84}$$

Then, using the properties of the Wiener process, one can show [60] that

$$\lim_{\substack{\max \{t_i - t_{i-1}\} \\ 1 \le i \le n}} S_n = \frac{1}{2}\left(W^2(t) - W^2(t_0)\right) + (\alpha - \frac{1}{2})(t - t_0) \tag{85}$$

where the convergence occurs in the mean square sense (see 1.6.6). Therefore, to uniquely define the integral, it is necessary to specify where intermediate points are chosen. Set $\alpha = 0$, i.e., define S_n as

$$S_n = \sum_{i=1}^{n} W(t_{i-1})\left(W(t_i) - W(t_{i-1})\right). \tag{86}$$

The limit of S_n is called the Ito integral. In this case, From Eq. 85,

$$\text{(Ito)} \int_{t_0}^{t} W(t')dW(t') = \frac{1}{2}\left(W^2(t) - W^2(t_0)\right) - \frac{1}{2}(t - t_0). \tag{87}$$

Note that there is a deviation from the formal application of standard calculus, which would give

$$\int_{t_0}^{t} W(t')dW(t') = \frac{1}{2}\left(W^2(t) - W^2(t_0)\right). \tag{88}$$

An alternative definition of a stochastic integral, which satisfies the ordinary integral rule, was suggested by Stratonovich:

$$S_n = \sum_{i=1}^{n} \frac{W(t_{i-1}) + W(t_i)}{2}\left(W(t_i) - W(t_{i-1})\right). \tag{89}$$

Here, the limit of S_n gives the same result as the ordinary calculus:

$$(\text{Strat}) \int_{t_0}^{t} W(t')dW(t') = \frac{1}{2}\left(W^2(t) - W^2(t_0)\right). \tag{90}$$

In general, the Stratonovich integral satisfies the same rule as the ordinary calculus. However, there is a price for the convenience, which will be discussed in 1.7.5.

In a similar fashion, one can define the stochastic integral for the 2nd term on the right hand side of Eq. 80. The Ito integral is defined as

$$(\text{Ito}) \int_{t_o}^{t_1} b(x)dW(t) = \lim \sum_{i=1}^{n} b(x_{i-1})(W(t_i) - W(t_{i-1})), \tag{91}$$

while the Stratonovich integral is defined as

$$(\text{Strat}) \int_{t_o}^{t_1} b(x)dW(t) = \lim \sum_{i=1}^{n} \frac{b(x_i) + b(x_{i-1})}{2}(W(t_i) - W(t_{i-1})) \tag{92}$$

where $x_i = x(t_i)$ and $x(t)$ is a solution of the SDE in Eq. 74. In general, these two integrals give different values. However, the two stochastic integrals can be connected with the following formula [59]:

$$(\text{Strat}) \int_{t_o}^{t_1} b(x)dW(t) = (\text{Ito}) \int_{t_o}^{t_1} b(x)dW(t) + \frac{1}{2}\int_{t_0}^{t_1} b(x(t'))\frac{\partial b(x(t'))}{\partial x}dt'. \tag{93}$$

This is equivalent to saying that the following Ito and Stratonovich SDEs give the same solution:

$$\begin{aligned}&\text{(Ito SDE) } dx = a(x)dt + b(x)dW(t)\\&\text{(Stratonovich SDE) } dx = \left(a(x) - \frac{1}{2}b(x)\frac{\partial b(x)}{\partial x}\right)dt + b(x)dW(t)\end{aligned} \tag{94}$$

or conversely,

$$\begin{aligned}&\text{(Stratonovich SDE) } dx = \alpha(x)dt + \beta(x)dW(t)\\&\text{(Ito SDE) } dx = \left(\alpha(x) + \frac{1}{2}\beta(x)\frac{\partial \beta(x)}{\partial x}\right)dt + \beta(x)dW(t).\end{aligned} \tag{95}$$

1.7.4. Change of Variables: Ito Formula. Let *x(t)* be a solution of the Ito stochastic integral:

$$dx = a(x)dt + b(x)dW(t) \tag{96}$$

and let *f(x(t))* be a function of *x(t)*. The question of interest is to obtain the differential equation for *f(x(t))*.

$$\begin{aligned}df(x(t) &= f(x(t) + dx(t)) - f(x(t))\\&= f'(x(t))dx + \frac{1}{2}f''(x(t))dx(t)^2 + \ldots\\&= f'(x(t))(a(x)dt + b(x)dW(t)) + \frac{1}{2}f''(x(t))(a(x)dt + b(x)dW(t))^2 + \ldots\\&= f'(x(t))(a(x)dt + b(x)dW(t)) + \frac{1}{2}f''(x(t))(dW(t))^2 + \ldots\end{aligned} \tag{97}$$

Here is the most crucial part. One can show

$$\int_0 G(x(t'))dW^2(t') = \int_0 G(x(t'))dt' \tag{98}$$

where the stochastic integral on the left hand side is interpreted in the Ito sense. This implies that one can symbolically write

$$dW^2(t) = dt \tag{99}$$

and one can consider that dW is of the order of $dt^{1/2}$. Therefore, it turns out that all the neglected terms in the last line on Eq. 97 are of higher order than dt, and one can obtain

$$df(x(t)) = \left[f'(x(t))a(x) + \frac{1}{2}b(x(t))^2 f''(x(t)) \right] dt + b(x) f'(x(t)) dW(t). \tag{100}$$

This is known as the Ito formula. Note the term with the 2nd derivative of $f (=1/2b^2f'')$, which deviates from the ordinary calculus, as in the example of the Ito integral (Eq. 87). Thus, changing variables in the Ito SDE does not follow ordinary calculus unless $f''(x) = 0$.

On the other hand, with the Stratonovich interpretation, the change of variable formula follows the ordinary calculus rule. In other words,

$$df(x(t)) = f'(x(t))a(x)dt + b(x) f'(x(t)) dW(t). \tag{101}$$

1.7.5. Ito or Stratonovich. The discussions in 1.7.3 and 1.7.4 might lead one to conclude that the Stratonovich SDE is favorable to the Ito SDE, since Stratonovich follows the same rule as ordinary calculus. However, there is an advantage to the Ito SDE as well. As explained in the following two subsections, one of the major advantages, which is critical in Section 5, is that the Ito SDE is consistent with both forward and backward Fokker-Planck equations and, therefore, is also consistent with the first passage time problem. Using Ito's formula, one can show that the stochastic process that satisfies the Fokker-Plank equation is equivalent to the Ito SDE [59].

1.7.6. Forward and Backward Fokker-Planck Equations. It is known that one can obtain deterministic partial differential equations (PDE) for the conditional probability for a stochastic process described by an Ito SDE. One of the examples of this correspondence between the partial differential equation and the SDE is the diffusion equation and Brownian motion, as shown in an example below.

One type of such PDE is called the forward Kolmogorov equation, which is also known as the (forward) Fokker-Planck equation, and can be derived using the Ito formula (see 1.7.4). Let $x(t)$ be a solution of the following Ito SDE

$$dx = a(x)dt + b(x)dW(t) \tag{102}$$

and suppose that $x(t)$ has a conditional probability density $p(x,t|x_0, t_0)$ (see 1.6.8). Let f be an arbitrary function. Then, using Ito's formula, the time development of $f(x(t))$ satisfies

$$df = \left[f'(x(t))a(x) + \frac{1}{2}b(x(t))^2 f''(x(t)) \right]dt + b(x)f'(x(t))dW(t) \tag{103}$$

or, equivalently, one can write

$$\frac{df}{dt} = f'(x(t))a(x) + \frac{1}{2}b(x(t))^2 f''(x(t)) + b(x)f'(x(t))\xi(t) \tag{104}$$

where $\xi(t)$ is a Gaussian white noise term with mean zero and covariance $\langle \xi(t)\xi(t') \rangle = \delta(t-t')$. Take the expected value of both sides above to obtain

$$\begin{aligned} \left\langle \frac{df(x(t))}{dt} \right\rangle &= \frac{d}{dt}\langle f(x(t)) \rangle \\ &= \left\langle f'(x)a(x) + \frac{1}{2}b(x)^2 f''(x) + b(x)f'(x)\xi(t) \right\rangle \\ &= \left\langle f'(x(t))a(x) + \frac{1}{2}b(x(t))^2 f''(x(t)) \right\rangle \\ &= \int_{-\infty}^{\infty} \left(f'(x)a(x) + \frac{1}{2}b(x)^2 f''(x) \right) p(x,t \mid x_0,t_0)dx \end{aligned} \tag{105}$$

Note that, for the third equality above, the fact that

$$\langle b(x)f'(x)\xi(t)\rangle = 0 \tag{106}$$

is used and, for the last equality, the fact is used that, for a given function g, the expected value of $g(x(t))$ can be expressed as

$$\langle g(x(t))\rangle = \int_{-\infty}^{\infty} g(x)p(x,t \mid x_0,t_0)dx \tag{107}$$

.

On the other hand, using the conditional probability density, $d/dt\langle f(x)\rangle$ can be also expressed as

$$\frac{d}{dt}\langle f(x(t))\rangle = \int_{-\infty}^{\infty} f(x)\frac{\partial}{\partial t}p(x,t \mid x_0,t_0)dx \tag{108}$$

Therefore, using integration by parts and making the assumption that $p(x)$ and dp/dx converge to zero faster than any other terms, the following equation can be obtained:

$$\int_{-\infty}^{\infty} f(x)\frac{\partial}{\partial t}p(x,t \mid x_0,t_0)dx = \int_{-\infty}^{\infty} f(x)\left(-\frac{\partial}{\partial x}(a(x)p(x,t \mid x_0,t_0)) + \frac{1}{2}b(x)^2\frac{\partial^2}{\partial x^2}(b(x)^2 p(x,t \mid x_0,t_0))\right)dx \tag{109}$$

Therefore, since f is arbitrary, the following PDE for a conditional probability can be obtained:

$$\frac{\partial}{\partial t}p(x,t \mid x_0,t_0) = -\frac{\partial}{\partial x}(a(x)p(x,t \mid x_0,t_0)) + \frac{1}{2}\frac{\partial^2}{\partial x^2}(b(x)^2 p(x,t \mid x_0,t_0)) \tag{110}$$

This is known as the forward Fokker-Planck equation [59].

As an example [58], consider a Wiener process

$$dx = \sigma dW \tag{111}$$

with the initial condition, $x(t_0)=x_0$, i.e.,

$$\lim_{t \downarrow t_0} p(x,t \mid x_0,t_0) = \delta(x - x_0). \tag{112}$$

Then, the corresponding forward equation is

$$\frac{\partial p}{\partial t} = \frac{1}{2}\frac{\partial^2}{\partial x^2}(\sigma^2 p) \tag{113}$$

which is known as the one-dimensional heat equation. The following equation satisfies the PDE above

$$p(x,t \mid x_0,t_0) = \frac{1}{\sqrt{2\pi\sigma^2(t-t_0)}} \exp\left(-\frac{1}{2}\frac{(x-x_0)^2}{\sigma^2(t-t_0)}\right) \text{ for } t > t_0 \tag{114}$$

The solution also satisfies the initial condition Eq. 112.

One can obtain a similar equation, called the backward Fokker-Planck equation:

$$\frac{\partial}{\partial t_0} p(x,t \mid x_0,t_0) = -a(x)\frac{\partial}{\partial x_0} p(x,t \mid x_0,t_0) - \frac{1}{2} b(x)^2 \frac{\partial^2}{\partial x_0^2} p(x,t \mid x_0,t_0). \tag{115}$$

Note the difference between the forward and backward equations. In the forward equation, t_0 and x_0 are fixed, and the partial derivatives are with respect to t and x. In the backward equation, t and x are fixed, and the partial derivatives are with respect to t_0 and x_0. Although one can show that they are equivalent to each other, they are used for different purposes. The forward equation is often used to obtain the probability density of a variable at time t. One of the major applications of the backward equation is the study of first passage time, which is explained in the next subsection.

1.7.7. First Passage Time Problem. Consider the following 1-dimensional Ito SDE:

$$dx = a(x)dt + b(x)dW(t). \tag{116}$$

One can imagine that $x(t)$ represents the position of a particle at time t whose dynamics is described by Eq. 116. Assume that there are two absorbing barriers at A and B with $A<x(0)<B$. This means that, if the particle reaches A or B, the particle will be removed from the system. The problem of interest here is how long it takes for the particle to reach one of the two boundaries. This is called the first passage time problem. One can show that, using the backward equation (see 1.7.6), the mean first passage time starting from x at $t=0$, denoted as $T(x)$, for the system of Eq. 116 with the above absorbing boundaries obeys the following boundary value problem [59]:

$$a(x)\frac{dT(x)}{dx}+\frac{1}{2}b(x)\frac{d^2T(x)}{dx^2}=-1 \tag{117}$$

with the boundary conditions

$$T(A)=T(B)=0 \tag{118}$$

Similarly, the nth moment (1.6.5) of the first passage time, denoted as $T_n(x)$, satisfies

$$a(x)\frac{dT_n(x)}{dx}+\frac{1}{2}b(x)\frac{d^2T_n(x)}{dx^2}=nT_{n-1}(x) \tag{119}$$

which, in principle, allows one to determine all the moments of the first passage time by integrating Eq. 119 repeatedly.

As an example, the following SDE is considered

$$dx=adt+\sqrt{2\varepsilon}dW(t), \tag{120}$$

where ε is "small". Set two absorbing boundaries at -1 and 1. Then, the ODE for the mean first passage time is

$$\varepsilon \frac{d^2T(x)}{dx^2} + a\frac{dT(x)}{dx} = -1 \tag{121}$$

with the boundary conditions

$$T(-1) = T(1) = 0. \tag{122}$$

The analytical solution for the boundary problem above is

$$T(x) = -\frac{x}{a} - \frac{2}{a}\frac{e^{-ax/\varepsilon}}{(e^{a/\varepsilon} - e^{-a/\varepsilon})} + \frac{1}{a}\frac{e^{a/\varepsilon} + e^{-a/\varepsilon}}{e^{a/\varepsilon} - e^{-a/\varepsilon}} \tag{123}$$

On the other hand, the outer approximation in singular perturbation theory (see 1.5.6) gives

$$T_{outer}(x) = \frac{1-x}{a}. \tag{124}$$

Two solutions are plotted in Figure 1.20. Except for the region close to the left boundary, the outer approximation gives a good approximation to the analytical solution.

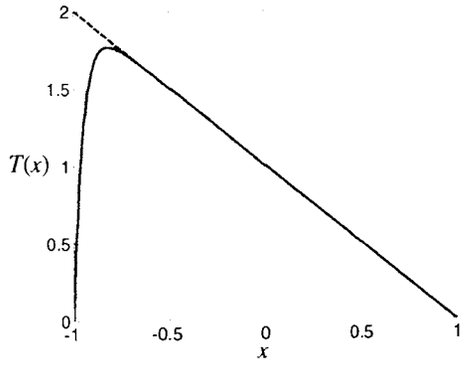

Figure 1.20. The analytical (solid line) and approximate (dashed line) solution for the mean first passage time.

2. ANALYZING SPIKE TRAINS WITH CIRCULAR STATISTICS

The study in this section is reprinted with permission from Daisuke Takeshita, John T. Gale, Erwin B. Montgomery, Jr., Sonya Bahar, and Frank Moss, American Journal of Physics, 77(5), pp 424-429, 2009.

2.1. OBJECTIVES

The analysis of neural signals has been of great interest in the fields of biophysics and neuroscience for more than six decades. The power spectrum is one of the most frequently used methods to detect periodicity from data, and thus is particularly useful for analyses of oscillatory and stochastic behavior of neural discharges [62, 63]. However, to understand the notion of the power spectrum, knowledge of Fourier analysis is required, which may be challenging for beginning undergraduate students who are taking introductory biophysics, as well as for students of neuro- or medical science who do not have experience with advanced mathematics. It will be shown that a statistical analysis technique called *circular statistics* (CS) can be applied to the important case of a time series of delta functions and yields the same information as the power spectrum, and thus might be a useful way of presenting the power spectrum concept at an introductory level.

It will be shown that CS can be applied to analyze time series of action potentials (see 1.2.5), or spike trains such as those recorded in a variety of experiments in neuroscience. Such experiments often yield data that present some combination of periodic and random behavior, sometimes called "harmonic noise" [64]. Contemporary examples range from extensive work on the electroreceptor in a variety of fish [65-70], through thermal receptors in mammals [71], to the noisy oscillations of hair bundles and hair cells in vertebrate auditory organs [72, 73] to name only a few. In the aforementioned examples the noisy oscillations are inherent to the dynamics of the particular organ, but in some cases the noise is deliberately added to a periodic stimulus, as in the example of noise-enhanced transmission of weak stimuli through ion channels in the cell membrane [74]. These examples indicate a range of applications where circular statistics might be usefully applied.

Circular statistics is suitable for analyzing data that are distributed on a circle, such as the directions that animals take after release from a central fixed point. Since not all animals will move in precisely the same direction, a statistical analysis is necessary. In seminal books, Batschelet [75] and Mardia [76] develop the theory in detail and describe classical applications. Modern examples include the use of CS to analyze the directional motions of single-celled algae [77], phase clustering of gamma oscillations in the brain [78] and the analysis of phase clustering in coupled oscillators [79].

An example of the type of motion to which CS can be applied is shown in Figure 2.1. Assume that one wants to know if there is a preferred direction in the behavior of a certain kind of bird when leaving its nest. To determine this, one first defines a circular boundary around the nest. If a bird crosses a point on the boundary, one puts a dot on the boundary at that point. If another bird crosses another point on the boundary, one also puts another dot at that point on the boundary, and so on. After many trials, the dots lying within bins of a small angular width can be counted. A histogram can thus be constructed on the circle (block bars in Figure 2.1) which immediately indicates the direction(s) preferred by the birds and their relative statistical strength(s). By applying this technique, one can obtain a simple, visual interpretation of the relative frequency of crossings in preferred directions, requiring only a basic knowledge of vectors and trigonometric functions. Below, it is shown how this simple construction can be used to analyze time series consisting of sequences of events that can be replaced with delta functions, and how it can reveal (sometimes hidden) periodicities within them. When the time series is a train of delta functions, it is shown that the technique reduces exactly to the power spectrum. The results of CS of simulated data sets are also compared with power spectra obtained using the discrete Fourier Transform (DFT). Finally, as a realistic example from neuroscience, it is shown how these techniques can be applied to neural spike trains from the crayfish photoreceptor.

2.2. FORMULATION

Formulations of the power spectrum and circular statistics of spike trains are discussed below. In both formulations, a spike train is considered as a sequence of events,

since it is generally accepted that the sequence of temporal occurrences of the spikes, rather than their size or shape, conveys information [38].

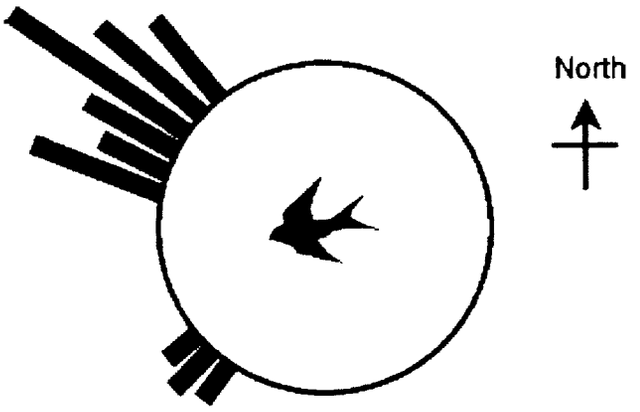

Figure 2.1. Circular statistics for detecting preferred direction.

2.2.1. Power Spectrum of a Sequence of Spikes. How to calculate the power spectrum of a signal is briefly explained below. For more rigorous and complete argument, see textbooks on signal processing such as [80] and [81]. Consider a collection (also called an ensemble) of signals $\{x_j(t)\}$. For each j, there exists a signal $x_j(t)$ and, for different j, $x_j(t)$ is not necessarily the same value. The statistical properties of the ensemble can be defined as the average over the ensemble (average over j). For example, the mean value of this process at time t, denoted as $E[x_j(t)]$, can be defined as the average of $x_j(t)$ over the ensemble:

$$E[x_j(t)] = \lim_{N\to\infty} \frac{1}{N} \sum_{j=1}^{N} x_j(t) \tag{125}$$

In reality, N has to be replaced by a finite number, and larger values of N give a better estimate of $E[x_j(t)]$. For a finite time interval $0 \le t \le L$, the Fourier transform of $x_j(t)$ is defined as

$$X(f,L,j) = \int_0^L x_j(t)\exp(-2\pi ift)dt\,. \tag{126}$$

The power spectrum of the signal is defined as

$$P(f) = \lim_{L\to\infty}\frac{1}{L}E[X(f,L,j)X^*(f,L,j)] \tag{127}$$

where $X^*(f, L, j)$ and $E[]$ represent the complex conjugate of $X(f, L, j)$ and ensemble average discussed above, respectively. Again, L has to be finite in reality. There are technical issues about how accurate the estimate would be for a given N and L, which are beyond the scope of this paper. An interested reader should see [80] and [81], and, for more neuroscience-oriented readers, see [82].

To consider the power spectrum for a spike train, assume a signal consisting of N spikes in the interval 0 to L, and let t_k be the time of the k^{th} spike. If the spikes are replaced by delta functions, the time series $x(t)$ becomes,

$$x(t) = \sum_{k=1}^{N}\delta(t-t_k) \tag{128}$$

where $\int_{-\infty}^{\infty}\delta(t-t_k)f(t)dt = f(t_k)$ for any well-behaved function [83]. Thus, the Fourier transform of the spike train is

$$\begin{aligned} X(f) &= \int\sum_{k=1}^{N}\delta(t-t_k)\exp(-2\pi ift)dt \\ &= \sum_{k=1}^{N}\exp(-2\pi ift_k) \\ &= \sum_{k=1}^{N}[\cos(2\pi ft_k) - i\sin(2\pi ft_k)] \end{aligned} \tag{129}$$

The power spectrum of the spike train is

$$
\begin{aligned}
P(f) &= \frac{1}{L_0}\langle X(f)X^*(f)\rangle \\
&= \frac{1}{L_0}\left\langle \left\{\sum_{k=1}^{N}[\cos(2\pi f t_k) - i\sin(2\pi f t_k)]\right\}\left\{\sum_{k=1}^{N}[\cos(2\pi f t_k) + i\sin(2\pi f t_k)]\right\}\right\rangle \\
&= \frac{1}{L_0}\left\langle \left[\sum_{k=1}^{N}\cos(2\pi f t_k)\right]^2 + \left[\sum_{k=1}^{N}\sin(2\pi f t_k)\right]^2\right\rangle
\end{aligned}
\tag{130}
$$

where L_0 and brackets < > denote the length of each periodogram and average over ensembles, respectively. To apply the Fourier transform to a recorded or generated spike train, the delta function will be "discretized" and the discrete Fourier transform (DFT) will be used to calculate the Fourier transform of the signal, which will be explained in 2.3.1.

2.2.2. Circular Statistics. In order to apply circular statistics to a data set, the time series data is first divided into time intervals T, which corresponds to the period of interest (Figure 2.2). Second, each segment is made into a circle with circumference T, and each spike is replaced by a unit vector on the circle. The resultant vector from all the circles is

$$
\vec{C}(T) = \sum_{k=1}^{N}\cos(2\pi t_k / T)\hat{x} + \sum_{k=1}^{N}\sin(2\pi t_k / T)\hat{y} \tag{131}
$$

where t_k is the time when the k^{th} spike occurred. A simple geometrical interpretation is the following. If spikes are totally periodic with a time interval T, one will obtain a large magnitude of the resultant vector because every unit vector occurs with the same phase, and hence at the same place on the circle (Figure 2.2A). On the other hand, random spike trains will produce a resultant vector of smaller magnitude, since the vectors are now distributed uniformly on circles and cancel each other when pointing in opposite directions (Figure 2.2B). Therefore, the magnitude of the resultant vector from circles with circumference T indicates the measure of periodicity of the signal at time interval T. By

finding the magnitude as a function of T, one can detect the degree of periodicity from the spike trains. The squared magnitude of the resultant vector is represented by

$$C(T) = \left[\left\{ \sum_{k=1}^{N} \cos(2\pi t_k / T) \right\}^2 + \left\{ \sum_{k=1}^{N} \sin(2\pi t_k / T) \right\}^2 \right] = \left[\left\{ \sum_{k=1}^{N} \cos(2\pi f t_k) \right\}^2 + \left\{ \sum_{k=1}^{N} \sin(2\pi f t_k) \right\}^2 \right] \quad (132)$$

where $f = 1/T$ is frequency of interest. Note that the magnitude of the resultant vector can also be considered a function of frequency. Therefore, by dividing by the length of each data set and taking the ensemble average, circular statistics is identical to the power spectrum of sequence of delta functions.

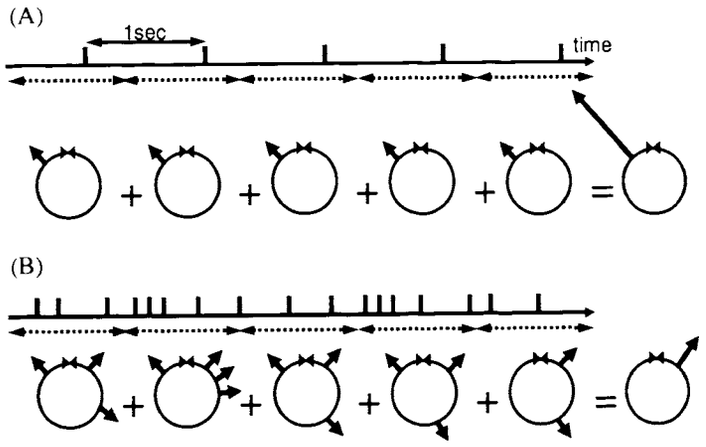

Figure 2.2. Schema of circular statistics. A: periodic and B: random spike trains. The time interval T is indicated by the dotted line segments.

To apply CS to a time series, the set of f has to be chosen. In this paper, in order to compare the results obtained using CS to those obtained with DFT, the same set of f used for DFT is used for CS (see the next section for more detail).

2.3. APPLICATIONS

Three kinds of spike trains were used for comparison between circular statistics and power spectrum: (A) Spike trains with a uniform distribution of interspike intervals, (B) periodic spike trains with a certain "spiking probability", and (C) spike trains from the crayfish photoreceptor. A "raw" signal consists of a sequence of spike times. 100 10-second realizations of the signal were generated for cases (A) and (B) and, for the experimental example (C), a 120 second time series was divided into 12 data sets for averaging. For each of the three examples, the power spectrum (using the discrete Fourier transform) and circular statistics were calculated as follows:

2.3.1. Discrete Fourier Transform (DFT). To calculate the discrete Fourier transform, the signals were digitized at 10,000Hz and each spike was replaced with a pulse with a height of 10,000. The total number of data points was set at 100,000 points since the time interval for one signal was at 10 sec. The frequency bin size for the power spectrum is

$$\Delta f = \frac{1}{L_0} = \frac{1}{N\Delta t} = \frac{1}{100{,}000 \times \dfrac{1}{10{,}000}} = 0.1Hz. \tag{133}$$

The power spectrum was calculated using Eq. 130. All calculations were performed using Matlab (The Mathworks, Inc) and the built-in script was used for DFT.

2.3.2. Circular Statistics (CS). As in Eq. 132, the squared magnitude of the resultant vector was determined for each frequency. The squared magnitude was divided by the time length of the data windows L_0 for the purpose of comparison with DFT. The same set of frequencies as that for DFT were chosen.

Example 1. Time sequence is generated as follows:

$$t_{k+1} = t_k + \xi_n \tag{134}$$

where t_k is a time when the k^{th} spike occurs and ξ_n is random number with uniform distribution from 0.0095 sec to 0.0105 sec. This signal may be considered as a noisy spike train with a mean frequency of 100 Hz.

Example 2. A set of periodic spikes with a certain probability was generated as follows. Let $P(t)$ represent the spiking probability at time t. Suppose

$$\begin{aligned} P(t) &= p \text{ (every } 1/100 \text{ sec)} \\ &= 0 \text{ (otherwise)} \end{aligned} \tag{135}$$

If $p = 1$, the set of spikes will be a completely periodic spike train with a spiking frequency of 100 Hz. $p = 0.2$ were chosen.

Example 3. As an example of biological data, the neural activity of the crayfish photoreceptor is utilized [84, 85]. The crayfish has two light sensitive neurons in its sixth caudal ganglion (i.e., in layperson's terms, "in a nerve in its tail"). These neurons fire periodically, and their firing rate is substantially increased when the cells are exposed to visible light. Furthermore, photoreceptors receive inputs from mechanoreceptors in the tail which are sensitive to periodic hydrodynamic motion (such as, in the wild, the periodic disturbances of the water made by the swimming motions of a predator). It has been observed that the response of the photoreceptors to a weak periodic hydrodynamic stimulus of the tail is enhanced by light [84, 85]. Both DFT and CS are used to calculate the frequency of photoreceptor spike trains in the presence and absence of light, recorded during the mechanical stimulation of the saline-immersed mechanoreceptors with small-amplitude (~ 400 nm) mechanical vibrations at 10.5 Hz.

2.4. RESULTS

The results for CS and DFT are shown in Figure 2.3. In Example A, both CS and the power spectrum showed the largest peak at 100 Hz, and smaller peaks at multiples of the fundamental frequency (Figure 2.3A, left panel).

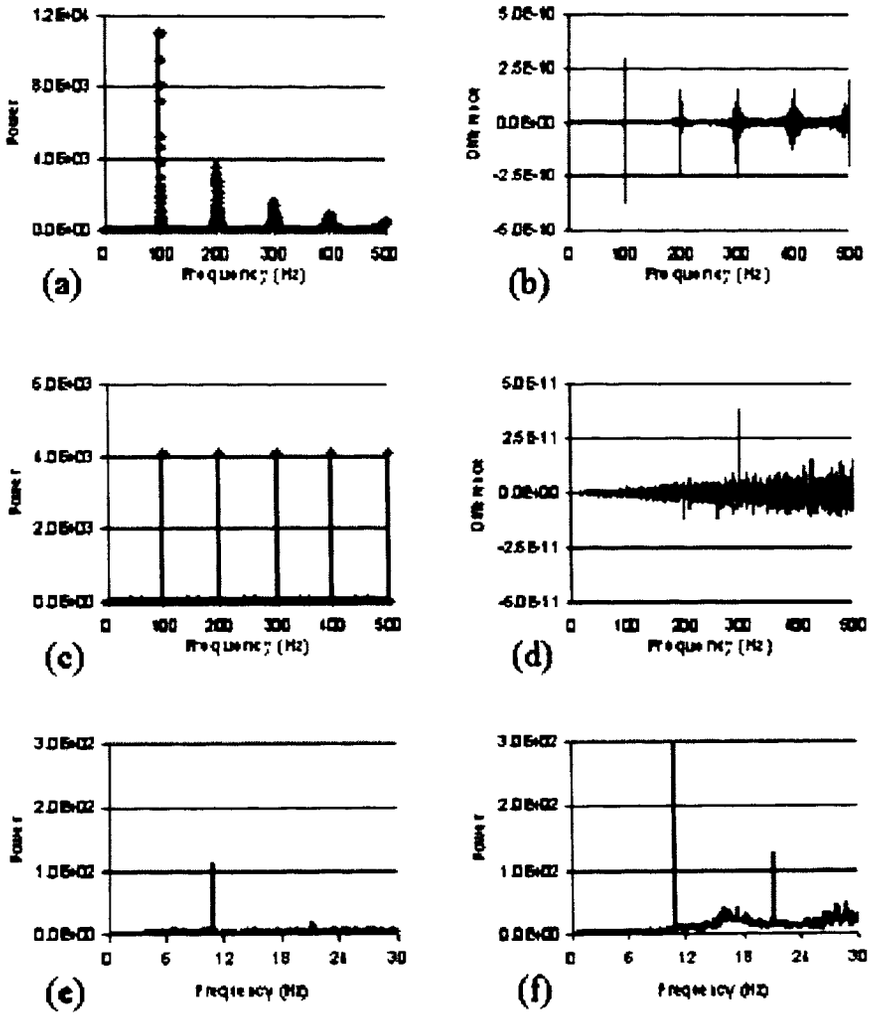

Figure 2.3. Comparison between CS and PS. (A) Circular statistics (diamonds) and the power spectrum (solid lines) of the signals from Example 1. (B) Difference between circular statistics and the power spectrum from (A). (C) Circular statistics (diamonds) and the power spectrum (solid lines) of the signals from Example 2. (D) Difference between circular statistics and the power spectrum from (C). (E) and (F) Circular statistics for the spike trains from the photoreceptor in the crayfish without and with light stimulus, respectively.

In contrast, in Example B, peaks of equal height at all multiples of 100 Hz are observed (Figure 2.3C). The reason for the difference in peak heights between the two examples will be addressed in 2.5. In both examples, CS and DFT showed almost identical results and the difference between two techniques was less than 10^{-9} (Figure 2.3B and D). The small error is likely the result of computer round-off error. In Example C, circular

statistics is plotted for experimental spike trains recorded both in the dark (Figure 2.3E) and in the light (Figure 2.3F). Note the peak at the stimulation frequency (10.5 Hz in this experiment), the broad peak between 14 and 20 Hz in under light stimulation (Figure 2.3F), which results from an increase in the photoreceptor's (noisy) mean firing rate, and the increase in the height of the 10.5 Hz peak in when the photoreceptor is stimulated by light. These results are essentially identical to the power spectra shown for the same data set in [84].

2.5. DISCUSSION

The present study has demonstrated that circular statistics provides a simple geometrical interpretation of the power spectrum of spike trains. In addition, it is also suggested that CS can be helpful in explaining to students some of the qualitative features of the power spectrum. An example is illustrated in Figure 2.4. Consider a completely periodic spike train at 100 Hz. It is obvious that one can expect to see a peak at 100 Hz in its power spectrum. Besides that, by using circular statistics, one can see that one should also expect peaks at multiples of 100 Hz (200, 300, 400, ... Hz). To see this, consider what happens if one calculates the resultant vector for 200 Hz (i.e., T=0.005 s), as shown in Figure 2.4A. Now, the spike appears at the same phase, but only on every other circle. On the other hand, one does not expect to see peaks at 100/2, 100/3, 100/4, ... Hz, as illustrated in Figure 2.4B. If one finds the resultant vector for 50 Hz (T=0.02 s), for example, one can see that each pair of spikes cancels each other on each circle (Figure 2.4B). Indeed, the power spectrum of a periodic spike train at 100 Hz is precisely what one would predict using this argument from circular statistics (Figure 2.4C). This is a straightforward way to introduce students to the idea of why higher harmonics occur, but lower harmonics do not.

An argument using CS can also be used to illustrate the fact that the higher harmonic peaks can have lower amplitude than the peak at the fundamental frequency. This can be illustrated with Example A in Figure 2.3A, where the peaks become smaller as the frequency increases. This can be understood in the following way using circular statistics as shown in Figure 2.5. Since the spike train can be considered one at 100 Hz

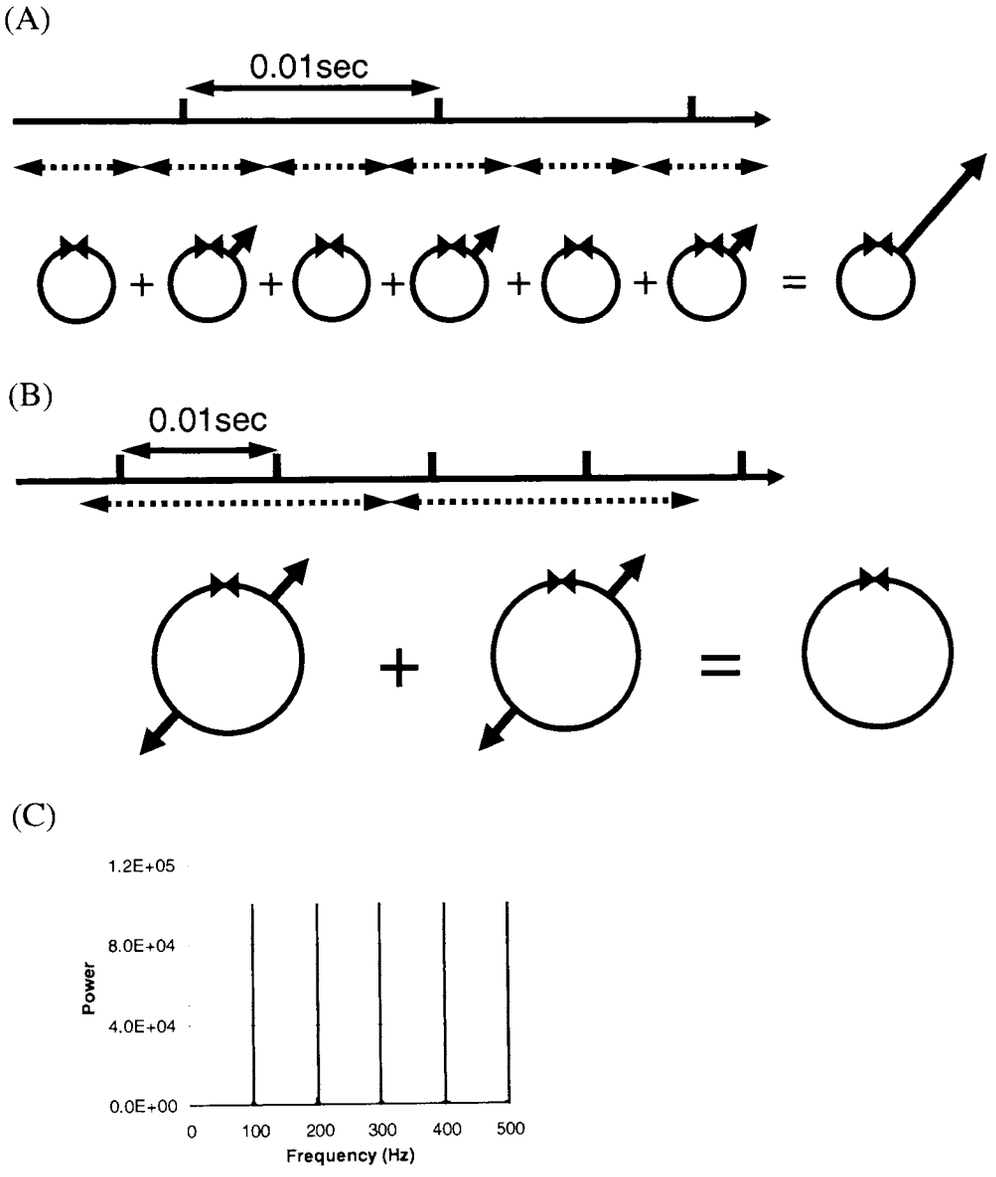

Figure 2.4. Diagrams of circular statistics. Circular statistics is applied to a periodic spike at 100 Hz with circumference (A) 200 Hz and (B) 50 Hz. (C) The power spectrum for a periodic spike train at 100 Hz.

with some jitter (noise) in the frequency, each unit vector is not be at exactly the same phase on the circle, even though one obtains a large resultant vector at 100 Hz (Figure 2.5A). At 200 Hz, one uses circles with half the circumference at 100 Hz (i.e., T=0.005 s instead of T=0.01 s). As a result of this, unit vectors on circles for 200 Hz have a wider

distribution of phases than that for 100 Hz (Figure 2.5B), which results in smaller resultant vector at 200 Hz than that at 100 Hz. At larger multiples of 100 Hz, the distribution of unit vector phases becomes even wider, and, as a result, the resultant vector becomes smaller.

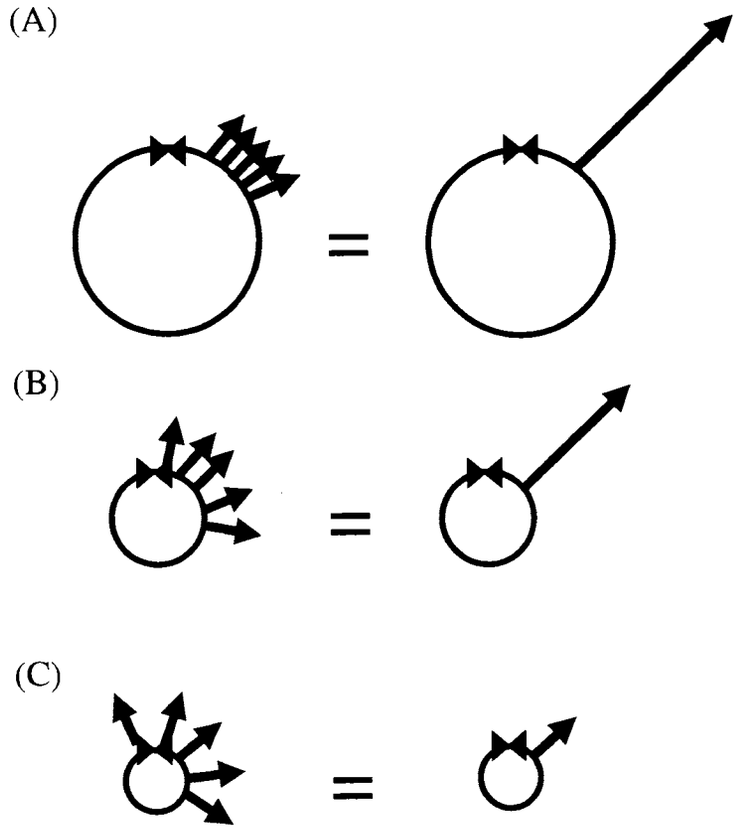

Figure 2.5. Circular statistics applied to spike trains with noise in the frequency. The circumference corresponds to (A) 100 Hz, (B) 200 Hz, and (C) 300 Hz.

In Example B, a periodic spike train is generated with a certain "spiking probability". Definite peaks of equal height at multiples of 100 Hz (Figure 2.3B) are observed. In this example, there is no jitter in the spike times, and thus every spike occurs at exactly the same phase on any circle, regardless of its circumference, and thus the effect illustrated in Figure 2.5 does not occur, and all the peaks have the same height. Note that

the height, however, is considerably lower than in Example A, due to the overall lower number of spikes. This can be seen explicitly from Eq. 132. Here, in the case where spikes always occur at the same phase, the CS value for the corresponding frequency is proportional to the squared number of spikes for a given time interval over which CS is determined. Since p was set at 0.2, the expected number of spikes is $0.2N$ where N is the number of spikes for the completely periodic spike train (p=1.0). Therefore, the ratio of the peak height in this example to the peak height in the completely periodic case is expected to be approximately $(0.2N)^2/N^2$=0.04. In fact, the ratio of the value calculated is 0.041 (=$4.09\text{x}10^3/1.0\text{x}10^5$), which is approximately as predicted.

2.6. CONCLUSION

In the present study, it is shown that circular statistics can be applied to spike trains, and demonstrated its equivalence to the power spectrum. Circular statistics requires only a knowledge of vectors and trigonometry, while calculating the power spectrum requires a knowledge of Fourier analysis. It is suggested that circular statistics may be a useful tool for introducing the concept of the power spectrum in introductory biophysics and neuroscience courses, as well as for helping undergraduate physics students in the first few years of their studies to understand the concepts of frequency analysis.

2.7. SUGGESTED PROBLEM: POISSON SPIKE TRAINS

Construct a spike train as follows. Divide the total time interval T bins of size Δt. Make sure that Δt is small (say $\Delta t=10^{-3}$ s). For each bin, assign a spike with probability p. Adjust p so that the mean spike frequency is, say, 10 Hz (The expected spike frequency is $p/\Delta t$).

1) Calculate the mean and variance, and generate a histogram of interspike intervals.

2) Find the circular statistics. Generate a number of sets of spike trains (say, 100) and calculate the circular statistics for each. Then take the overall average circular statistics. Note that the power spectrum is constant except around 0 Hz.

This process is called a Poisson process [61, 86] and can be constructed as follows [38]. Divide the time interval T into M bins with length $\Delta t=T/M$. Let the probability of the

occurrence of an event within each bin be p and the expected number of occurrences per unit time be $r=p/\Delta t$. Then the probability of having n events within a time interval T is

$$\frac{M!}{(M-n)!(n!)}(r\Delta t)^n(1-r\Delta t)^{M-n}. \tag{136}$$

By taking the limit $\Delta t \to 0$, one can show that the number of events within a time interval T is a random number with a Poisson distribution with a parameter rT. The decay of radioactive particles is a well-known example of a Poisson process [61, 86]. Stochastic neural firing has also been modeled by a Poisson process [38, 87]. In the suggested problem, the process is approximated by small Δt. The distribution of inter-event intervals is an exponential distribution with mean $1/r$. Alternately, setting a time of the n^{th} event as a sum of n random numbers from an exponential distribution with mean $1/r$ gives a Poisson process with parameter rT. For more discussion of a Poisson process, see [61, 86]. It can be shown that the power spectrum of a sequence of delta functions with exponential interval is constant except at zero frequency where there is a delta function singularity because of the nonzero mean of the signal [86].

3. SYNCHRONIZATION ANALYSIS OF VOLTAGE-SENSITIVE DYE IMAGING DURING DRUG-INDUCED SEIZUERES IN THE RAT NEOCORTEX

3.1. OBJECTIVES

The traditional view is that epileptic seizures (see 1.2.11 for some background on epileptic seizures) are defined by excess and/or synchronized electrical activity in the brain [26]. However, the results from some previous studies have challenged the traditional view. For example, lower synchrony is observed during seizure events than during pre-seizure states with whole cell patch clamp in rat hippocampal slices [88]. A few studies have shown decreases in synchrony during seizures in EEG (electroencephalography) and MEG (magnetoencephalography) recordings in human patients, compared to a pre-seizure state [89, 90]. Further motivating the need to study synchrony during seizures are recent studies which have shown that there is a decrease in synchrony prior to seizure onset in EEG recordings from human patients [91, 92]. Therefore, to study synchrony in detail may be crucial to understanding epilepsy.

The purpose of the present section is to investigate how spatiotemporal patterns of synchronization change during drug-induced in vivo neocortical seizures in rats. Focal seizures were caused by the potassium channel blocker 4-aminopyridine (4AP). See 1.2.11.3 and 1.2.11.4 for the discussion of usage of animal models and 4AP-induced epileptic seizures. Electrical activity in the neocortex during 4AP-induced seizures is measured using voltage-sensitive dye imaging (VSD, see 1.3.2). Data obtained from voltage-sensitive dye imaging are analyzed using phase synchronization analysis (see 1.5.5).

3.2. EXPERIMENTAL METHODS

The experimental procedure for voltage-sensitive dye imaging is described in this section. In short, the brain surface of an anesthetized rat is exposed and stained with the voltage-sensitive dye. An injector of potassium channel blocker (4-aminopyridine) and local field potential recording (see 1.3.1 for local field potential recording) were inserted approximately in the center of the exposed area. Changes in reflectance in the brain surface were measured using a CCD camera. The detail of each process is provided in the following subsections. All experiments described here were performed according to

Animal Protocol 05-03-06, approved by the University of Missouri at St. Louis's Institutional Animal Care and Use Committee (IACUC) on March 29, 2005.

3.2.1. Surgery and Staining. Adult male Sprague-Dawley rats (241-573 grams) are used in the present study. The rat is initially anesthetized with intraperitoneal ketamine (90 mg/kg) and xylazine (4.0 mg/kg) and then sustained with urethane (1.25g/kg). Temperature is maintained at 37°C with a heating blanket (Harvard Apparatus, Holliston MA). Heart rate, O_2 saturation and PCO_2 are monitored (SurgiVet, Waukesha, WI) and maintained stable. The electrocardiogram (EKG) is monitored between leads attached to the right hindlimb and the skin of the scalp. To control the timing of respiration for artifact reduction (see 3.3.1.4), the rat is artificially ventilated with an animal respirator (Kent Scientific, Torrington CT).

The rat is placed in a stereotaxic frame, the skin above the skull shaved, and the scalp incised along the midline. A cranial window (~5 by 9 mm) is made over one hemisphere, between lambda and bregma. This is translated, in layperson's language, to "a rectangular hole is made in the skull to expose the brain surface with reference to some anatomical landmarks on the skull of the rat", as shown in Figure 3.1.

The dura (thin membrane-like structure between the brain and skull) over the window is removed for dye staining. The solution of the voltage-sensitive dye, RH-1691 (Optical Imaging, Inc., 1.0-2.0 mg/ml in 1% NaCl solution) is applied to the cortex for 1-2 hrs. After staining, the cortex is washed by NaCl solution for 15 min.

3.2.2. Electrophysiology. A glass micropipette filled with 1% NaCl is positioned with its tip in the dural slit, approximately 500 μm below the neocortical surface, for the local field potential recording. The field potential and EKG are recorded using a DBA-S system (World Precision Instruments, Sarasota FL), digitized at 2000 Hz by a CED Power 1401 (Cambridge Electronic Design, Cambridge UK), and recorded onto a PC using Spike 2 software.

3.2.3. Drug Administration. The injection of 4AP was performed in a similar method to that by [93]. A glass pipette, filled with a solution of 4AP, and attached to a Nanoject II Auto-Nanoliter injector (Drummond Scientific, Broomall PA), is positioned less than 1 mm from the field potential electrode. One set of injections contained 0.5 μl of 4-AP (25 mM in 1% NaCl), which was injected into cortical layers approximately II-III

(see 1.2.9.1 for the laminar structure of the neocortex), in increments of 50 nl. Seizures occurred multiple times without additional injection, although time intervals between seizures tended to become longer at later stages of the experiment (see 3.4.1 for more description of this). When no seizure occurred for more than 20-30 minutes, an additional set of injections of 4AP was performed.

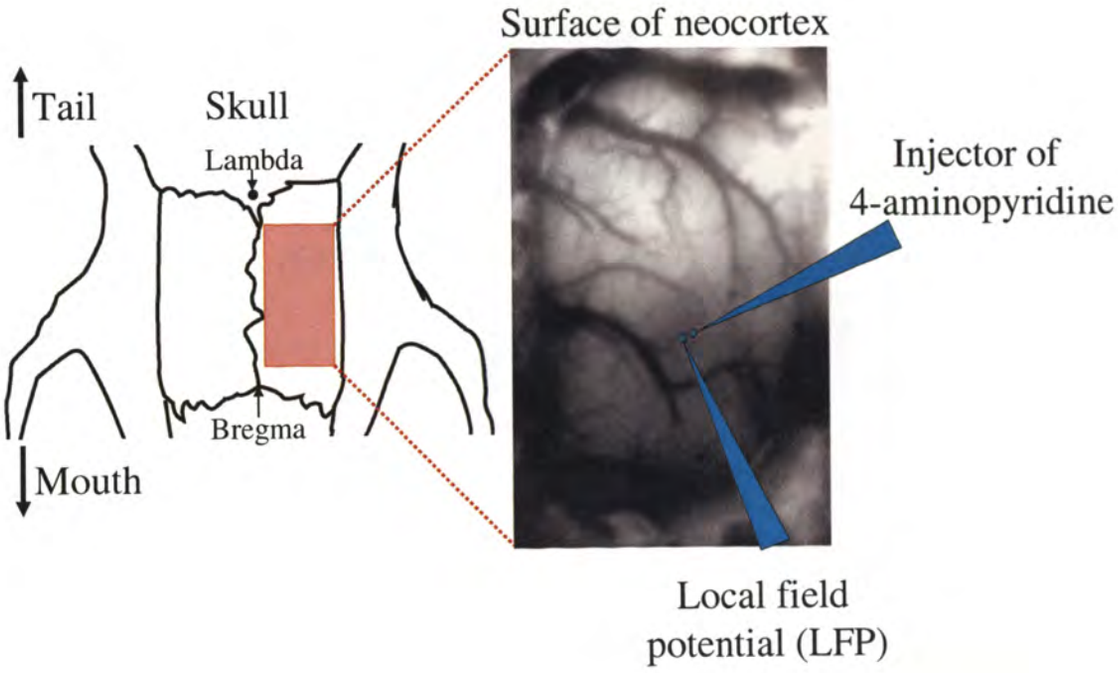

Figure 3.1. Cranial window on the skull of the rat. *Left:* The position of craniotomy window. *Right:* The arrangement of electrodes in the neocortex.

3.2.4. Recording. A schema of the recording setup is shown in Figure 3.2. Agar (1.5% in 1% NaCl) and a glass cover slip are placed over the cortex. The cortex is illuminated using a 100W tungsten-halogen bulb. The light is passed through a macroscope and 630 ± 20 nm interference filter (Optical Imaging Inc) and reflected down onto the cortex via a dichroic mirror (Optical Imaging Inc). The fluorescence of the dye from the stained cortex is filtered by a 695 nm long-pass filter (Optical Imaging Inc), and projected to the a 16-bit CCD camera, which is placed over a tandem configuration of two

50 mm lenses [94]. The camera is focused about 300-500 μm below the cortical surface in order to de-emphasize the changes in reflectance from the surface blood vessels in preference to the neocortical layers. The camera images are synchronized with the recorded field potential via a TTL pulse.

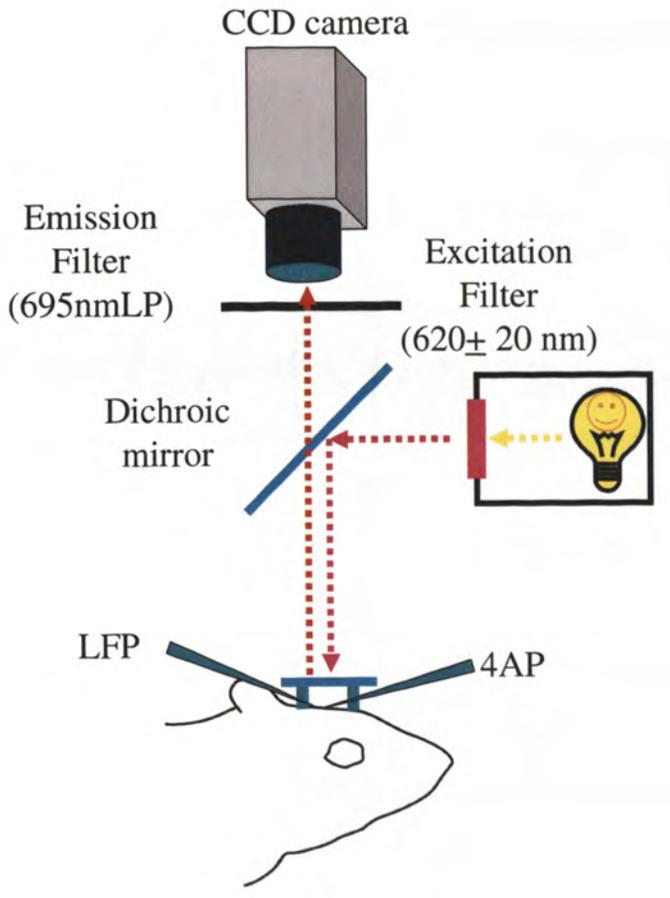

Figure 3.2. A schema of the recording setup.

3.3. DATA ANALYSIS

The analysis of VSD imaging is divided into three components: (1) the reduction of noise and artifact, (2) determination of seizure area, and (3) synchronization analysis.

3.3.1. Noise/Artifact Reduction. There are several sources for noise and artifact: drift of signal baseline, random noise inherent to photon counting and measurement with the CCD sensor, and artifacts due to respiration and heartbeat. The detail is discussed in the following subsections. Figure 3.3 shows a comparison among raw signal and processed signals from voltage-sensitive dye signal, and local field potential signal. While it is hard to see the correspondence between the raw VSD signal and the local field potential, there is a sufficiently clear correspondence between the processed VSD signal and local field potential signal. Note that the VSD signals will be filtered further for phase synchronization analysis as discussed in 3.3.3

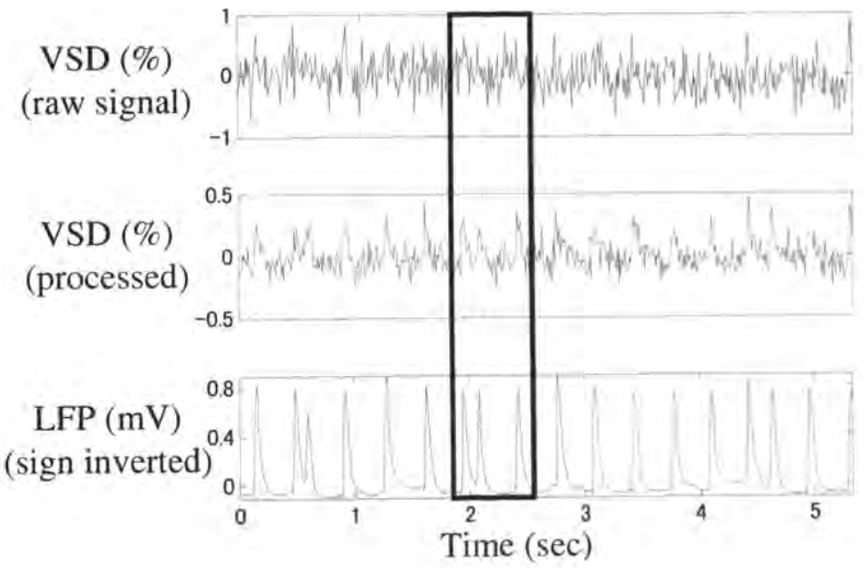

Figure 3.3. Comparison among the raw and processed voltage-sensitive dye signals, and local field potential during a seizure event. The VSD signals are plotted as the percent change with respect to the averaged intensity over the time interval shown.

3.3.1.1 Baseline drift. It is known that the recording time of voltage-sensitive dye imaging is limited by dye bleaching [95]. In the case of in vivo imaging, dye may get washed away due to blood circulation [96]. These factors cause a drift in the baseline in measured fluorescence intensity. It is critical to remove the drift especially

since the recording time of imaging during one seizure event is much longer than that of a single trial performed in studies of cognitive functions, where voltage-sensitive dye has been often used. The baseline drift was removed using regression by a 10^{th} order polynomial. In addition to the baseline drift, a large oscillation at very low frequency (less than ~0.2 Hz) was observed associated with seizure events. This is likely to be contamination due to hemodynamics and was removed with high-pass filtering at 0.2 Hz.

3.3.1.2 Random noise. There was random fluctuation which was possibly caused by the statistical fluctuation of the number of photons arriving at the CCD (called photon noise) and by the process of quantifying the electronic signal on the CCD (called read noise). This noise was reduced by spatial averaging over neighboring 3 by 3 pixels at each frame. This is reasonable, assuming that the noise of this kind is statistically independent (or uncorrelated) between signals from different CCD sensors.

3.3.1.3 Heartbeat artifact. Although RH-1691, which is the voltage-sensitive dye used, has been developed to reduce contamination due to hemodynamics (see 1.3.2 for more discussion), a very sharp peak in the power spectrum was observed at the rate of the heart beat. A previous study has suggested that this might be caused by physical movement (e.g., movement of blood vessels caused by the heartbeat) rather than absorption of light by the hemoglobin [96].

To reduce the heartbeat artifact, a template of the artifact was constructed using the triggered averaging of the voltage-sensitive dye signal was performed with reference to EKG signal as suggested by [96, 97]. The signal is concatenated using weighted averaging to avoid discontinuity in the signal.

3.3.1.4 Respiration artifact. After removing the dura, the movement of the brain surface synchronized with the respiration of the rat was often clearly visible, even to the naked eye. Corresponding periodic oscillations at the frequency of the respiration were observed in the voltage-sensitive dye signals. This artifact was removed by triggered averaging similar to the removal of heartbeat artifact. Averaging was triggered by electrical pulses received from the ventilator (see 3.2.1), corresponding to the timing of the animal's respirations.

3.3.2. Determination of Seizure Area. Each pixel at every time instant from the imaging signal during a seizure event was determined whether "epileptic" or not based on the value of power spectrum of the signal before a seizure event. The method developed by [93] was modified for this purpose. The power spectrum was calculated, using a sliding window of 1,000 data points (about 10-13 seconds) with 100 point shift, for voltage sensitive dye recordings both before and during the seizure event. For a each window, the sum of five largest peak values in the frequency range of 1-10 Hz in the power spectrum was determined. This frequency range was chosen based on the observation that the peaks in the power spectrum during seizure events appear in this frequency range. Each pixel at each time window was classified as part of the seizure event if the sum of the five largest peak values exceeded a threshold value determined from the pre-seizure state. The threshold value was determined for each pixel as 1.5 times the maximum of the summed peak values from sliding time windows in pre-seizure state.

3.3.3. Synchronization Analysis. Phase synchronization analysis (see 1.5.5) was applied to the voltage-sensitive dye signals. After the noise/artifact reduction process described in 3.3.1, the time course of light intensity from each pixel was filtered using a zero-phase band-pass digital filter (Butterworth 4^{th} order, 1-10 Hz). As described in 3.3.2, this frequency range was chosen based on the observation that the peaks in the power spectrum during seizure events appear in this frequency range. Phase synchronization analysis was performed, using a sliding window of 1,000 data points (about 10-13 seconds) with a 100 point shift. For a given set data, a pixel which was estimated to be the place of injection of 4AP was chosen as a "reference" pixel. For each sliding window, the synchronization index was calculated for every pixel with respect to the reference pixel. All the analysis was performed using custom-written programs in MATLAB (The Mathworks).

3.4. RESULTS

A complete set of experiments were performed for six rats. However, the results from only three rats are shown below. In two of the three rats not used for the results, the data from the voltage sensitive dye imaging were contaminated with unknown large signals. Since the amplitude of the signals was much larger than those from seizure

activity, it is unlikely that the artifact is due to electrical activity in the brain. In the other rat, respiration artifact was not able to be removed by the triggered averaging discussed in 3.3.1.4. Therefore, the data from these three rats were excluded from the results below, although further signal processing might be able to be utilized to remove the artifacts.

3.4.1. Description of Seizure Events. Seizure events are defined by sustained activity of large oscillations in the local field potential recording (see the top panel in Figure 3.4). The first seizure after the first set of injections of 4AP usually occurred within a few minutes from the injection. Seizures occur multiple times without additional injection of 4AP. The duration of seizures varied both within the same rat and among rats. Seizure duration tended to be short (about 10-60 seconds) right after injection of 4AP and to become longer and, eventually, to reach a plateau (about 200-300 seconds) without additional injection of 4AP, although short seizures sometimes appeared between long ones even at later stage of an experiment. A typical time interval between seizure events was a few minutes although, in some cases, it was as short as a few seconds. The time intervals between seizure events tended to be longer at later stages of an experiment, which was as long as 20-30 minutes.

3.4.2. Patterns of Local Field Potential during Seizure Events. In this subsection, typical patterns of the signals from local field potential during seizure events are described (see the bottom panels in Figure 3.4). However, it is important to note that there is variability among seizure events and rats. Seizure events often begin with a large spike followed by relatively fast oscillations with increasing amplitude (see the panel showing the time interval 77-82 sec in Figure 3.4). In the middle of a seizure event, periodic spiking with constant large amplitude is observed (100-105 and 160-165 sec in Figure 3.4). As the seizure event nears its end, firing becomes irregular and bursting patterns are often observed (230- 235 sec in Figure 3.4).

3.4.3. Change of Seizure Area over Time. An example of the changes in seizure area determined by the method in 3.3.2 is shown in Figure 3.5. The epileptic area typically increases quickly at the beginning of a seizure event and stays almost constant throughout the duration of the seizure. A sudden decrease of the area is observed at the end of each seizure event. In this particular example, the area drops around 200 seconds and stays almost constant from 200 to 250 seconds, while the amplitude of the local field potential

shows an increase during this time interval. Within this time interval, the local field potential shows irregular bursting pattern (see right bottom panel in Figure 3.5). This might relate with the smaller seizure area, although more careful analysis would be necessary to support this claim.

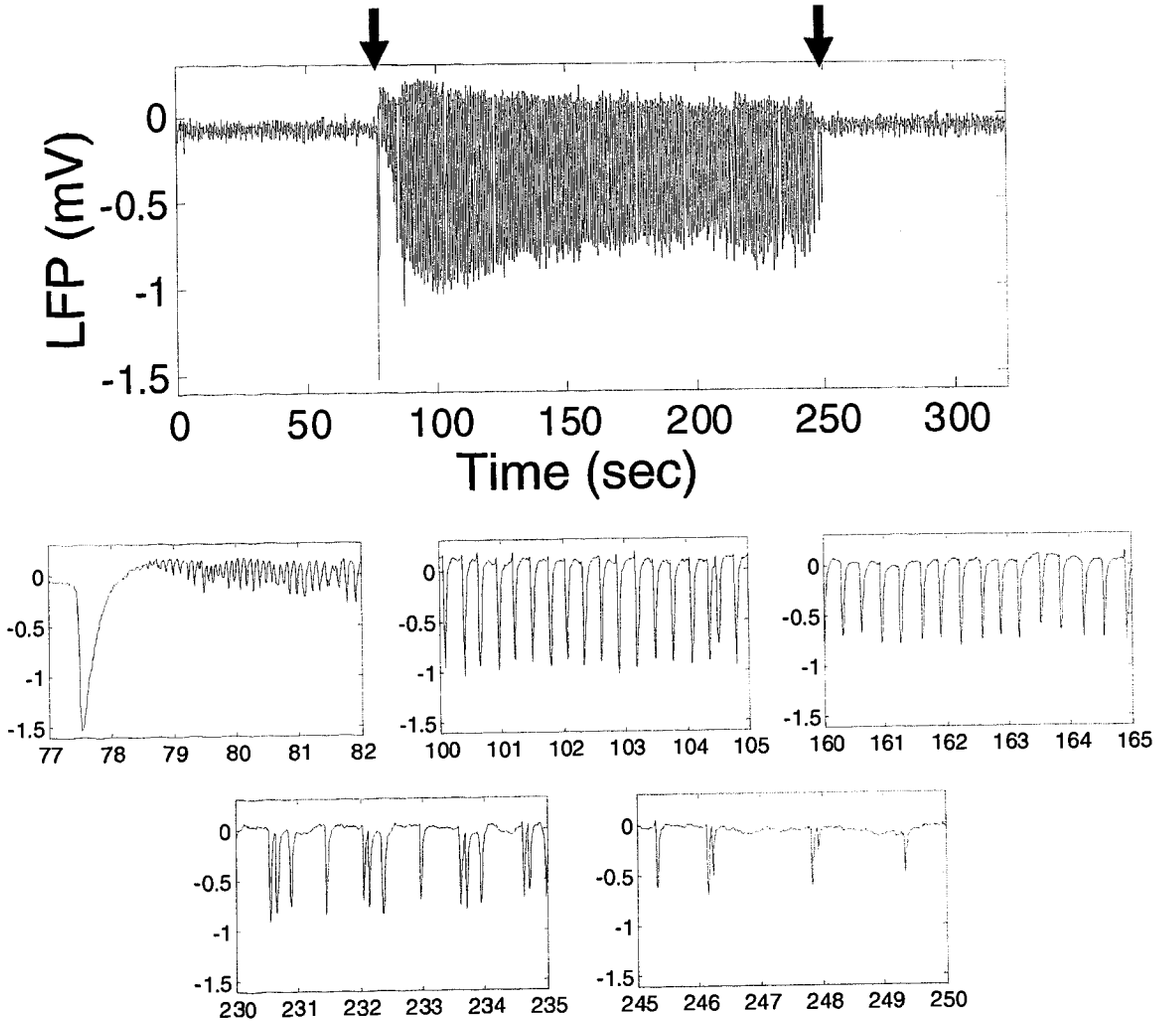

Figure 3.4. Example local field potential patterns during a seizure event. *Top*: Local field potential for the entire duration of a seizure. The arrows indicate the beginning and ending of the seizure event. *Bottom*: Blowups of the top panel.

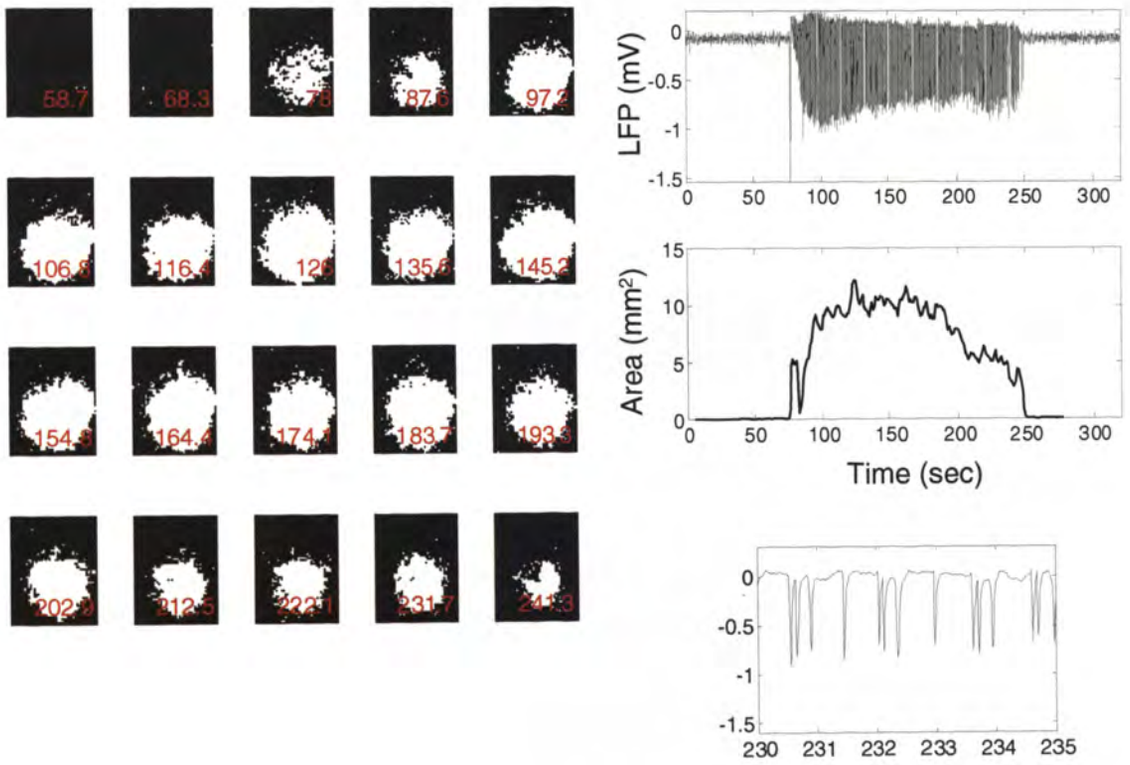

Figure 3.5. Time course of seizure area. *Top right*: The changes in the local field potential and seizure area over time. *Bottom right*: the blow up of local field potential toward the end of the seizure event. *Left*: The patterns of seizure area in space. The white regions are classified to be "epileptic" using the criterion described in the main text The red number in each picture represents the time in the right panel.

3.4.4. Phase Synchronization. An example of the changes in synchronization indices over time from multiple pairs of pixels throughout the seizure area is shown in Figure 3.6. As seen from this example, a dramatic increase in synchronization during seizure events is observed. One can also observe that closer pairs of pixels show stronger synchronization than pairs separated by a larger distance. Even widely separated pairs of pixels within the seizure area, however, show a significant increase in synchronization during the seizure event.

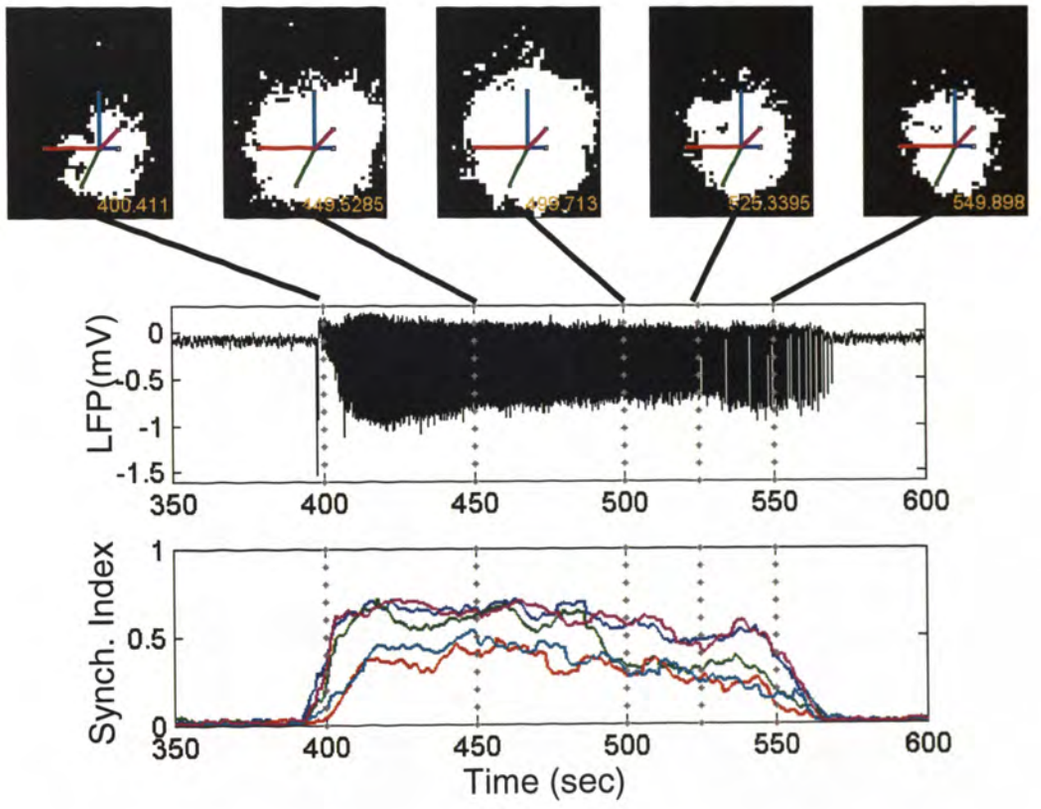

Figure 3.6. LFP and γ (synchronization index) before and during seizure event. Lower panels show LFP and γ; upper panels show the seizure area. Synchronization index in the bottom panel is shown for the pixel pairs corresponding to the colored lines in the seizure maps. The pixel pairs chosen always included one pixel approximately at the 4AP injection site.

To investigate the time course of spatially averaged synchronization behavior, the averaged synchronization index is calculated as the average of synchronization indices over all the pairs, one member of which is always a pixel located at or near the 4AP injection site. A dramatic increase in the averaged synchronization index is observed during seizure events (see the right panels of Figure 3.7 and Figure 3.8).

The changes in spatial distribution of synchronization indices over time are shown in the left panels of Figure 3.7 and Figure 3.8. As time increases from the onset of the seizure events, the synchronized region increases in both area and degree of synchronization. In the middle of seizure, most of the pixels in the recorded area are well

synchronized with the 4AP injection site. At seizure termination, the synchronized region decreases in both area and degree of synchronization.

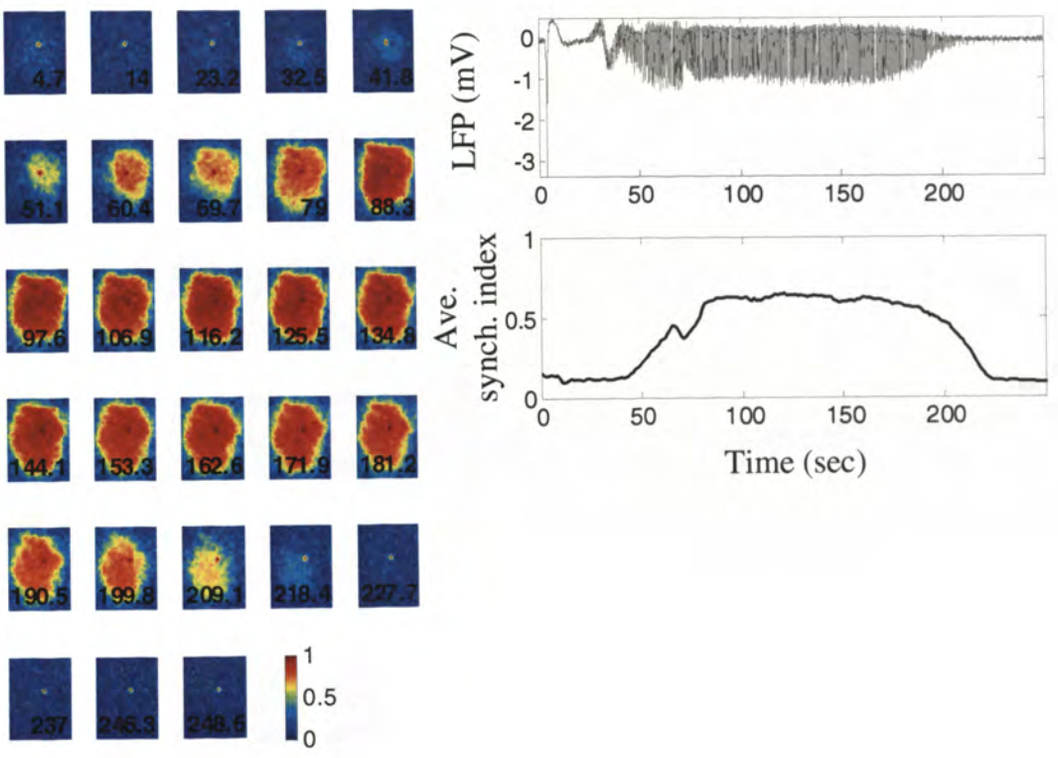

Figure 3.7. Changes in overall synchronization index and spatial map of synchrony. *Left*: color map of synchronization indices of each pixel with reference to the 4AP injection site. The color scale is shown at the end of the sequence of the color maps. The black number in each figure indicates time in the right panel. *Right*: changes in LFP and overall synchronization index over time.

Two things are worth commenting from these examples. In the case of Figure 3.7, there is a slight decrease in the averaged synchronization index (around 70 sec). The local field potential recording at the corresponding time shows a decrease in the amplitude. In the case of Figure 3.8 (see the 2nd row in the color maps), at the beginning of the seizure

event, there are two clusters of synchronized regions. One of these encloses the pixel of the injection site, while the other is distant from the injection site. Although these observations are quite intriguing as a collective phenomenon in an excitable system, more detailed analysis will be necessary to make a general conclusion.

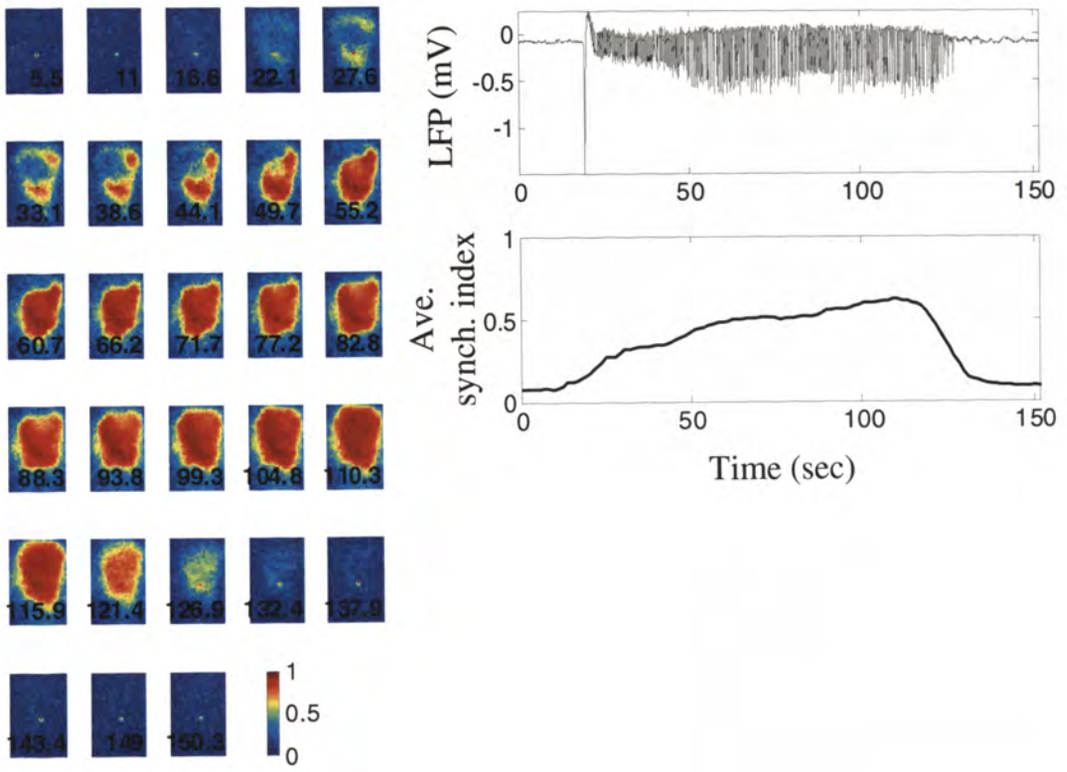

Figure 3.8. The same plot as Figure 3.7, but showing a seizure event in another rat. Note the two areas of high synchronization early in the seizure (33 seconds – 44 seconds).

In order to perform a statistical analysis, the maximum spatially averaged synchronization index before and during each seizure event was calculated as the maximum spatially averaged synchronization index over time (over sliding windows) in the respective time periods (Figure 3.9). A paired t-test was performed for 37 seizure

events from the 3 rats, in order to compare the maximum synchronization index prior to each seizure with that during the seizure. The p-value from the statistical test was very small ($p<0.00001$). Therefore, the maximum averaged synchronization index during seizure events was significantly larger than that before seizure events.

3.4.5. Phase Maps. In addition to measurements of the synchronization index, the collective behavior of the neocortical tissue during the seizure event can be visualized by mapping the phase derived from the Hilbert transform (1.5.5) at every pixel in the recorded image, as a function of time. A typical example of the distribution of the phases is shown in Figure 3.10. The distribution of the phase over space at a given time shows a clear difference between the periods before and during the seizure event. Before the seizure event, the distribution of phase looks almost random. On the other hand, during the seizure event, most of the pixels show an in-phase pattern, although it is often observed that one region is slightly advanced in phase with respect to the rest of the seizure area.

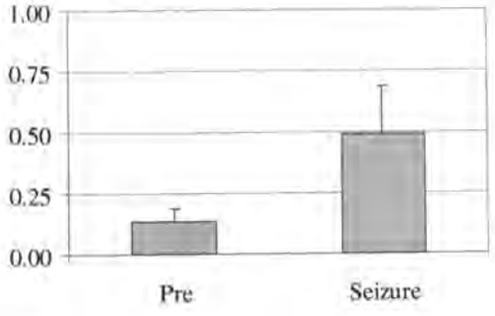

Figure 3.9. Maximum averaged synchronization indices before and during seizure events. As discussed in the main text, the difference is statistically significant.

The degree of the concentration of the distribution of the phase at a given time is evaluated by the following measure (see Eq. 146 in 4.3.4 for more detail):

$$R_1(t) = \left| \frac{1}{N} \sum_{k=1}^{N} \exp[i\phi_k(t)] \right|, \tag{137}$$

where $\phi_k(t)$ is the phase of the signal from the k^{th} pixel at time t and N is the total number of pixels in a two-dimensional image. There is a clear increase in $R_1(t)$ during seizure event, which indicates in-phase activity (Figure 3.10, right).

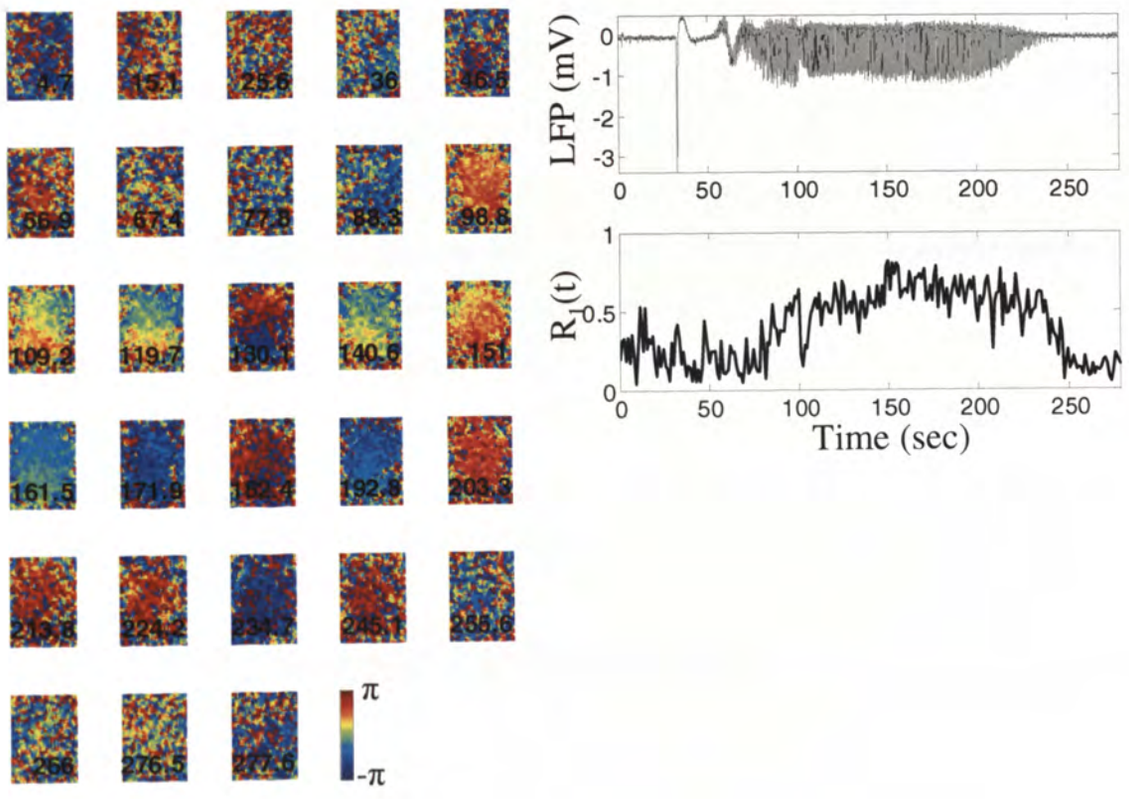

Figure 3.10. Phase map of voltage-sensitive dye imaging during a seizure. *Left*: the phase of the signal from each pixel is coded in color. The number in black in each figure corresponds to the time in the right graphs. *Right*: the local field potential and $R_1(t)$ as defined in Eq. 137.

3.5. DISCUSSION

3.5.1. Comparison with Previous Studies. Some previous studies have shown that, in some situations, synchrony between signals from two distant locations in the brain was lower during the seizure event than before the event [88, 89, 98]. As far as the averaged synchronization index in the present study is concerned, greater synchrony during the seizure event than pre seizure state was observed in all the 37 seizure events from 3 rats analyzed in the present study.

However, it is important to note that the differences in the results might be caused by the systems studied. For example, Netoff and Schiff studied synchrony using whole-cell patch recording from a pair of pyramidal neurons in hippocampus [88]. Their recording technique measures electrical activity at a single neuron level, while the voltage-sensitive dye imaging performed here measures activity at a population level. Furthermore, in [88], seizure-like events were caused 4AP in hippocampal slices in the rat, where 4AP is globally applied to the brain slice. On the other hand, in the present study, 4AP is locally applied through an injector in vivo neocortex in the rat.

In [98], phase synchronization analysis was applied to MEG (magnetoencephalography) recordings from human patients with generalized seizures (see 1.2.11.2 for generalized seizures). Their results show that, while the local synchrony (between neighboring pairs with distance less than 4 cm) increased during seizures, the distant synchrony (>4 cm) sometimes showed lower synchrony during seizures than during states between seizures. They commented about this lower synchrony that "although not uncommon, this marked desynchronization between particular channels during the ictal [seizure] period was not the rule in the patients studied". Again, there are important differences: seizures they studies are generalized seizures while the animal-seizure model in the present study is a model for the focal seizure.

In [89], a measure for the overall synchrony among multivariate signals was developed based on the random matrix and was applied to signals from epileptic patients recorded with EEG (electroencephalogram) and ECoG (electrocorticogram). The authors reported that there are relatively more cases where the overall synchrony decreased during seizures. It may be possible that the measure in [89] is more sensitive to subtle changes in the overall synchrony than the averaged synchronization index used in the present study

and that decrease in the overall synchrony during seizure events could be observed in the present study using the measure developed in [89].

3.5.2. Future Work. There are several aspects which have not been investigated in the present study. In studies with epileptic patients, it has been reported that there is a dependence of the degree of synchrony on the frequency band of signals studied [98]. Note that the frequency range of epileptic activity investigated in the present study (1-10 Hz) is much smaller than that in [98] (3-55 Hz). It is possible that increased synchrony may occur during seizures in certain frequency ranges and not in others, and that this may underlie some of the disparate results within the literature.

Another problem for further investigation is the correlation between synchrony and spatiotemporal evolution of the seizure event. For example, one could ask whether there are differences in synchrony during different time stages of the seizure event such as beginning and ending. In the present study, the synchronization index was calculated for pairs of pixels, one of which was always from the estimated injection site of the seizure-inducing drug, 4AP. However, synchrony with respect to a distant pixel from the injection site may reveal different patterns of synchrony.

The local field potential recording during seizures shows a variety of firing patterns such as periodic spiking and bursting (see Figure 3.4).Another subject for further investigation is the relationship between field potential oscillation patterns (amplitude, frequency and irregularity) and synchrony.

3.5.3. Limitation of the Present Study. The voltage-sensitive dye imaging used in the present study mainly reflects the electrical activity from a population of neurons (as does the local field potential) rather than single cells (action potentials). It would be intriguing to simultaneously measure signals in both a population and single cell levels from multiple places, using an array of multi-electrodes. This may reveal how the activity at a population level is related with the activity of individual neurons during the seizure event.

The preliminary experiments performed have shown that the presence of the voltage-sensitive dye itself alters the dynamics of the seizure event. Seizures induced by 4AP injection without the presence of the dye occur much more frequently than when neocortex is stained with RH-1691. This may be due to phototoxic effects on the neural

activity [95]. A recent study has shown that some voltage-sensitive dyes, including the one used in the present study, affect the function of GABA-A receptors, which are receptors for an inhibitory neurotransmitter (see 1.2.7 for basic terminology) [99]. Therefore, the results from the present study should be interpreted with some caution.

3.6. CONCLUSION

The present study has focused on 4-aminnopyridine induced seizures in the rat neocortex. The results show that there is significant increase in the overall synchrony during seizure events and that synchrony was greater between closer pixel pairs during a seizure event. The entire "epileptic" region is synchronized almost in phase.

4. MODELING SEIZURE DYNAMICS

The study in this section is reprinted with some modifications with permission from Daisuke Takeshita, Yasuomi D. Sato, Sonya Bahar, Physical Review E 75, 051925, 2007.

4.1. OBJECTIVES

In addition to synchrony, another interesting dynamical aspect in epileptic seizures (see 1.2.11 for some basics about epileptic seizures) is that changes in amplitude and frequency of electrical activity are often observed during seizure events in both human patients [100, 101] and animal models [102]. Various computational models of seizure onset and progression have been developed [103, 104], but many questions remain unanswered.

In this section, a possible dynamical mechanism for seizure initiation, and for dynamical changes in electrical activity during seizure events is reported. A model of a neocortical network based on a nonlinear model suggested by Wilson [105], (Eqs. 1-4 below) is developed. The effect of the potassium channel blocker 4-aminopyridine (4AP, see 1.2.11.4), used experimentally to induce seizures [93], is simulated by decreasing the model's maximal K^+ channel conductance (g_k). Phase reduction analysis [50, 106] (see also 1.5.4) is used to demonstrate that the phase relationship of a pair of synaptically coupled neurons undergoes a bifurcation as g_k is varied. Multi-stability is observed in the stable fixed phase difference, and a dramatic increase in the activity of a larger network of neurons correlates with the bifurcation.

4.2. NEOCORTICAL NEURAL MODEL

The dynamics of a single neuron is represented by a set of nonlinear ordinary differential equations [105], which belongs to a class of conductance-based models explained in 1.4:

$$C\frac{dV}{dt} = -m_\infty(V)(V-0.5) - g_K R(V+0.95) - g_T T(V-1.2) - g_H H(V+0.95) + I \quad (138)$$

$$\frac{dR}{dt} = \frac{1}{\tau_R}(-R + R_\infty(V)) \tag{139}$$

$$\frac{dT}{dt} = \frac{1}{\tau_T}(-T + T_\infty(V)) \tag{140}$$

$$\frac{dH}{dt} = \frac{1}{\tau_H}(-H + 3T), \tag{141}$$

where V is the membrane potential, and R, T, and H are the conductance variables for K^+, Ca^{2+}, and Ca^{2+}-mediated K^+ hyperpolarizing currents, respectively. The following variables depend on V:

$$m_\infty(V) = 17.8 + 47.6V + 33.8V^2 \tag{142}$$

$$R_\infty(V) = 1.24 + 3.7V + 3.2V^2, T_\infty(V) = 8(V + 0.725)^2. \tag{143}$$

System parameters are given as follows: $C = 1.0\ \mu\text{Fcm}^{-2}$, $I = 0.7$ nA, $\tau_T = 14$ ms and $\tau_H = 45$ ms. The first term in Eq. 1 represents the Na^+ current; the Na^+ channel dynamics is incorporated into $m_\infty(V)$ instead of using a conductance variable. In the model equations, V is scaled by 1/100 with respect to realistic membrane potential values in order to keep the constants in m_∞ etc. within a reasonable range. In the figures below, V is rescaled by 100 (mV) in order to return to biologically realistic values. The model can be tuned to exhibit the behavior of the three major subtypes (regular spiking, bursting, and fast spiking inhibitory) of neocortical neurons by changing g_K, g_T, and g_H [105]. However, only a single subtype, the regular spiking mode ($g_K = 26.0, g_T = 0.1$, and $g_H = 5.0$), which corresponds to the largest population of neocortical neurons [19], is considered in the present study.

Chemical synaptic coupling (see 1.2.7 for chemical synapse) is modeled using an alpha function [107]:

$$\frac{df}{dt} = \frac{1}{\tau_{syn}}(-f + Hvs(V_{pre} - \Omega)) \tag{144}$$

$$\frac{dS}{dt} = \frac{1}{\tau_{syn}}(-S + f) \tag{145}$$

where V_{pre} represents the voltage of the presynaptic neuron, $\tau_{syn} = 0.5$ ms, $\Omega = -0.2$ mV, and the Heaviside function $Hvs(V_{pre} - \Omega) = 1$ for $V_{pre} - \Omega > 0$ and 0 for $V_{pre} - \Omega \leq 0$. The effect of synaptic coupling is incorporated into the dynamics of each neuron by adding the term $-Sg_{syn}(V - V_{syn})$ to Eq. 1, where g_{syn}, the synaptic strength, is set at 0.1, and V_{syn}, the synaptic reversal potential, is 0 mV, which mimics the effect of an excitatory synapse (see 1.2.7).

4.3. RESULTS

4.3.1. Phase Reduction. Phase reduction analysis (1.5.4.3) is performed for a pair of model neurons with bidirectional synaptic connections. Plots of $d\phi/dt$ as a function of ϕ are shown in Figure 4.1. At normal g_K ($g_K = 26.0$), the stable phase difference is small (filled circles, inset, Figure 4.1A), but nonzero, so that the neurons are almost, but not exactly, in phase. In fact, two stable states coexist, one where neuron i fires first and neuron j fires shortly afterwards, and vice versa. Since the two neurons are identical, this bistability is trivial in the sense that, if ϕ is stable, then so is $2\pi - \phi$. The time delay in firing between the two neurons corresponds to τ_{syn}. A similar "trivial bistability" was observed by Van Vreeswijk et al. in the Hodgkin-Huxley neural model with synaptic coupling [108].

At high values of g_K, only the "trivial" bistability is observed. At $g_K \approx 5.0$, a subcritical pitchfork bifurcation (see 1.5.3 for some discussions about bifurcation and [44] for pitchfork bifurcation, in particular) occurs, as a result of which an antiphase firing pattern becomes stable (Figure 4.2). Also at $g_K \approx 5.0$, the "trivial" bistable states coalesce into a single stable branch (at $\phi = 0$) corresponding to exactly in-phase firing.

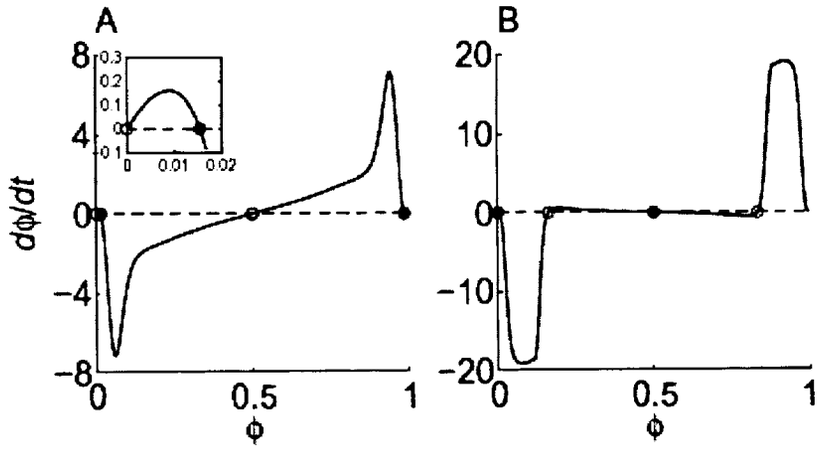

Figure 4.1. Results of phase reduction applied to the neocortical model. A: $d\phi/dt$ at $g_K = 26.0$; B: $d\phi/dt$ at $g_K = 0$. Open and filled circles correspond to unstable and stable fixed points, respectively. Phase difference is normalized to [0,1]. The inset shows a blow-up around ϕ=0.

Thus, for low conductance, there exists a "non-trivial" bistability. These results were confirmed by numerical integration (4th order Runge-Kutta, $dt = 0.01$ ms), using a variety of different initial conditions (data not shown).

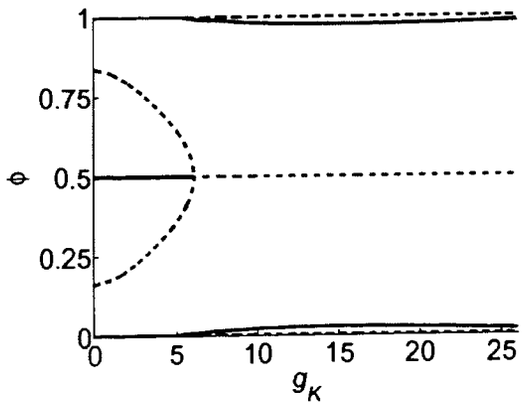

Figure 4.2. Bifurcation diagram. Thick and thin lines represent stable and unstable fixed phase differences, respectively. Phase difference is normalized to [0,1].

4.3.2. Effect of Noise -- Two Neuron Case. To study the effect of noise on the behavior of a pair of neurons, an independent Gaussian white noise term $\xi(t)$ was added to each dV/dt equation; the noise was defined such that $\langle \xi(t) \rangle = 0$ and $\langle \xi(t)\xi(s) \rangle = D\delta(t-s)$, where D is the noise intensity. The stochastic differential equations (see 1.7 for some basics about stochastic differential equations) were solved by the Heun method [109] with $dt = 0.01$ ms. Transitions between the bistable states were observed for $g_K = 0$, as illustrated by the mean field (average voltage from the two neurons) in Figure 4.3. At normal g_K (Figure 4.3A), transitions between the "trivial" bistable states are observed, which do not significantly affect the mean field. Since the spikes from the two neurons rarely coincide in time, the mean field has an amplitude half as large as the transmembrane potential of a single neuron throughout most of the simulated time series. The sharp spikes in the mean field corresponds to the moments when the two neurons fire simultaneously. At $g_K = 0$ (Figure 4.3B), noise-induced transitions between in-phase and antiphase states were observed; these transitions significantly affect the mean field, in contrast to the case of normal g_K.

4.3.3. Network without Noise. In order to investigate the role of decreased g_K on the activity of a larger array, a square lattice of 20 by 20 neurons is constructed with bidirectional nearest neighbor synaptic coupling. It is suggested that the results of phase reduction analysis for two neurons can give a qualitative explanation of the network behavior as shown in Figure 4.4. When g_K was decreased to zero (Figure 4.4 A, 2.5×10^4 ms), to simulate the addition of 4AP, a dramatic increase in the mean field amplitude was observed (Figure 4.4 A). A raster plot (Figure 4.4 B) shows that, before decreasing g_K, the neurons do not all fire in phase, which results in a small mean field amplitude. It is suggested that this corresponds to the case of two neurons, in which a non-zero phase difference is stable, whereas in-phase is unstable. In contrast, after decreasing g_K, where in-phase is stable, the neurons fire in phase, leading to large-amplitude mean field oscillations. These results, in a spatially extended array of neurons, are consistent with the result of phase reduction analysis for a pair of neurons.

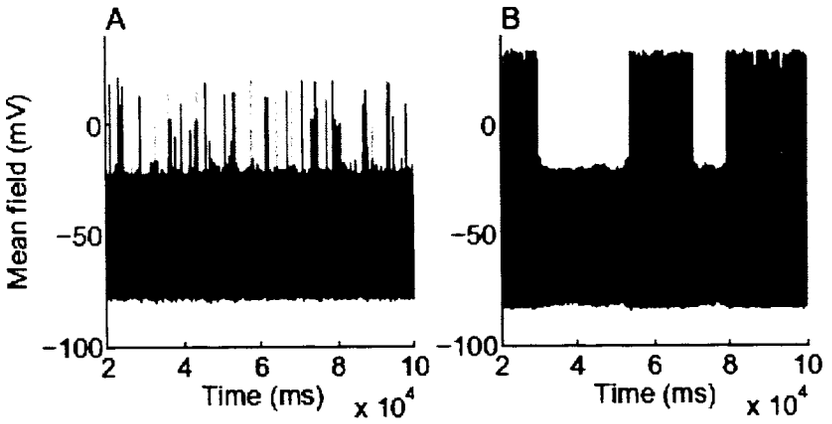

Figure 4.3. Mean field for a pair of coupled neurons. A: $g_K = 26$; B: $g_K = 0$. $D = 1.0 \times 10^{-4}$ in both cases.

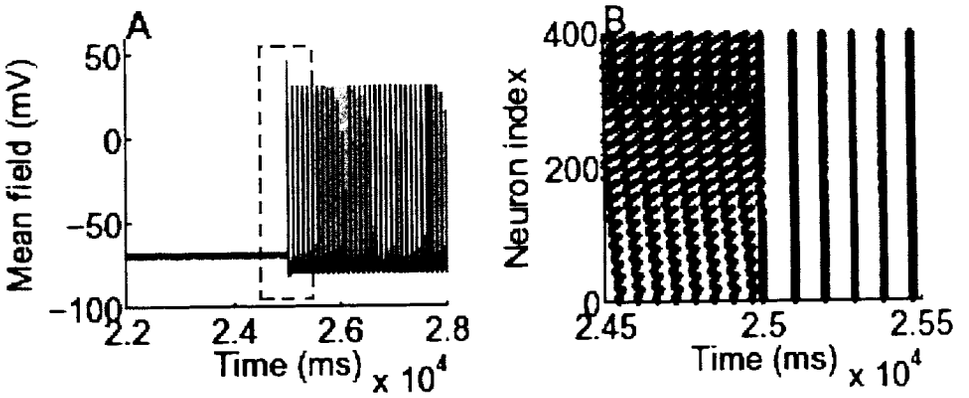

Figure 4.4. Mean field and raster plot of netwwork without noise. A: Mean field of network. B: Raster plot corresponding to the time interval represented by the dashed rectangle in A.

4.3.4. Network with Noise. The effect of noise on the network firing pattern is investigated by adding an independent Gaussian white noise term to each *dV/dt* equation (Figure 4.5). As in the case without noise (Figure 4.4), a dramatic increase of the

amplitude of the mean field was observed by decreasing g_K to 0 (data not shown). With $g_K = 0$, modulations in the amplitude and frequency of the mean field was observed (Figure 4.5A). During the intervals when the mean field amplitude is relatively large, most of the neurons fire in phase (Figure 4.5D).

On the other hand, when the amplitude is relatively small, some groups of neurons fire in phase with each other, but these small sub-populations are often out of phase with other sub-populations Figure 4.5C). This suggests that there are similar noise-induced transitions between "in-phase" and "antiphase" as in the case of two neurons. It is emphasized that both the in-phase, large amplitude activity and the antiphase, low-amplitude activity occur during a simulated "seizure", i.e., when $g_k = 0$.

Clustering is a phenomenon in which multiple populations, each exhibiting in-phase synchronization, but not in phase with each other, emerge from a larger group of oscillators. Clustering has been observed in theoretical studies of coupled oscillators [110] and might play a role in neural systems [111]. To quantify the degree of clustering in the network, the distribution of the phases of all the neurons was measured. The instantaneous phase of the i^{th} neuron was defined as $\phi_i(t) = 2\pi(t - t_{i,n})/(t_{i,n+1} - t_{i,n})$, where $t_{i,n}$ is the n^{th} spike time of the i^{th} neuron and $t_{i,n} \le t \le t_{i,n+1}$ [112]. The measure below was calculated:

$$R_m(t) = \left| \frac{1}{N} \sum_{k=1}^{N} \exp[im\phi_k(t)] \right| \tag{146}$$

which can be used to detect the m-modal distribution of a circular (periodic) variable as follows [113]. For a given time t, a unit vector is assigned for each neuron with the phase $m\phi(t)$ in the Gaussian plane. Then the magnitude of the resultant vector, normalized by the total number of neurons, is represented by $R_m(t)$. For $m = 1$, the magnitude of the resultant vector would be high (close to 1) in the case of in-phase synchronization, whereas, in the case of antiphase clustering, the two populations would form vectors with opposite directions, resulting in a small resultant vector. For $m = 2$, two anti-phase clusters would have vectors in the same direction, leading to a large resultant vector.

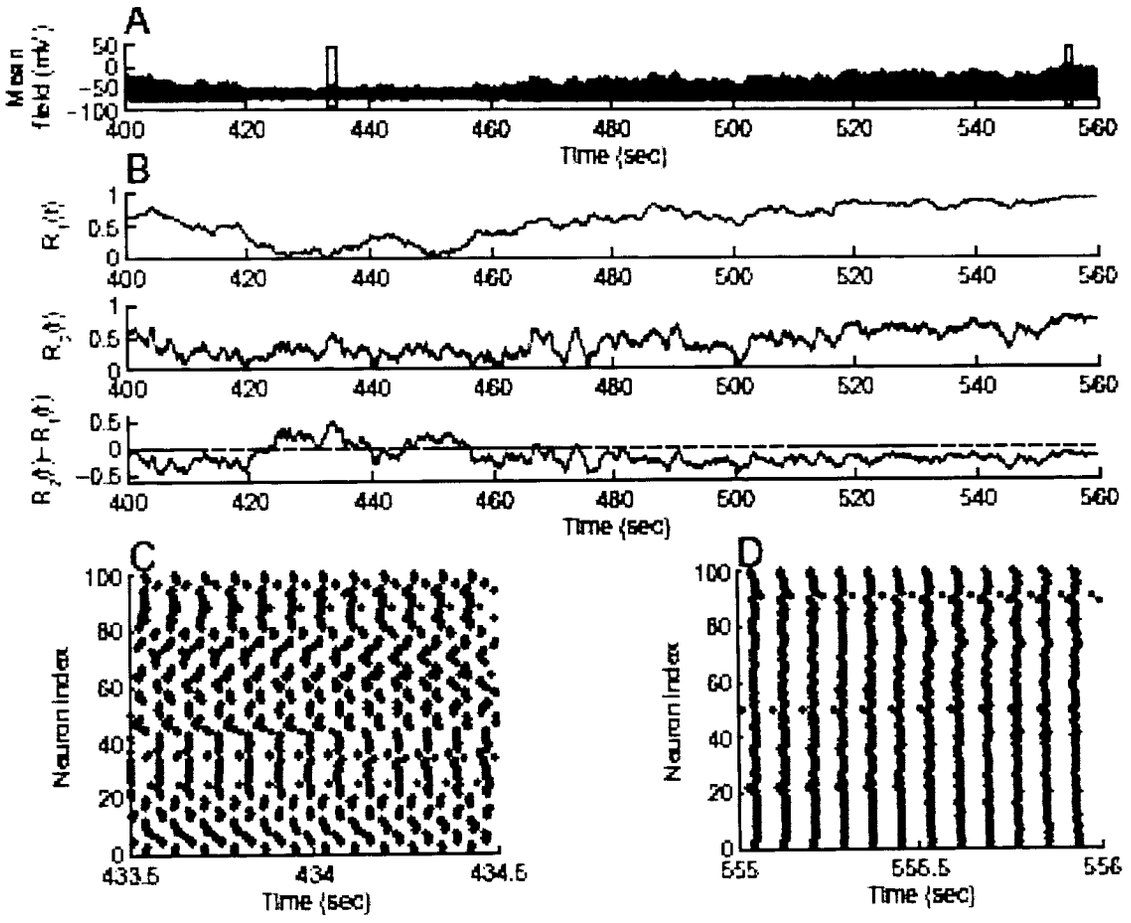

Figure 4.5. Mean field, clustering index, and raster plot of network with noise. A: Mean field of network $D = 5.3 \times 10^{-4}$ with, $g_K = 0$. B: Measures for clustering. Top: R_1, middle: R_2, and bottom: $R_2 - R_1$ as defined in the text. C: Raster plot corresponding to the time interval represented by the left rectangle in A. D: Raster plot corresponding to the time interval represented by the right rectangle in A.

Therefore, a relatively large positive value of $R_2(t)$-$R_1(t)$ is a signature of anti-phase clustering. As shown in the bottom graph of Figure 4.5B, this occurs during the interval of lower-amplitude firing (compare Figure 4.5A, between 420 and 460 seconds, and the raster plot in 5C).

The transitions between mean field firing patterns observed in the network simulation were able to capture the qualitative aspects of transitions observed in local field

potential in 4AP-induced seizures in the rat neocortex (see 1.3.1 for the local field potential 1.2.11.4 for 4AP seizures, and 1.2.9 for the neocortex). The comparison between the network simulation and local field potential recording is shown in Figure 4.6. Figure 4.6A shows such a transition in the simulated mean field from the present network model, in comparison with segments of field potential recording in the rat neocortex in vivo (Figure 4.6B and C), following the focal injection of 4AP [102]. Based on these observations, it is suggested that neural activity during 4AP-induced seizures may be caused by a bifurcation in the stable phase difference between neurons. Furthermore, the present results suggest that changes in amplitude and frequency of the field potential, reminiscent of the transitions between so-called spike-and-wave (SW) and low voltage fast activity (LVFA), seen in human patients [100, 101] may be explained by noise-induced transitions among multiple stable states.

4.4. DISCUSSION

4.4.1. Comparison with Previous Studies. Recently, several dynamical system models have been proposed to describe seizure dynamics [103, 104]. Suffczynski *et al.* suggest one possible mechanism of seizure initiation where transitions between bistable states (epileptic and non-epileptic) are caused by noise. (In contrast, the present model relates such transitions to shifts between firing patterns *during* a seizure.) Wendling *et al.* show that various firing patterns of the EEG signal can be produced by tuning the synaptic "coupling strength". These models suggest different mechanisms from ours for the initiation and development of seizure dynamics. However, none of these models need be mutually exclusive. Since seizures can arise via a vast array of biological mechanisms, it is probably reasonable to assume that the underlying dynamical mechanisms of their onset and development can also fill a wide spectrum.

4.4.2. Limitations and Shortcomings of the Present Model. It is important to note that the present model is vastly simplified than the actual neocortex. In this subsection, the limitations and shortcomings of the present model are discussed.

The network built in this study is constructed on a much smaller scale than an actual neocortical network. For example, the number of synaptic connections in the model network is only 4 while, in the real neocortex in rodents, it is of the order of 1,000 (see

1.2.9.4). The total number of neurons is 100 to 200 in the model. Based on the density of neurons in 1.2.9.4 (10^4-10^5 neurons /mm^3), this corresponds to 10^{-3}-10^{-2} mm^3, which is a tiny fraction of the volume in the rat neocortex. A model with a closer scale to an actual neocortical network may change the results dramatically. In the future work, a large scale model (or mean field type model) will be used.

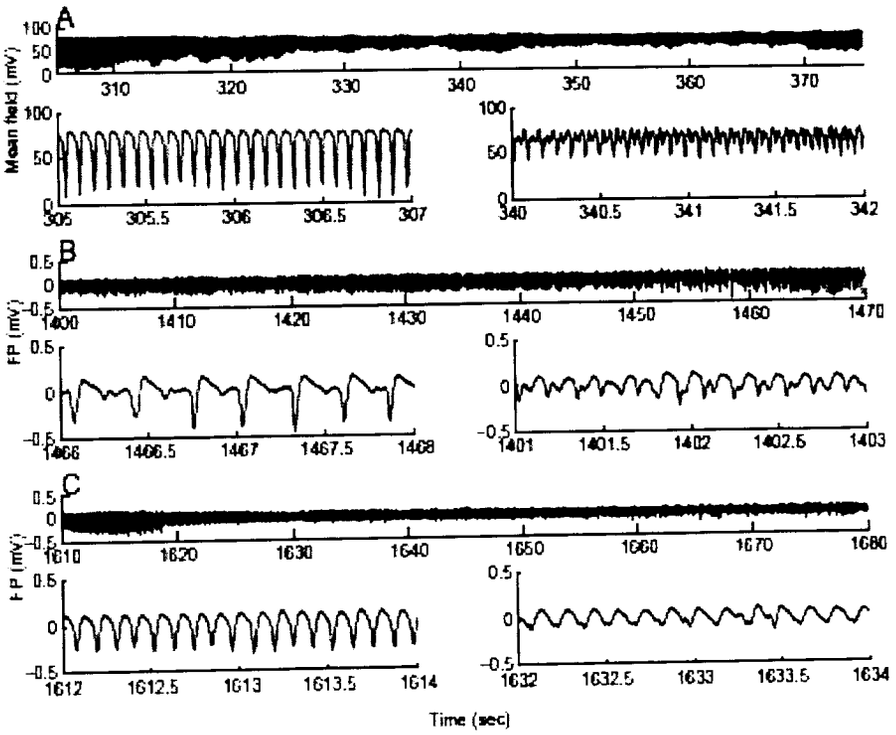

Figure 4.6. Comparison between simulation and experiment. A: Mean field from simulation. Note that the sign is inverted with respect to the previous figures for comparison with extracellular recordings. B, C: Extracellular field potential recordings. The bottom two graphs in each panel (A, B and C) zoom in on intervals within the top graphs, showing examples of high-amplitude field potential spikes (left column), and low-amplitude activity (right column).

All the synaptic connections in the model used here were bidirectional, for a simple coupling scheme allows more direct interpretation of the results. In the neocortex, however, the percentage of unidirectional excitatory synapses outweighs that of

bidirectional excitatory synapses [91, 114, 115]. However, it has been reported that, for a subtype of pyramidal cells in the neocortex, the proportion of bidirectional coupling is much larger than that expected from random network and the synaptic strength is stronger in a pair of neurons with bidirectional synaptic coupling than unidirectional coupling [115]. A further simplification in the present model is that inhibitory neurons were not considered. Although a large percentage of neocortical neurons and synapses are excitatory [19] and disinhibition resulting from the blockage of GABA receptors by drugs such as bicuculline and picrotoxin has been known to cause seizures [116] , the activity of inhibitory neurons has been shown to be important for synchronous neural firing during various seizures induced by other drugs, including 4-AP [117] . A critical next step will be to add inhibitory neurons to the present model.

The increase of extracellular potassium concentration has been observed during epileptiform activity [11]. Several modeling studies predict that the increase of extracellular potassium concentration can play a role in transitions and synchronization in epileptic activity [118, 119]. In the present model, however, the changes in the concentration of extracellular potassium were not taken into account, again in order to develop a preliminary, simplified model. Besides those omissions mentioned above, other complex effects, like the role of astrocytes and long-range neocortical connections, will be addressed in future expansions of the current model.

4.5. CONCLUSION

The present study proposes a possible dynamical mechanism for seizure initiation as a bifurcation, and suggests that experimentally observed changes in field potential amplitude and frequency during the course of a seizure may be explained by noise-induced transitions among multistable states. Despite its lmitations and shortcomings, the synaptically-connected excitatory network model presented here provides testable hypotheses of bifurcation and noise-induced transitions as the mechanisms underlying key elements of neocortical seizure dynamics.

5. STOCHASTIC ANALYSIS OF LIMIT CYCLE OSCILLATOR

5.1. OBJECTIVES

In this section, theoretical aspects of a limit cycle under stochastic perturbation are studied. The ultimate goal of the project is to develop a practical numerical method to reduce a system with a stable limit cycle to normal form, which would be applied to the study of synchronization of coupled oscillators.

In 5.2, the original motivation for the project, which is to study the effect of stochastic dynamics of ion channels on the statistics of the firing period in a neuron model, is stated. A two-state continuous time Markov chain model for ion channel dynamics will be approximated by stochastic differential equations which consist of deterministic neural models with multiplicative (state-dependent) noise. Therefore, the study is converted into the study of a limit cycle under stochastic perturbation. Below, the approach taken to this problem is outlined (see also Figure 5.1).

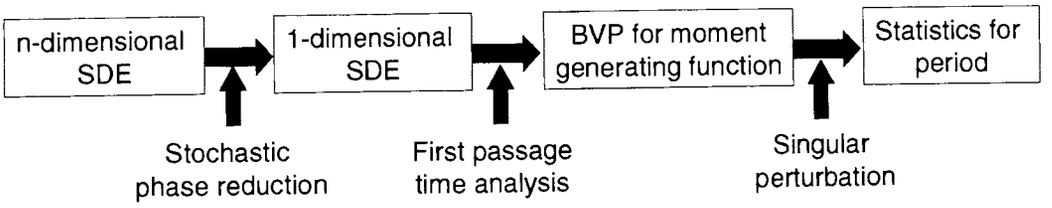

Figure 5.1. Diagram of the approach taken.

In 5.3, a stochastic version of phase reduction is discussed (see 1.5.4 for phase reduction). It turns out that the second derivative of the phase function is necessary even for the lowest approximation, which motivated the study in the next subsection.

In 5.4, a numerical method is developed to obtain partial derivatives of any order of the phase function for a stable limit cycle, which is necessary for higher order phase reduction. In particular, the second order partial derivatives can be applied to stochastic perturbation of a limit cycle.

In 5.5, a framework to obtain the moments of the period of a limit cycle under stochastic perturbation is developed by solving the boundary value problem for the moment-generating function of the first passage time problem.

The development of the numerical method described in 5.4 has been submitted and uploaded on ArXiv.org [4].

5.2. MOTIVATION: STOCHASTIC NEURAL MODEL

Consider the Morris-Lecar oscillator (see 1.4.6). The equations are repeated below:

$$C\frac{dV}{dt} = -g_{Ca}m_{\infty}(V)(V-V_{Ca}) - g_K w(V-V_K) - g_L(V-V_L) + I_{app} \tag{147}$$

$$\frac{dw}{dt} = \frac{\phi(w_{\infty}(V)-w)}{\tau} \tag{148}$$

where V and w represent the membrane potential and the fraction of open potassium channels, respectively. A stochastic version of Eq. 148 is constructed below (see 1.4.2 for a deterministic case). Start from a two-state Markov process (see 1.6.9) for a model of a single ion channel:

$$C \rightleftharpoons O, \tag{149}$$

where C and O represent the closed and open state, respectively. Let $k_O(V)$ and $k_C(V)$ be the reaction rates for the formation of the open and closed states, respectively. Then, by the property of Markov chain [120]:

$$\#\{Close\ to\ Open\ in[t,t+\Delta t)\} = P((N-N_O(t))k_O(V)\Delta t) \tag{150}$$

$$\#\{Open\ to\ Close\ in[t,t+\Delta t)\} = P(N_O(t)k_C(V)\Delta t), \tag{151}$$

where $N_O(t)$ is the number of open channels at time t and $P(\lambda)$ is a Poisson random variable with mean λ. For a large number of channels, $P(\lambda)$ can be approximated by a Gaussian random variable with mean and variance λ:

$$P(\lambda) \approx \lambda + \sqrt{\lambda} Z(0,1), \tag{152}$$

where $Z(0,1)$ is a Gaussian random variable with mean and variance 1. Then,

$$\begin{aligned} N_O(t+\Delta t) - N_O(t) &= (N - N_O(t))k_O(V)\Delta t - N_O(t)k_C(V)\Delta t \\ &\quad + \sqrt{(N - N_O(t))k_O(V)\Delta t}Z_1 - \sqrt{N_O(t)k_C\Delta t}Z_2 \\ &= \{(N - N_O(t))k_O(V) - N_O(t)k_C(V)\}\Delta t \\ &\quad + \sqrt{\{(N - N_O(t))k_O(V) + N_O(t)k_C\}\Delta t}Z. \end{aligned} \tag{153}$$

By dividing both sides by the total number of channels N, the stochastic equation for w can be obtained as follows:

$$dw = \{(1-w)k_O - wk_C\}\Delta t + \sqrt{\frac{(1-w(t))k_O(V) + w(t)k_C}{N}}dW, \tag{154}$$

where W is a Wiener process (see 1.7 for how this equation should be interpreted). Note that, by taking the limit of $N \to \infty$ and following the process discussed in 1.4.2, Eq. 154 takes the same form as Eq. 148.

5.3. STOCHASTIC PHASE REDUCTION

The stochastic differential equation of the following form is studied:

$$\dot{X} = F(X) + G(X)\xi(t), \tag{155}$$

where $X \in \Re^N$ and $\xi(t)$ is a Gaussian white noise term such that $\langle \xi(t) \rangle = 0$ and $\langle \xi(t)\xi(t') \rangle = 2D\delta(t-t')$ (see 1.7 for background on stochastic differential equations). In

[49], where a stochastic version of phase reduction in the first order is formulated, the authors start from Eq. 155 with the Stratonovich interpretation and obtain the Ito stochastic equation for the phase variable (see 1.5.4 for phase reduction and 1.7.3 for interpretation of the stochastic integral). Additional algebraic manipulation of their phase equation gives

$$\dot{\theta} = 1 + D\sum_{i,j}^{N}\left(\frac{\partial^2\theta}{\partial x_i \partial x_j}G_i + \frac{\partial\theta}{\partial x_i}\frac{\partial G_i}{\partial x_j}\right)G_j + \sum_{i}^{N}\frac{\partial\theta}{\partial x_i}G_i\xi(t), \tag{156}$$

where all the terms on the right hand side above are evaluated on the limit cycle. A comparison of Eq. 156 with the deterministic version of phase reduction discussed in 1.5.4.2 (Eq. 39) shows that, in the stochastic version, the extra terms,

$$D\sum_{i,j}^{N}\left(\frac{\partial^2\theta}{\partial x_i \partial x_j}G_i + \frac{\partial\theta}{\partial x_i}\frac{\partial G_i}{\partial x_j}\right)G_j \tag{157}$$

appear in the deterministic part on the right hand side of Eq. 156. Therefore, even within the framework of first-order phase reduction, the second order partial derivatives have to be obtained for the stochastic version of phase reduction, which motivated the development of a theoretical framework for a numerical algorithm to obtain higher-order partial derivatives of the phase function, explained in the next subsection.

It is worth commenting on the choice of the interpretation of SDEs, Eqs. 155 and 156 (see 1.7.5 for some discussions about the choice of Ito and Stratonovich interpretations). The Stratonovich interpretation is preferred in Eq. 155 for the change of variables from $\Re^n$ to the phase variable, since the rules of ordinary calculus hold for the Stratonovich interpretation. On the other hand, the Ito interpretation is preferred in Eq. 156 since this equation will be used for the first passage time analysis in 5.5, with which the Ito interpretation is consistent.

5.4. HIGER ORDER APPROXIMATION OF ISOCHRONS

One limitation of the method for phase reduction described in 1.5.4.1 is that it is only valid to first order. To develop higher order phase reduction, it is necessary to obtain higher order partial derivatives of θ. In addition, as discussed in the previous subsection, to obtain the second order partial derivatives of θ is necessary even for the lowest-order stochastic phase reduction (Eq. 156). However, to the best of our knowledge, an approach to higher order approximations of θ similar in spirit to the one due to Malkin (see Eq. 40 in 1.5.4.2) for finding the gradient of θ has not been described so far in the literature.

In this subsection, a theoretical basis is developed for a numerical algorithm to obtain partial derivatives of the phase function to arbitrary order. Only the outline of the method is provided. The full mathematical detail of the method is in [4]. In 5.4.1, some notions from differential geometry are explained since the result can be described in a more compact way with those notions. The main result is stated in 5.4.2. An example of the application of the result is given in 5.4.3. The reader interested in applications may jump directly to 5.4.3 and use the preceding subsections as references.

5.4.1. Some Definitions and Notations. Let $v=(v_1,\ldots,v_n)$ be any vector in $\Re^n$ and f any differentiable real-valued function in $x_1,\ldots,x_n$. Given a multi-index $J=(j_1,\ldots,j_n)$, i.e., an n-dimensional vector with non-negative integer entries, write $v^J=v_{j_1}\ldots v_{j_n}$ and $f_J=D^Jf=D_1^{j_1}\ldots D_n^{j_n}f$, where D_i denotes the partial derivative with respect to x_i and $D_i^k=D_i\ldots D_i$ (k times). Let $f^{(k)}$ represent the symmetric k-multilinear map on $\Re^n$ characterized (via polarization of polynomial maps) by

$$f^{(k)}(v,\ldots,v)=\sum_{|J|=k}f_Jv^J \tag{158}$$

for all $v\in\Re^n$. The sum is over all multi-indices J of order $|J|=j_1+\ldots+j_n=k$. Here, and often later, reference to the point x, where the derivatives are taken, is omitted. When necessary, this point is indicated as a sub-index; thus $f_x^{(2)}(v,w)$ is the bilinear map

evaluated at the vectors v, w regarded as tangent vectors at $x \in \mathbb{R}^n$, where x is the point where the partial derivatives of f are calculated.

Now define

$$Q_t^{(k)} = \Theta^{(k)}_{\phi_t(x)}, \tag{159}$$

for some fixed $x \in \Re^n$, where ϕ_t is the flow of F. $F^{(k)}$ is defined similarly, which is now a vector-valued, symmetric, k-multilinear map. (A convenient alternative description of $\Theta^{(k)}$ and $F^{(k)}$, and more generally of the higher order derivative forms associated with tensor fields, will be given below.) In particular, $F^{(1)}$ is the linear map which for $v \in \Re^n$ gives the directional derivative of F along v, i.e., $F^{(1)}(v) = D_v F = \sum_j v_j D_j F$, where $D_v F$ is defined by this identity.

Another general concept needed below is the *symmetric composition* of multilinear maps, which is defined as follows. Let Q by a symmetric s-multilinear map on $\Re^n$ taking values in $\Re$, and H a symmetric k-multilinear map on $\Re^n$ taking values in $\Re^n$. Then the symmetric composition of Q and H is the symmetric $s+k-1$-multilinear map on $\Re^n$, denoted $Q \bullet H$ and given by

$$Q \bullet H(v_1, \ldots, v_{s+k-1}) = \frac{1}{(s+k-1)!} \sum_{\sigma \in S_{s+k-1}} Q(H(v_{\sigma(1)}, \ldots, v_{\sigma(k)}), v_{\sigma(k+1)}, \ldots, v_{\sigma(s+k-1)}) \tag{160}$$

where the sum is over all permutations of the set $\{1,2,\ldots,s+k-1\}$. Finally, given a co-vector Q on $\Re^n$ (a linear map from $\Re^n$ to $\Re$), the k-multilinear map is defined as

$$(Q \otimes \cdots \otimes Q)(v_1, \ldots, v_k) = Q(v_1) \ldots Q(v_k) (\text{the } k - \text{fold tensor product.}) \tag{161}$$

5.4.2. The Main Results. The theoretical basis for the numerical algorithm to obtain partial derivatives is summarized as the theorem below. The proof is given in [4] and is not repeated in this dissertation. In 5.4.3, the use of the theorem with the Stuart-Landau oscillator is illustrated.

Theorem: Let $x \in \mathrm{C}$, $x(t) = \phi_t(x)$, $k \geq 1$, and $Q_t^{(k)}$ the k-multilinear map defined in Eq. 161. Then, the following hold.

1. $Q_t^{(k)}$ satisfies the differential equation in $A_t^{(k)}$ given by

$$\dot{A}_t^{(k)} + kA_t^{(k)} \bullet F_{x(t)}^{(1)} = -\sum_{l=1}^{k-1} \binom{k}{l+1} Q_t^{(k-l)} \bullet F_{x(t)}^{(l+1)}, \tag{162}$$

where the right-hand side contains the $Q_t^{(j)}$ for $j < k$, and equals 0 if $k = 1$.

2. Let A be any k-multilinear map, N a positive integer, and $A_{t,N}$ the solution to Eq. 162 for $0 \leq t \leq NT$ such that $A_{NT,N} = A$. Then there exists a T-periodic solution A_t such that $A_{t,N}$ converges exponentially to A_t for $0 \leq t \leq T$ as $N \to \infty$. More precisely, there are constants $C > 0$ and $0 < \lambda < 1$ so that

$$\sup_{0 \leq t \leq T} | A_{t,N} - A_t | \leq C\lambda^N. \tag{163}$$

3. If $A_t^{(k)}$ is any T-periodic solution of Eq. 162, then

$$Q_t^{(k)} = A_t^{(k)} + \mu Q_t^{(1)} \otimes \cdots \otimes Q_t^{(1)} \tag{164}$$

where $\mu = T^k [Q_0^{(k)}(F_x, \ldots, F_x) - A_0^{(k)}(F_x, \ldots, F_x)]$.

4. The term $Q_0^{(k)}(F_x, \ldots, F_x)$ has an ***a priori*** expansion as a linear combination of compositions of the lower order terms $Q_0^{(l)}$ and $F_x^{(l)}$ for $l \leq k-1$. This expansion is described in section 2.5 in [4].

The equation for the standard (Malkin's) method of phase reduction for obtaining the gradient of Θ is the equation in part 1 of the theorem when $k = 1$:

$$\dot{Q}_t^{(1)} + Q_t^{(1)} \circ F_{x(t)}^{(1)} = 0. \tag{165}$$

Furthermore, $Q_t^{(1)}$ is the unique periodic solution such that $Q_0^{(1)}(F_x) = 1/T$. This unique solution can be found numerically, according to part 2, by the following procedure: Let a covector A (i.e., a linear map from $\Re^n$ to $\Re$) at p be a choice of initial condition for Eq. 165 which is arbitrary except for the normalization $A(F_p) = 1/T$. One then integrates Eq. 165 for $t < 0$ (backward integration) until the solution stabilizes to a periodic (co)-vector-valued function on the limit cycle. Stabilization is assured to happen for sufficiently large $|t|$. This periodic function is the solution desired in order one. The general order case is then given recursively by the successive applications of the theorem.

5.4.3. The Stuart-Landau Oscillator: an Illustration. To illustrate the method, the case $k = 2$ is considered. From the general definition of symmetric composition introduced in Eq. 160, $Q_t^{(2)} \bullet F^{(1)}$ and $Q_t^{(1)} \bullet F^{(2)}$ are given by

$$Q_t^{(2)} \bullet F^{(1)}(v_1, v_2) = \frac{1}{2}\left(Q_t^{(2)}(F^{(1)}(v_1), v_2) + Q_t^{(2)}(F^{(1)}(v_2), v_1)\right) \tag{166}$$

$$Q_t^{(1)} \bullet F^{(2)}(v_1, v_2) = Q_t^{(1)}(F^{(2)}(v_1, v_2)). \tag{167}$$

Suppose that $Q_t^{(1)}$ has already been obtained (say, by the standard method) and wish to find $Q_t^{(2)}$. According to the main theorem, this second order term satisfies the non-homogeneous differential equation

$$\dot{Q}_t^{(2)} + 2Q_t^{(2)} \bullet F^{(1)} = -Q_t^{(1)} \bullet F^{(2)}, \tag{168}$$

where the $F^{(j)}$ are evaluated at $x(t)$ on the limit cycle. The equation can be solved as follows: Let $A_t^{(2)}$ be a solution to Eq. 168 obtained by backward integration for an arbitrary initial condition. For large enough $|t|$ this solution stabilizes to a periodic (tensor-valued) function along the limit cycle, which is still denoted by $A_t^{(2)}$. Then, by item 3 of Theorem 1.1,

$$Q_t^{(2)} = A_t^{(2)} + T^2\left(Q_0^{(2)}(F_x, F_x) - A_0^{(2)}(F_x, F_x)\right)Q_t^{(1)} \otimes Q_t^{(1)} \tag{169}$$

where $Q_t^{(1)} \otimes Q^{(1)}(v_1, v_2) = Q_t^{(1)}(v_1)Q_t^{(1)}(v_2)$. It is shown in the section 2.5 in [4] that the expansion referred to in item 4 of the theorem amounts in this case to $Q_0^{(2)}(F_x, F_x) = -Q_0^{(1)}(F_x^{(1)}(F_x))$. Therefore,

$$Q_t^{(2)} = A_t^{(2)} - T^2\left(Q_0^{(1)}(F^{(1)}(F_x)) + A_0^{(2)}(F_x, F_x)\right)Q_t^{(1)} \otimes Q_t^{(1)} \tag{170}$$

is the desired solution.

Recall the Stuart-Landau oscillator (see 1.5.4.1). Define

$$A_a = \begin{bmatrix} 1 & -a \\ a & 1 \end{bmatrix}. \tag{171}$$

Regard points of $\Re^2$ as column vectors: $x = (x_1, x_2)^\dagger$, where $\dagger$ indicates the transpose operator. Let a, b be real constants and $\rho(r)$ a smooth function of $r > 0$ such that $\rho(1) = 1$ and $\rho'(1) = \chi > 0$. Now define a vector field on $\Re^2$ by

$$F(x) = A_a x - \rho(|x|)A_b x. \tag{172}$$

Then it is easy to check that the differential equation $\dot{x} = F(x)$ has a hyperbolic stable limit cycle given by $S^1 = \{x \in \Re^2 : |x| = 1\}$. In fact, $r = |x|$ satisfies:

$$\dot{r} = r(1-\rho(r)) = -\chi(r-1) + o(r-1), \tag{173}$$

showing that the limit cycle is approached for $t > 0$ with Lyapunov exponent $-\chi$. In the special case of $\rho(r) = r^2$, then $\dot{r} = r(1-r^2)$ is easily solved:

$$r(t) = \left(1 + \frac{1-r_0^2}{r_0^2} e^{-2t}\right)^{-\frac{1}{2}}, \tag{174}$$

where $r_0 = r(0)$. With the coordinate change $x_1 = \cos(\varphi + b \ln r)$ and $x_2 = \sin(\varphi + b \ln r)$, one can write the solution to $\dot{x} = F(x)$ explicitly in the new variables r, φ by setting

$$\varphi(t) = \varphi_0 + (a-b)t, \tag{175}$$

as can be easily checked. Therefore, $\Theta(x) = \varphi/2\pi$ modulo integer translations. For this example, one can calculate the derivatives of $\Theta(x)$ explicitly, and then compare them with the numerical values derived from Theorem 1.1.

Implicit differentiation gives the first and second order derivatives of Θ along the limit cycle. Write $\Theta_i = D_i\Theta$, $\Theta_{ij} = D_iD_j\Theta$, where D_i is the partial derivative in x_i. Then

$$\Theta^{(1)} = (\Theta_1, \Theta_2) = \left(-\frac{bx_1 + x_2}{2\pi |x|^2}, \frac{x_1 - bx_2}{2\pi |x|^2}\right). \tag{176}$$

Identifying $\Theta^{(2)}$ with the Hessian of Θ, one can write

$$\Theta^{(2)} = \begin{bmatrix} \Theta_{11} & \Theta_{12} \\ \Theta_{21} & \Theta_{22} \end{bmatrix} = \begin{bmatrix} \dfrac{2x_1x_2 - b(x_2^2 - x_1^2)}{2\pi |x|^4} & \dfrac{2bx_1x_2 + x_2^2 - x_1^2}{2\pi |x|^4} \\ \dfrac{2bx_1x_2 + x_2^2 - x_1^2}{2\pi |x|^4} & -\dfrac{2x_1x_2 - b(x_2^2 - x_1^2)}{2\pi |x|^4} \end{bmatrix}. \tag{177}$$

The tensors $Q_t^{(1)}$ and $Q_t^{(2)}$ are similarly written. Let $\zeta(t) = \varphi_0 + (a-b)t + b\ln r(t)$. Then

$$Q_t^{(1)} = (Q_1(t), Q_2(t)) = \left(\frac{\sin\zeta(t)}{2\pi r(t)}, \frac{\cos\zeta(t)}{2\pi r(t)} \right) \tag{178}$$

and

$$Q_t^{(2)} = \begin{bmatrix} Q_{11}(t) & Q_{12}(t) \\ Q_{21}(t) & Q_{22}(t) \end{bmatrix} = \begin{bmatrix} \dfrac{b\cos(2\zeta(t)) + \sin(2\zeta(t))}{2\pi r^2(t)} & \dfrac{-\cos(2\zeta(t)) + b\sin(2\zeta(t))}{2\pi r^2(t)} \\ \dfrac{-\cos(2\zeta(t)) + b\sin(2\zeta(t))}{2\pi r^2(t)} & -\dfrac{b\cos(2\zeta(t)) + \sin(2\zeta(t))}{2\pi r^2(t)} \end{bmatrix}. \tag{179}$$

For any vectors $v, v_1, v_2 \in \Re^2$,

$$F = A_a x - |x|^2 A_b x \tag{180}$$

$$F^{(1)}(v) = A_a v - 2x \cdot v A_b x - |x|^2 A_b v \tag{181}$$

$$F^{(2)}(v_1, v_2) = -2x \cdot v_1 A_b v_2 - 2x \cdot v_2 A_b v_1 - 2v_1 \cdot v_2 A_b x. \tag{182}$$

Let the components of these tensors relative to the standard basis e_1, e_2 of $\Re^2$ be denoted as follows:

$$F_x = \begin{bmatrix} F^1(x) \\ F^2(x) \end{bmatrix}, \quad F_x^{(1)}(e_i) = \begin{bmatrix} F_i^1(x) \\ F_i^2(x) \end{bmatrix}, \quad F_x(e_i, e_j) = \begin{bmatrix} F_{ij}^1(x) \\ F_{ij}^2(x) \end{bmatrix}, \tag{183}$$

where the entries are obtained from Eqs. 180, 181, and 182. For example, from Eq. 182, it follows that $F_{21}^2(x) = F_{12}^2(x) = e_2 \cdot F^{(2)}(e_1, e_2) = -2(x_1 + bx_2)$. The other entries are:

$$\begin{bmatrix} F_1^1(x) & F_2^1(x) \\ F_1^2(x) & F_2^2(x) \end{bmatrix} = \begin{bmatrix} 1-2x_1(x_1-bx_2)-|x|^2 & -b-2x_2(x_1-bx_2)+b|x|^2 \\ b-2x_1(bx_1+x_2)-b|x|^2 & 1-2x_2(bx_1+x_2)-|x|^2 \end{bmatrix} \tag{184}$$

$$\begin{bmatrix} F_{11}^1(x) & F_{12}^1(x) \\ F_{21}^1(x) & F_{22}^1(x) \end{bmatrix} = \begin{bmatrix} -6x_1+2bx_2 & 2bx_1-2x_2 \\ 2bx_1-2x_2 & -2x_1+6bx_2 \end{bmatrix} \tag{185}$$

$$\begin{bmatrix} F_{11}^2(x) & F_{12}^2(x) \\ F_{21}^2(x) & F_{22}^2(x) \end{bmatrix} = \begin{bmatrix} -6bx_1-2x_2 & -2x_1-2bx_2 \\ -2x_1-2bx_2 & -2bx_1-6x_2 \end{bmatrix} \tag{186}$$

The differential equations for Q_i and Q_{ij} (Eqs. 165 and 168; all summations are over $s=1,2$) can be written as:

$$\dot{Q}_i = \sum_s Q_s F_i^s \tag{187}$$

$$\dot{Q}_{ij} = \sum_s (F_i^s Q_{sj} + F_j^s Q_{si}) - \sum_s Q_s F_{ij}^s . \tag{188}$$

The first equation is the one used in Malkin's standard approach. Once it is solved by the already indicated procedure, its solution enters as the non-homogeneous term for the second equation.

The result of the numerical calculation is shown in Figure 5.2. The initial condition for $A_{t,NT}$ was chosen from a set of random numbers and numerical integration of Eq. 168 was done backward in time (data not shown). Then, $Q_t^{(2)}$ was obtained using Eq. 170 (solid line in Figure 5.2). Convergence of $Q_t^{(2)}$, obtained numerically, to the analytical solution (dashed line in Figure 5.2) is clearly observed.

5.5. DETERMINATION OF MOMENTS OF PERIOD

5.5.1. First Passage Time Analysis. To determine the statistics for the period of a limit cycle, the differential equation for the phase (Eq. 156) will be used. A framework to determine the moments of the first passage time (see 1.7.7) is applied to this problem.

Eq. 156 can be written in a more general form as follows:

$$\dot{\theta} = a + Df(\theta) + \sqrt{2D}g(\theta)\xi \tag{189}$$

where D is "small". The problem of interest is, for the system described by Eq. 189, to obtain the moments of the first passage time through a boundary starting from the initial point θ. In particular, the period of an oscillation in the original limit cycle is assumed to be the first passage time through $\theta = T$ starting from $\theta = 0$. The moment generating function $u(s,\theta)$ of the first passage time starting at θ is defined as

$$u(s,\theta) = \int_0^\infty e^{-st} p(t,\theta)dt, \tag{190}$$

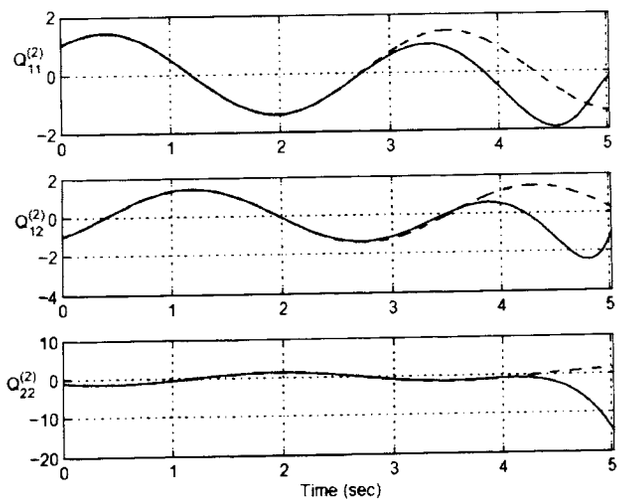

Figure 5.2: Determination of $Q_t^{(2)}$ for the Stuart-Landau oscillator. $a = 2, b = 1$. Each component of the tensors is plotted as a function of time. Numerical integration is done backward in time using the Euler method with $dt = 10^{-3}$. Solid line: $Q_t^{(2)}$ determined from $A_{t,NT}$; dashed line: $Q_t^{(2)}$ found analytically. To clearly show convergence of the numerically obtained $Q_t^{(2)}$ to the analytical solution, $A_{t,NT}$ was not plotted and the period of the simulation was set at only $0.8T$.

where $p(t,\theta)$ is the probability density for the first passage time starting from θ (see 1.6.7 for the moment generating function). It is known that $u(s,\theta)$ satisfies

$$Dg(\theta)^2 u'' + (a + Df(\theta))u' - su = 0, \tag{191}$$

where $u' = \partial u / \partial \theta$ [121]. Since Eq. 191 is a second order differential equation, two boundary conditions are necessary, although the first passage time of interest is the one through only one point. To handle this issue, two absorbing boundaries are set at two points, $\theta = \pm T$. This corresponds to the boundary values $u(\pm\theta) = 1$. The crucial two assumptions made here are that the drift term (= a) in Eq. 189 is large enough compared to the diffusion term ($= \sqrt{2D}g(\theta)$) and that the left boundary ($\theta = -T$) is "far away" from the starting point, so that it is unlikely to reach the left boundary. This justifies the application of the outer solution in boundary layer theory (see 1.5.6 for boundary layer theory and 1.7.7 for the application of the outer solution in a first passage time problem). Then, the n^{th} order moment of the first passage time T_{fp} can be determined by

$$E\left[T_{fp}^n\right] = (-1)^n \left.\frac{\partial^n u}{\partial s^n}\right|_{s=0}. \tag{192}$$

To solve Eq. 191, if $g(\theta) \neq 0$ for all θ, one can solve the linear equation

$$u_{\theta\theta} + \frac{(a + Df(\theta))u_\theta}{Dg(\theta)^2} - \frac{su}{Dg(\theta)^2} = 0. \tag{193}$$

However, since $g(\theta)$ can be 0 for some θ, which would bring discontinuity in Eq. 193, there is an issue with solving Eq. 191. Although the existence and uniqueness are unsolved issues, the attempt here is to obtain an approximate solution to this equation by applying regular perturbation to the outer solution of boundary layer theory.

Assume u can be written in the following form:

$$u(\theta) = u_0(\theta) + Du_1(\theta) + D^2 u_2(\theta) + \cdots \tag{194}$$

Substituting into Eq. 191,

$$\begin{aligned} &Dg(\theta)^2(u_0''(\theta) + Du_1''(\theta) + D^2u_2''(\theta) + \cdots) + (a + Df(\theta))(u_0'(\theta) + Du_1'(\theta) + D^2u_2'(\theta) + \cdots) \\ &- s(u_0(\theta) + Du_1(\theta) + D^2u_2(\theta) + \cdots) = 0 \end{aligned} \tag{195}$$

Equate the coefficients of powers of D to be zero to obtain

$$\begin{aligned} &D^0 : au_0' - su_0 = 0 \\ &D^1 : au_1' - su_1 + g^2(\theta)u_0'' + f(\theta)u_0' = 0 \\ &\quad\vdots \end{aligned} \tag{196}$$

By the boundary conditions $u(\pm T) = 1$,

$$\begin{aligned} &u_0(-T) = u_0(T) = 1 \\ &u_1(-T) = u_1(T) = 0 \\ &\quad\vdots \end{aligned} \tag{197}$$

Tedious but straightforward calculation gives the solutions for Eq. 196

$$\begin{aligned} u_0(\theta) &= \exp\left(\frac{s(\theta - T)}{a}\right) \\ u_1(\theta) &= \frac{1}{a}\exp\left(\frac{s(\theta - T)}{a}\right)\left[\left(\frac{s}{a}\right)^2 \int_x^T g^2(\theta)d\theta + \left(\frac{s}{a}\right)\int_x^T f(\theta)d\theta\right] \end{aligned} \tag{198}$$

Therefore, u can be written as

$$u(\theta) = \exp\left(\frac{s(\theta - T)}{a}\right) + \frac{D}{a}\exp\left(\frac{s(\theta - T)}{a}\right)\left[\left(\frac{s}{a}\right)^2 \int_x^T g^2(\theta)d\theta + \left(\frac{s}{a}\right)\int_x^T f(\theta)d\theta\right] + O(D^2) \tag{199}$$

Using Eq. 192, the first and second moments for the first passage time can be obtained as follows:

$$E[T_{fp}] = \frac{T-\theta}{a} - \frac{D}{a^2}\int_\theta^T f(\theta')d\theta' + O(D^2), \tag{200}$$

$$E[T_{fp}^2] = \left(\frac{T-\theta}{a}\right)^2 - \frac{2D}{a^3}\left[(T-\theta)\int_\theta^T f(\theta')d\theta' + \int_\theta^T g^2(\theta')d\theta'\right] + O(D^2). \tag{201}$$

The variance for the first passage time is

$$\begin{aligned} Var[T_{fp}] &= E[T_{fp}^2] - E[T_{fp}]^2 \\ &= \frac{2D}{a^3}\int_\theta^T g^2(\theta')d\theta' + O(D^2). \end{aligned} \tag{202}$$

5.5.2. Numerical Results. To study the validity of the approximation by the outer solution, the first passage time of a one-dimensional SDE is numerically obtained for a comparison. Let x_0 be the position of a particle at t=0. Assume that the position of the particle at t is determined by the following SDE:

$$\dot{x} = a + D\cos^2 2\pi x + \sqrt{2D}\cos(4\pi x)\xi(t) \tag{203}$$

Two absorbing boundary B_L and B_R are set such that $B_L \le x_0 \le B_R$. To obtain one realization, Eq. 203 is numerically integrated with the Euler method and the time required for x to pass either one of the two boundaries is obtained. 100,000 realizations are simulated to obtain the moments for the first passage time.

The mean first passage time from the outer solution (Eq. 200) and that from the numerical integration of Eq. 203 results are shown in Figure 5.3. Although both the 0^{th} and 1^{st} order outer solution have a good agreement with the numerically obtained value, the 1^{st} order solution is closer to the numerically obtained value in the region close to x=0. Figure 5.4 shows the comparison between the variance of the first passage time obtained the two methods above (the one from Eq. 202 and numerically obtained one). Both values are in good agreement. Therefore, these results suggest the validity of the application of the outer solution approximation to the boundary value problem (Eq. 191) for the first passage time problem of the 1-dimensional SDE of the form in Eq. 189.

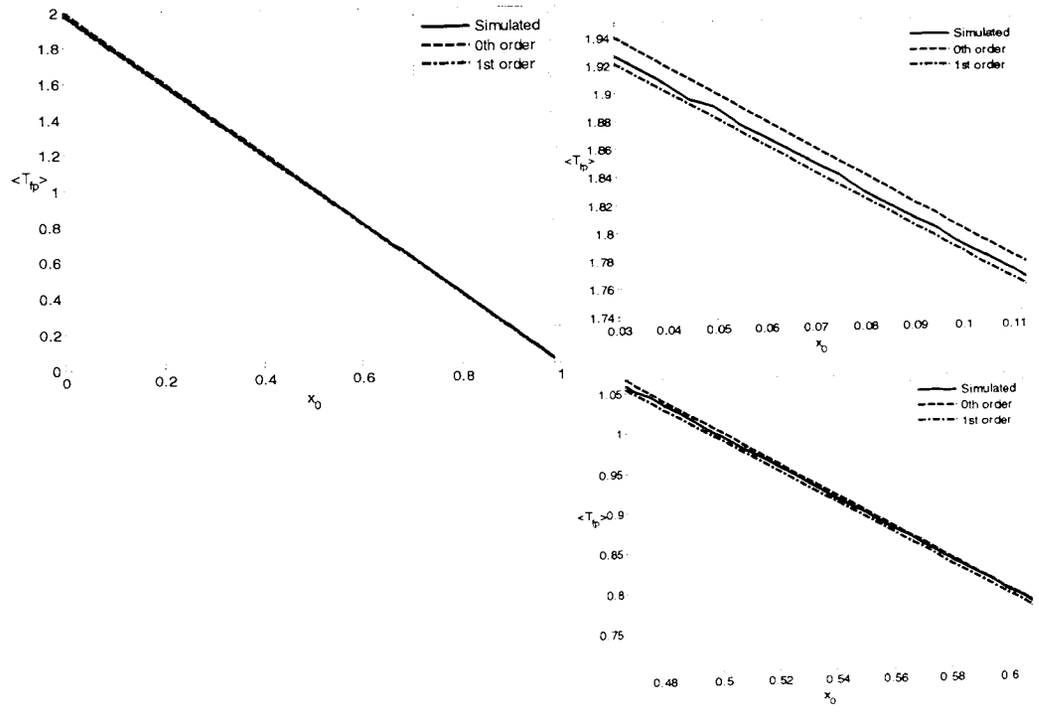

Figure 5.3. $<T_{fp}>$ is plotted as a function of starting point (x_0). a=0.5, D=0.05. Right two figures are blow-ups of the left. The solid, dashed, and dotted-dashed line represent numerical, 0^{th} order, and 1^{st} order solutions, respectively.

5.5.3. Application to a Limit Cycle Oscillator. Since the application of the outer solution in boundary layer theory to the first passage time problem of a one-dimensional SDE is justified in the previous subsection, this subsection discusses how this approach is valid for the determination of the moments of the period of a stable limit cycle oscillator under stochastic perturbations. For this purpose the Stuart-Landau oscillation (see 1.5.4.1) is used since the partial derivatives of the phase variable can be analytically obtained.

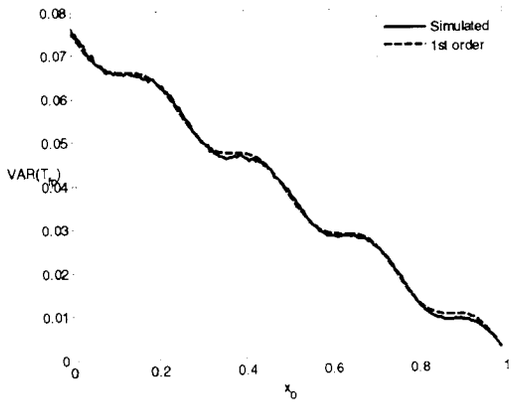

Figure 5.4. VAR(T_{fp}) is plotted as a function of starting point (x_0). a=0.5, D=0.05.

The Stuart-Landau equations (see 1.5.4.1) with multiplicative noise of the following form is considered:

$$\begin{aligned} \dot{x} &= x - c_0 y - (x^2 + y^2)(x - c_2 y) + \sqrt{2D}x\xi(t), \\ \dot{y} &= c_0 x + y - (x^2 + y^2)(c_2 x + y), \end{aligned} \tag{204}$$

where $\xi(t)$ is a Gaussian white noise term with $\langle \xi(t) \rangle = 0$ and $\langle \xi(t)\xi(s) \rangle = \delta(t-s)$. Using Eq. 156, the set of equations can be reduced to

$$\dot{\theta} = 1 + D\left[\frac{\partial^2 \theta}{\partial x^2} x_0(t)^2 + \frac{\partial \theta}{\partial x} x_0(t)\right] + \sqrt{2D}\frac{\partial \theta}{\partial x} x_0(t)\xi(t), \tag{205}$$

where $x_0(t)$ is a point on the limit cycle and all the partial derivatives above are evaluated at $x_0(t)$. Below, for simplicity, the case of the period without noise is 2π (i.e., $|c_0 - c_2| = 1$) is considered (see Eq. 36 in 1.5.4.1 how the two parameters determines the period). From Eqs. 35, 200, and 202, the mean and variance of the period of the limit cycle can be obtained

$$\langle T \rangle = 2\pi - D\int_0^{2\pi}\left(\frac{\partial^2\theta}{\partial x^2}\cos^2\theta + \frac{\partial\theta}{\partial x}\cos\theta\right)d\theta, \tag{206}$$

$$Var(T) = D\int_0^{2\pi}\left(\frac{\partial\theta}{\partial x}\cos\theta\right)^2 d\theta. \tag{207}$$

By the application of the chain rule to Eq. 35, the partial derivatives of θ used above can be obtained:

$$\begin{aligned}\frac{\partial\theta}{\partial x} &= -c_2\cos\theta - \sin\theta,\\ \frac{\partial^2\theta}{\partial x^2} &= c_2\cos 2\theta + \sin 2\theta.\end{aligned} \tag{208}$$

From Eqs. 206, 207, and 208, the mean and variance can be determined analytically:

$$\begin{aligned}\langle T \rangle &= 2\pi + D\frac{\pi c_2}{2}\\ \mathrm{Var}(T) &= D\pi\left(c_2^{\,2} + \frac{(1-c_2)}{4}\right).\end{aligned} \tag{209}$$

From the numerically integrated solution of Eq. 204, the periods of oscillations are determined by thresholding of the y-value of the data. The mean and variance of the period from the numerical integration and analytical calculation are compared in Figure 5.5. In both the mean and variance, the numerical and theoretical results are consistent with each other, except that the variance from the numerical one is twice as large as the theoretical

one at D=0.1. This may improve when the theoretical variance is calculated to higher orders in D.

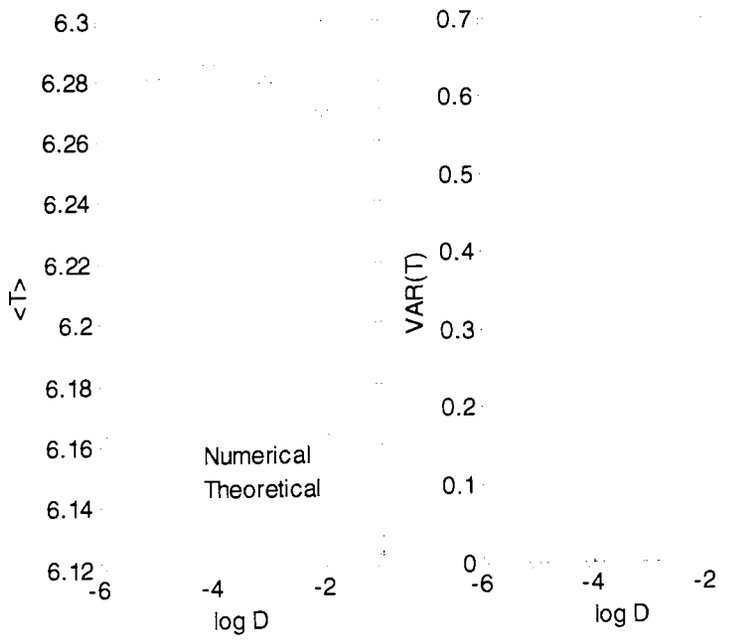

Figure 5.5. A comparison between the numerical and analytical results of the mean (left) and variance (right) of the period of the Stuart-Landau oscillator.

5.6. CONCLUSION

In this section, a theoretical framework to obtain the statistics for the period of a limit cycle oscillator under stochastic perturbation is developed. It is shown that the second partial derivatives of the phase variable are necessary for the stochastic version of phase reduction studied, which is not the case for the deterministic case. A theoretical underpinning to numerically obtain the partial derivatives of the phase variable is developed. Using first passage time analysis, a theoretical framework to determine the moments of the period is obtained. The method obtained is applied to the Stuart-Landau oscillator. The result agrees well the numerical results in the weak noise regime. The method presented here can be applied to any system with a stable limit cycle. If the phase

variable can be analytically obtained, the method gives an analytical result for the moments of the period of the limit cycle oscillator. Otherwise, the partial derivatives of the phase variable can be numerically obtained with the method developed here, and the moments of the period can be obtained by the numerical integration of the obtained partial derivatives.

BIBLIOGRAPHY

[1] Takeshita D, Gale JT, Montgomery EBJ, Bahar S, Moss F. Analyzing spike trains with circular statistics. *Am J Phys* 2009;**77**(5):424-9.

[2] Takeshita D, Tsytsarev V, Bahar S. Spatiotemporal patterns of phase synchronization in voltage-sensitive dye imaging of 4AP-induced epileptic seizures in the rat neocortex (poster). Program No. 250.13, Abstract Viewer/Itinerary Planner, Washington DC, USA: Society for Neuroscience, 2008. Online.

[3] Takeshita D, Sato YD, Bahar S. Transitions between multistable states as a model of epileptic seizure dynamics. *Phys Rev E* 2007;**75**(5 PT 1):051925.

[4] Takeshita D, Feres R. Higher order approximation of isochrons (submitted), arXiv:0910.3890v1.

[5] Nicholls JG, Martin AR, Wallace BG. From Neuron to Brain. Sunderland: Sinauer Associates; 1992.

[6] Kandel ER, Schwartz JH, Jessell TM. Principles of Neural Science. Norwalk: Appleton & Lange; 1991.

[7] Zigmond MJ, Bloom FE, Landis SC, Roberts JL, Squire LR. Fundamental Neuroscience. San Diego: Academic Press 1999

[8] Hille B. Ionic Channels of Excitable Membranes. Sunderland: Sinauer Associates; 1992.

[9] McCormick DA. Membrane potential and action potential. In Fundamental Neuroscience. Zigmoid MJ, Bloom FE, Landis SC, Roberts JL, Squire LR. San Diego: Academic Press 1999, pp129-54.

[10] Cooper GM. The Cell: a Molecular Approach. Sunderland: Sinauer Associates; 2000.

[11] Moody WJ, Futamachi KJ, Prince DA. Extracellular potassium activity during epileptogenesis. *Exp Neurol* 1974;**42**(2):248-63.

[12] Keener J, Sneyd J. Mathematical Physiology. New York: Springer; 1998.

[13] Boyd IA, Martin AR. The end-plate potential in mammalian muscle. *J Physiol* 1956;**132**(1):74-91.

[14] Kress GJ, Mennerick S. Action potential initiation and propagation: upstream influences on neurotransmission. *Neuroscience* 2009;**158**(1):211-22.

[15] Hof PR, Trapp BD, Clauudio L, Colman DR. The cellular components of nervous tissue. In Fundamental Neuroscience. Zigmond MJ, Bloom FE, Landis SC, Roberts JL, Squire LR. San Diego: Academic Press 1999, pp41-70.

[16] Jones EG. Laminar distribution of cortical efferent cells. In Cellular Components of the Cerebral Cortex. Peters A, Jones EG. New York: Plenum 1984:Vol.1, pp521-53.

[17] Connors BW, Gutnick MJ. Intrinsic firing patterns of diverse neocortical neurons. *Trends Neurosci* 1990;**13**(3):99-104.

[18] Steriade M. Neocortical cell classes are flexible entities. *Nat Rev Neurosci* 2004;**5**(2):121-34.

[19] Braitenberg V, Schutz A. Cortex: Statistics and Geometry of Neuronal Connectivity. Cortex: Statistics and Geometry of Neuronal Connectivity. Telos: Springer-Verlag; 1998.

[20] Uhlhaas PJ, Singer W. Neural synchrony in brain disorders: relevance for cognitive dysfunctions and pathophysiology. *Neuron* 2006;**52**(1):155-68.

[21] Rodriguez E, George N, Lachaux JP, Martinerie J, Renault B, Varela FJ. Perception's shadow: long-distance synchronization of human brain activity. *Nature* 1999;**397**(6718):430-3.

[22] Miltner WH, Braun C, Arnold M, Witte H, Taub E. Coherence of gamma-band EEG activity as a basis for associative learning. *Nature* 1999;**397**(6718):434-6.

[23] Golshani P, Goncalves JT, Khoshkhoo S, Mostany R, Smirnakis S, Portera-Cailliau C. Internally mediated developmental desynchronization of neocortical network activity. *J Neurosci* 2009;**29**(35):10890-9.

[24] Nunez PL, Srinivasan R. Electric Fields of the Brain. New York: Oxford University Press; 2006.

[25] Fisher RS, van Emde Boas W, Blume W, Elger C, Genton P, Lee P et al. Epileptic seizures and epilepsy: definitions proposed by the International League Against Epilepsy (ILAE) and the International Bureau for Epilepsy (IBE). *Epilepsia* 2005;**46**(4):470-2.

[26] Wong RK, Traub RD, Miles R. Cellular basis of neuronal synchrony in epilepsy. *Adv Neurol* 1986;**44**:583-92.

[27] Engel JJ, Pedley TA. Epilepsy. New York: Wolters Kluwer; 2008:Vol.1.

[28] Berger T, Borgdorff A, Crochet S, Neubauer FB, Lefort S, Fauvet B et al. Combined voltage and calcium epifluorescence imaging in vitro and in vivo reveals subthreshold and suprathreshold dynamics of mouse barrel cortex. *J Neurophysiol* 2007;**97**(5):3751-62.

[29] Hauser WA, Hesdorffer DC. Epilepsy: Frequency, Causes and Consequences. New York: Demos Publications; 1990.

[30] Pitkanen A, Schwartzkroin PA, Solomon LM. Models of Seizures and Epilepsy. Boston: Elsiver 2006.

[31] Huang X, Troy WC, Yang Q, Ma H, Laing CR, Schiff SJ et al. Spiral waves in disinhibited mammalian neocortex. *J Neurosci* 2004;**24**(44):9897-902.

[32] Hoel PG, Port SC, Stone CJ. Introduction to Probability Theory. New York: Houghton Mifflin Company; 1971.

[33] Schwartz TH, Bonhoeffer T. In vivo optical mapping of epileptic foci and surround inhibition in ferret cerebral cortex. *Nature Medicine* 2001;**7**(9):1063-7.

[34] Leung LS. Field potentials in the central nervous system-recording, analysis, and modeling. In Neurophysiological techniques: application to neural systems. Boulton AA, Baker GB, Vanderwolf CH. Clifton: Humana Press 1990, pp277-312.

[35] Nunez PL. Electric Fields of the Brain. New York: Oxford University Press; 1981.

[36] Civillico EF, Contreras D. Comparison of responses to electrical stimulation and whisker deflection using two different voltage-sensitive dyes in mouse barrel cortex in vivo. *J Membr Biol* 2005;**208**(2):171-82.

[37] Shoham D, Glaser DE, Arieli A, Kenet T, Wijnbergen C, Toledo Y et al. Imaging cortical dynamics at high spatial and temporal resolution with novel blue voltage-sensitive dyes. *Neuron* 1999;**24**(4):791-802.

[38] Dayan P, Abbot LF. Theoretical Neuroscience. Cambridge, Massachusetts: MIT Press; 2001.

[39] Gerstner W, Kistler W. Spiking Neuron Models. New York: Cambridge University Press; 2002.

[40] Connors KA. Chemical Kinetics. New York: VCH Publishers; 1990.

[41] Fall CP, Keizer JE. Voltage gated ionic currents. In Computational Cell Biology. Fall CP, Marland ES, Wagner JM, Tyson JJ. New York: Springer 2002, pp21-52.

[42] Morris C, Lecar H. Voltage oscillations in the barnacle giant muscle fiber. *Biophys J* 1981;**35**(1):193-213.

[43] Rinzel J, Ermentrout B. Analysis of neural excitability and oscillations. In Methods in Neuronal Modeling. Koch C, Segev I. Cambridge: MIT Press 1989, pp135--170.

[44] Strogatz SH. Nonlinear Dynamics and Chaos. Cambridge: Perseus Publishing; 1994.

[45] Wiggins S. Introduction to Applied Nonlinear Dynamical Systems and Chaos. New York: Springer-Verlag; 1990.

[46] Izhikevich EM. Dynamical Systems in Neuroscience. Cambridge: MIT Press; 2007.

[47] Brown E, Moehlis J, Holmes P. On the phase reduction and response dynamics of neural oscillator populations. *Neural Comput* 2004;**16**(4):673-715.

[48] Guckenheimer J. Isochrons and phaseless sets. *J Math Biol* 1975;**1**:259-73.

[49] Yoshimura K, Arai K. Phase reduction of stochastic limit cycle oscillators. *Phys Rev Lett* 2008;**101**(15):154101.

[50] Hoppensteadt FC, Izhikevich EM. Weakly Connected Neural Networks. New York: Springer; 1997.

[51] Neu JC. Coupled chemical oscillators. *SIAM J Appl Math* 1979;**37**:307-15.

[52] Ermentrout GB, Kopell N. Multiple pulse interactions and averaging in systems of coupled neural oscillators. *J Math Biol* 1991;**29**:195-217.

[53] Williams TL, Bowtell G. The calculation of frequency-shift functions for chains of coupled oscillators, with application to a network model of the lamprey locomotor pattern generator. *J Comput Neurosci* 1997;**4**(1):47-55.

[54] Rosenblum MG, Pikovsky AS, Kurths J. Phase synchronization of chaotic oscillators. *Phys Rev Lett* 1996;**76**(11):1804-7.

[55] Maistrenko Y, Popovych O, Burylko O, Tass PA. Mechanism of desynchronization in the finite-dimensional kuramoto model. *Phys Rev Lett* 2004;**93**:084102.

[56] Rall W. Distinguishing theoretical synaptic potentials computed for different soma-dendritic distributions of synaptic input. *J Neurophysiol* 1967;**30**(5):1138-68.

[57] Logan JD. Applied Mathematics. New York: John Wiley & Sons; 1997.

[58] Lefebvre M. Applied Stochastic Processes. New York: Springer; 2006.

[59] Gardiner CW. Handbook of Stochastic Methods. New York: Springer-Verlag; 1985.

[60] Arnold L. Stochastic Differential Equations: Theory and Applications. New York: John Wiley & Sons; 1974.

[61] Hoel PG, Port SC, Stone CJ. Introduction to Stochastic Processes. Boston: Houghton Mifflin Company; 1972.

[62] Glass L, Mackey MC. From Clocks to Chaos: the Rhythms of Life. Princeton NJ: Princeton Univ. Press; 1988.

[63] Glass L. Synchronization and rhythmic processes in physiology. *Nature* 2001;**410**:277-84.

[64] Schimansky-Geier L, Zulicke C. Harmonic noise: effect on bistable systems. *Z Phys B* 1990;**79**:451-60.

[65] Braun HA, Wissing H, Schafer K, Hirsch MC. Oscillation and noise determine signal transduction in shark multimodal sensory cells. *Nature* 1994;**367**:270-3.

[66] Schafer K, Braun HA, Peters RC, Bretschneider F. Periodic firing pattern in afferent discharges from electroreceptor organs of catfish. *Pflugers Arch* 1995;**429**:378-85.

[67] Neiman A, Pei X, Russell DF, Wojtenek W, Wilkens LA, Moss F et al. Synchronization of the electrosensitive noisy cells in the paddlefish. *Phys Rev Lett* 1999;**82**:660-3.

[68] Neiman A, Russell DF. Stochastic biperiodic oscillations in the electroreceptors of paddlefish. *Phys Rev Lett* 2001;**86**:3443-6.

[69] Neiman A, Russell DF. Synchronization of noise-induced bursts in noncoupled sensory neurons. *Phys Rev Lett* 2002;**88**:138103.

[70] Neiman AB, Russell DF. Two distinct types of noisy oscillators in electroreceptors of paddlefish. *J Neurophysiol* 2004;**92**:492-509.

[71] Heinz M, Schafer K, Braun HA. Analysis of facial cold receptor activity in the rat. *Brain Res* 1990;**521**:289-95.

[72] Martin P, Bozovic D, Choe Y, Hudspeth AJ. Spontaneous oscillation by hair bundles of the bullfrog's sacculus. *J Neurosci* 2003;**23**:4533-48.

[73] Camalet S, Duke T, Julicher F, Prost J. Auditory sensitivity provided by self-tuned critical oscillations of hair cells. *Proc Natl Acad Sci U S A* 2000;**97**:3183-8.

[74] Bezrukov SM, Vodyanoy I. Noise-induced enhancement of signal transduction across voltage-dependent ion channels. *Nature* 1995;**378**:362-4.

[75] Batschelet E. Circular Statistics in Biology. New York: Academic Press; 1981.

[76] Mardia K. Statistics of Directional Data. London: Academic Press; 1972.

[77] Hill NA, Hader D-P. A biased random walk model for the trajectories of swimming micro-organisms. *J Theor Biol* 1997;**186**:503-26.

[78] Parra J, Kalitzin SN, Iriarte J, Blanes W, Velis DN, Lopes da Silva FH. Gamma-band phase clustering and photosensitivity: is there an underlying mechanism common to photosensitive epilepsy and visual perception? *Brain* 2003;**126**:1164-72.

[79] Tass PA. Transmission of stimulus-locked responses in two oscillators with bistable coupling. *Biol Cybern* 2004;**91**:203-11.

[80] Bentad JS, Piersol AG. Random Data. New York: Wiley; 2000.

[81] Percival DB, Walden AT. Spectral Analysis for Physical Applications. New York: Cambridge U. P.; 1993.

[82] Mitra PP, Bokil H. Observed Brain Dynamics. New York: Oxford U. P.; 2008.

[83] Arfken GB, Weber HJ. Mathematical Methods for Physicists. San Diego: Academic Press; 1995.

[84] Bahar S. Effect of light on stochastic phase synchronization in the crayfish caudal photoreceptor. *Biol Cybern* 2003;**89**(3):200-13.

[85] Pei X, Wilkens LA, Moss F. Light enhances hydrodynamic signaling in the multimodal caudal photoreceptor interneurons of the crayfish. *J Neurophysiol* 1996;**76**(5):3002-11.

[86] Stratonovich RL. Topics in the Theory of Random Noise. New York: Gordon and Breach; 1967:2.

[87] Netoff TI, Clewley R, Arno S, Keck T, White JA. Epilepsy in small-world networks. *J Neurosci* 2004;**24**(37):8075-83.

[88] Netoff TI, Schiff SJ. Decreased neuronal synchronization during experimental seizures. *J Neurosci* 2002;**22**(16):7297-307.

[89] Lai YC, Frei MG, Osorio I, Huang L. Characterization of synchrony with applications to epileptic brain signals. *Phys Rev Lett* 2007;**98**(10):108102.

[90] Le Van Quyen M, Navarro V, Martinerie J, Baulac M, Varela FJ. Toward a neurodynamical understanding of ictogenesis. *Epilepsia* 2003;**44 Suppl 12**:30-43.

[91] Markram H. A network of tufted layer 5 pyramidal neurons. *Cereb Cortex* 1997;**7**(6):523-33.

[92] Mormann F, Kreuz T, Andrzejak RG, David P, Lehnertz K, Elger CE. Epileptic seizures are preceded by a decrease in synchronization. *Epilepsy Res* 2003;**53**(3):173-85.

[93] Yang XF, Duffy DW, Morley RE, Rothman SM. Neocortical seizure termination by focal cooling: temperature dependence and automated seizure detection. *Epilepsia* 2002;**43**(3):240-5.

[94] Ratzlaff EH, Grinvald A. A tandem-lens epifluorescence macroscope: hundred-fold brightness advantage for wide-field imaging. *J Neurosci Methods* 1991;**36**(2-3):127-37.

[95] Jin W, Zhang RJ, Wu JY. Voltage-sensitive dye imaging of population neuronal activity in cortical tissue. *J Neurosci Methods* 2002;**115**(1):13-27.

[96] Lippert MT, Takagaki K, Xu W, Huang X, Wu JY. Methods for voltage-sensitive dye imaging of rat cortical activity with high signal-to-noise ratio. *J Neurophysiol* 2007;**98**(1):502-12.

[97] Ma HT, Wu CH, Wu JY. Initiation of spontaneous epileptiform events in the rat neocortex in vivo. *J Neurophysiol* 2004;**91**(2):934-45.

[98] Garcia Dominguez L, Wennberg RA, Gaetz W, Cheyne D, Snead OC 3, Perez Velazquez JL. Enhanced synchrony in epileptiform activity? Local versus distant phase synchronization in generalized seizures. *J Neurosci* 2005;**25**(35):8077-84.

[99] Mennerick S, Chisari M, Shu HJ, Taylor A, Vasek M, Eisenman LN et al. Diverse voltage-sensitive dyes modulate GABAA receptor function. *J Neurosci* 2010;**30**(8):2871-9.

[100] Engel J. The Hans Berger lecture. Functional explorations of the human epileptic brain and their therapeutic implications. *Electroencephalogr Clin Neurophysiol* 1990;**76**(4):296-316.

[101] Lee SA, Spencer DD, Spencer SS. Intracranial EEG seizure-onset patterns in neocortical epilepsy. *Epilepsia* 2000;**41**(3):297-307.

[102] Bahar S, Suh M, Zhao M, Schwartz TH. Intrinsic optical signal imaging of neocortical seizures: the 'epileptic dip'. *Neuroreport* 2006;**17**(5):499-503.

[103] Suffczynski P, Kalitzin S, Lopes Da Silva FH. Dynamics of non-convulsive epileptic phenomena modeled by a bistable neuronal network. *Neuroscience* 2004;**126**(2):467-84.

[104] Wendling F, Bartolomei F, Bellanger JJ, Chauvel P. Epileptic fast activity can be explained by a model of impaired GABAergic dendritic inhibition. *Eur J Neurosci* 2002;**15**(9):1499-508.

[105] Wilson HR. Simplified dynamics of human and mammalian neocortical neurons. *J Theor Biol* 1999;**200**(4):375-88.

[106] Ermentrout GB, Kopell N. Frequency plateaus in a chain of weakly coupled oscillators, I. *SIAM J Math Anal* 1984;**15**:215-37.

[107] Wilson HR. Spikes, Decisions, and Actions : The Dynamical Foundations of Neuroscience. New York: Oxford University Press; 1999.

[108] Van Vreeswijk C, Abbott LF, Ermentrout GB. When inhibition not excitation synchronizes neural firing. *J Comput Neurosci* 1994;**1**(4):313-21.

[109] Gard TC. Introduction to Stochastic Differential Equations. New York: Marcel Dekker; 1988.

[110] Hansel D, Mato G, Meunier C. Clustering and slow switching in globally coupled phase oscillators. *Phys Rev E* 1993;**48**(5):3470-7.

[111] Pereira T, Baptista MS, Kurths J. General framework for phase synchronization through localized sets. *Phys Rev E* 2006;**75**:026216.

[112] Pikovsky A, Rosenblum M, Kurths J. Synchronization: A Universal Concept in Nonlinear Sciences. Cambridge: Cambridge University Press; 2003.

[113] Tass PA. Phase Resetting in Medicine and Biology: Stochastic Modelling and Data Analysis. Telos: Springer-Verlag; 1999.

[114] Holmgren C, Harkany T, Svennenfors B, Zilberter Y. Pyramidal cell communication within local networks in layer 2/3 of rat neocortex. *J Physiol* 2003;**551**(PT 1):139-53.

[115] Song S, Sjöström PJ, Reigl M, Nelson S, Chklovskii DB. Highly nonrandom features of synaptic connectivity in local cortical circuits. *PLoS Biol* 2005;**3**(3):e68.

[116] Fisher RS. Animal models of the epilepsies. *Brain Res Brain Res Rev* 1989;**14**(3):245-78.

[117] Avoli M, Barbarosie M, Lücke A, Nagao T, Lopantsev V, Köhling R. Synchronous GABA-mediated potentials and epileptiform discharges in the rat limbic system in vitro. *J Neurosci* 1996;**16**(12):3912-24.

[118] Fröhlich F, Bazhenov M, Timofeev I, Steriade M, Sejnowski TJ. Slow state transitions of sustained neural oscillations by activity-dependent modulation of intrinsic excitability. *J Neurosci* 2006;**26**(23):6153-62.

[119] Park EH, Durand DM. Role of potassium lateral diffusion in non-synaptic epilepsy: a computational study. *J Theor Biol* 2006;**238**(3):666-82.

[120] Norris JR. Markov Chains. New York: Cambridge University Press; 1997.

[121] Wazwaz AM, Hanson FB. Moments of extinction for a singular perturbation problem in the diffusion process. *SIAM J Appl Math* 1991;**51**(1):233-65.

VITA

Daisuke Takeshita was born in 1975 in Tokyo, Japan. He earned a Bachelor of Liberal Arts from the University of Tokyo in 1999, where he studied biology, chemistry, and physics with emphasis on biology, and conducted research on biophysical aspects of a molecular motor, kinesin. He conducted research on the biomechanics and physiology of the musculo-skeletal system in human movement for his Master's degree in Multidisciplinary Sciences, which he earned from the University of Tokyo in 2001. He switched his field to physics and entered the graduate program at the Department of Physics and Astronomy and Center for Neurodynamics at the University of Missouri-St. Louis in 2002, where he conducted research on the neural system from the perspective of nonlinear dynamics and stochastic processes. He earned a Master's degree in Physics from the University of Missouri-St. Louis in 2003 and received his Ph.D. in Physics in the spring of 2010 from the cooperative Ph.D. program of the Missouri University of Science and Technology and University of Missouri-St. Louis.